Investigating the Spectroscopic properties of Mammeigin from *Mesua ferrea* in micro-heterogenous systems

A Thesis submitted in Partial Fulfilment of the Requirements for the Degree of

Doctor of Philosophy

By

S. Sanjana

Roll No. 156106018

Department of Biosciences and Bioengineering

Indian Institute of Technology Guwahati

Guwahati, Assam – 781039, India

December 2022

INDIAN INSTITUTE OF TECHNOLOGY GUWAHATI, Assam, India

Department of Biosciences and Bioengineering

STATEMENT

I do hereby declare that the matter embodied in this thesis is the result of investigations carried out by me in the Department of Bioscience and Bioengineering, Indian Institute of Technology Guwahati, India, under the guidance of Prof. Latha Rangan and Prof. Rajaram Swaminathan.

In keeping with the general practice of reporting scientific observations, due acknowledgements have been made wherever the work described is based on the findings of other investigators.

S. Sanjana

S. Sanjana

IIT Guwahati

December, 2022

INDIAN INSTITUTE OF TECHNOLOGY GUWAHATI, Assam, India

Department of Biosciences and Bioengineering

CERTIFICATE

It is certified that the work described in this thesis, entitled "**Investigating the spectroscopic properties of Mammeigin from *Mesua ferrea* in micro-heterogenous systems**", done by **S. Sanjana** for the award of the degree of Doctor of Philosophy is an authentic record of the results obtained from the research work carried out under my supervision in the Department of Bioscience and Bioengineering, Indian Institute of Technology Guwahati, India, and this work has not been submitted elsewhere for a degree.

Prof. Latha Rangan
Department of BSBE
IIT Guwahati

12 Dec 22

Prof. Rajaram Swaminathan
Department of BSBE
IIT Guwahati

IIT Guwahati

December, 2022

Dedicated to my Family

ACKNOWLEDGEMENTS

I am immensely delighted to be in this position through all the ups and downs in my Ph.D life at IIT Guwahati. I would like to convey my sincere gratitude to all the people who have helped me through my this period.

First and foremost, I express my deepest respect and gratefulness to my thesis supervisors, Prof. Latha Rangan and Prof. R. Swaminathan, for providing me the opportunity to work under their guidance. Their constant support, motivation, expertise, scientific insights and approaches helped me at all times throughout my Ph.D.

Also, I would like to extend my sincere gratitude to the Doctoral Committee members, Prof. Biman B. Mandal, Dr. Satpati Priyadarshi and Prof. Chandan K. Jana for their fruitful suggestions and timely evaluation which helped improvise my Ph.D research.

I thank IIT Guwahati for the facilities and the Ministry of Human Resource Development (MHRD) for providing me financial support. I also extend my thanks to Department of Biosciences and Bioengineering, Central Instrumental Facilities (CIF), North East Centre for Biological Sciences and Healthcare Engineering (NECBH) for the facilities required for my research. I also acknowledge Central Drug Research Institute (CDRI) and IIT Bombay for Liquid Chromatography-Mass Spectrometry analysis. I would like to thank all the BSBE department staff members for being very co-operative and supportive. A special mention to Dr. Babulal Das from Dept. of Chemistry for his support in SC-XRD analysis.

Next, I wish to express my sincere gratitude to all my lab members and friends who have been like a family to me through all the hardships and happy times of my life. Special mention to Rashmi Singh, Dr. Ishani Chakrabartty, Dr. Ashish Prabhu, Dr. Amrendra Kumar, Dr. Sujit Mahato, Dr. Subbi Reddy, Sadokpam Shreekant, Manish Kumar Gupta and Ankan Sinha, to name a few, for assisting me with specific technical support and valuable scientific insights in my research work.

Last but not the least, I would like to express my deepest gratitude to my beloved family for their endless love and support, especially my father who has been the greatest inspiration in my career. A special mention to my new family members, my husband and in-laws for their constant moral support.

S. Sanjana December, 2022

ABBREVIATIONS

HOMO	Highest Occupied Molecular Orbital
LUMO	Lowest Unoccupied Molecular Orbital
DMSO	Dimethyl Sulfoxide
cmc	Critical Micelle Concentration
MMG	Mammeigin
HEWL	Hen Egg-White Lysozyme
TLC	Thin Layer Chromatography
RP-HPLC	Reverse Phase-High Performance Liquid Chromatography
FT-IR	Fourier Transform-Infrared Spectroscopy
LC-MS	Liquid Chromatography-Mass spectrometry
NMR	Nuclear Magnetic Resonance
COSY	Correlated Spectroscopy
HSQC	Heteronuclear Single Quantum Coherence
DEPT	Distortionless Enhancement by Polarization Transfer
SC-XRD	Single Crystal-X-Ray Diffraction
UV-Vis	Ultraviolet-Visible
OOP	Out of plane
SDS	Sodium Dodecyl Sulphate
CTAB	Cetyltrimethylammonium Bromide
T20	Tween 20
O.D	Optical Density
QS	Quinine Sulphate

ThT	Thioflavin T
pHEWL	Polycationic HEWL aggregates

Abbreviations for ^{1}H NMR spectra

s – Singlet	m – Multiplet
d – Doublet	Hz – Hertz
sept – Septate	

THESIS ABSTRACT

Mesua ferrea L. (Calophyllaceae), is a medicinal plant, abundant in Northeast (NE) India. It is a reservoir for a variety of phytochemicals like phenylcoumarins, biflavonoids, xanthones, triterpenoids and so on. Mammeigin (MMG) is one of the 4-phenylcoumarins reported from *M. ferrea* seeds (Bala and Seshadri, 1971). In the current thesis work, it was extracted from the seed oil, further fractionated, isolated and purified through a series of techniques which resulted in high yield (0.64 % w/w of seeds) and high purity (99 %). The structural elucidation was carried out using various analytical techniques.

UV-Visible absorption spectroscopy of MMG was investigated in various solvent systems. Absorption spectra of MMG revealed three absorption bands – band I (232-234 nm), band II (286 nm) and band III (332-370 nm) in organic solvents and it did not exhibit major spectral shifts arising from different solvent polarities. In ethanol-water binary solvent systems of different compositions, absorption of MMG decreased at water concentrations ≥ 60 % (v/v) in ethanol due to precipitation, owing to insolubility. Since MMG is insoluble in water, its aqueous solubility was enhanced using surfactant micelles. The role of charges on MMG-surfactant interactions was investigated using Sodium Dodecyl Sulphate (SDS), Cetyltrimethylammonium Bromide (CTAB) and Tween 20 (T20). The relative environment of MMG in surfactant micelles was comparable to 40 % (v/v) ethanol in water, suggesting the occurrence of MMG interaction sites in semi-polar region of the micelle. Absorption spectral changes of MMG in different surfactant concentrations of pre-cmc (Critical Micelle Concentration), cmc and post cmc were explored. A dip in the absorbance was observed near the cmc among the ionic surfactants, accompanied by scattering in the vicinity of cmc of SDS. While in case of CTAB, the dip in absorbance was due to relative differences in local environment of MMG at cmc. However, these interactions were stabilized in the presence of 200 mM NaCl, resulting in absence of absorbance dip near cmc and saturation in absorbance with increase in SDS and CTAB concentration. The spectral changes were random, accompanied by precipitation at pre-cmc of T20 with and without the presence of NaCl. Also, MMG was not found to be stable over a time period in T20 micelles.

Apart from surfactants, the interactions of MMG with Hen Egg-White Lysozyme (HEWL) aggregates at pH 2, pH 5 and pH 9 were investigated. The results indicated that MMG interacted with the aggregates in pH 2 condition at the initial stage, but not in the case of pH 5.

However, these interactions were not observed at later aggregation and fibrillation stages, owing to inaccessibility to aggregate interior resulting in instability of the MMG-HEWL complex over time. The MMG-polycationic HEWL aggregates formed from transferring mature aggregates from pH 12.2 to 9 revealed that MMG interacted only when HEWL underwent partial unfolding and exposed the hydrophobic regions. The relative environment of HEWL aggregates were comparable to surfactant micelles, but were found to be more heterogenous than the surfactants. Since MMG is water insoluble, it is essential to develop an efficient drug carrier system for targeted drug delivery. The current work will thus provide insights on the nature of interactions of MMG with surfactants and protein aggregates at different solvent conditions.

Furthermore, application of MMG in different pH conditions was investigated. It was observed that MMG was insoluble at acidic and neutral pH, while it showed solubility at alkaline condition in a pH dependent manner. The compound turned yellow (pH 9.5-12) and also exhibited red-shifted spectra as a result of MMG ionization. Whereas in the presence of surfactants, the solubility increased at all pH conditions. But in the presence of CTAB (5 mM) micelles alone, MMG displayed a bathochromic shift ($\Delta\lambda$ = 22-68 nm) in the absorption spectra and brighter yellow colouration at alkaline pH (pH $\geq$ 7.5), along with improved solubilization and stabilization (pH 2-10.5, 13). On the contrary, MMG at pH 13 displayed a different absorption spectra (277 nm and 336 nm peaks) as compared to the native MMG in other solvents. The spectral change was found to be irreversible suggesting permanent chemical change in the compound. Further characterization of MMG in pH 13 suggested that the likely chemical reaction resulted in the formation of carbinol pseudobase and chalcone forms of MMG. Therefore, due to difference in the absorption properties of MMG at different pH, it can be utilized as a pH indicator.

The effect of specific ions of group 1 and 17 elements as sodium and chloride salts i.e., LiCl, NaCl, KCl, NaF, NaBr, NaI on the spectroscopic properties of MMG in surfactants were investigated. Absorption spectra of MMG displayed a wide range of variations at higher concentration (200 mM) of the salts. In the presence of NaF, MMG displayed a red-shifted spectra in the presence of CTAB, similar to the alkaline condition. This shift in spectra was not observed for other solvents like organic-aqueous systems, suggesting no direct binding of MMG with fluoride. Also, lower CTAB concentration with 10 mM NaCl displayed better sensitivities to NaF than at higher CTAB concentrations. MMG exhibited prominent changes in

the absorption spectra only at high NaF concentrations. Further it was observed that the presence of interfering ions (levels in drinking water) did not induce significant changes in the presence of NaF. To conclude, MMG in CTAB solution can be utilized for applications related to fluoride sensing in concentration range of 2.4-200 mM.

TABLE OF CONTENTS

Chapter 1

Introduction and Review of Literature

1.1. Introduction

Plants are the greatest chemists in nature that have dominated the world by their colors, odor, taste and nutritive values. Chemical compounds known as secondary metabolites, alternatively called phytochemicals are responsible for such medley in plants (Cheynier et al., 2013; Manach et al., 2004). These compounds are not directly involved in primary metabolism like photosynthesis or respiration, but are thought to be essential for the survival of plants in the environment and as a means of communication with other living organisms (Cheynier et al., 2013; Daayf and Lattanzio, 2009). They are more diverse than primary metabolites, both structurally and functionally.

Major categories of phytochemicals are phytosterols, terpenoids, polyphenols, saponins, alkaloids, aromatic and organic acids, carotenoids, essential oils and protease inhibitors (Bansal and Priyadarsini, 2021).

1.2. Plant polyphenols: Classification and therapeutic potential

One of the major classes of secondary metabolites with a variety of functions in plants is polyphenols. Plant phenolics are considered to play a leading role in defense against biotic and abiotic stresses like intense light, temperatures, pathogen infections, herbivores, nutrient deficiency and so on (Lattanzio, 2013). These compounds are biogenetically produced from two pathways. Either as phenylpropanoids through shikimate/phenylpropanoid pathway or as simple phenols through "polyketide" acetate/malonate pathway, resulting in phenols and polyphenols in monomeric and polymeric forms (Lattanzio, 2013; Quideau et al., 2011). The ability to synthesize phenolic compounds in different plant lineages has been selected throughout the course of evolution, to permit plants cope with dynamic environmental challenges (Boudet, 2007; Lattanzio, 2013). Phenolics are not commonly found in bacteria, fungi and algae. Bryophytes regularly produce them, but it is the vascular plants that possess a full range of diverse polyphenols (Harborne 1980; Swain 1975). It has been estimated that about 2% of the carbon originating from photosynthesis is converted to polyphenols like flavonoids or closely related compounds (Robards and Antolovich, 1997).

Structurally, they consist of multiple phenolic rings with functional group substitutions. The phenolics are categorized into several classes based on their basic skeleton: C_6 (simple phenols, benzoquinones), C_6-C_1 (phenolic acids), C_6-C_2 (phenylacetic acid, acetophenone), C_6-C_3 (hydroxycinnamic acids, coumarins, phenylpropanes, chromones), C_6-

C_4 (naphthoquinones), C_6-C_1-C_6 (xanthones), C_6-C_2-C_6 (stilbenes, anthraquinones), C_6-C_3-C_6 (flavonoids, isoflavonoids, neoflavonoids), $(C_6$-C_3-$C_6)_{2,3}$ (bi-, tri- flavonoids), $(C_6$-$C_3)_2$ (lignans, neolignans), $(C_6$-$C_3)_n$ (lignins), $(C_6)_n$ (catechin melanins) and $(C_6$-C_3-$C_6)_n$ (condensed tannins) (Lattanzio, 2013; Quideau et al., 2011). The backbone structure of the major plant phenolic classes are illustrated in **Fig 1.1**.

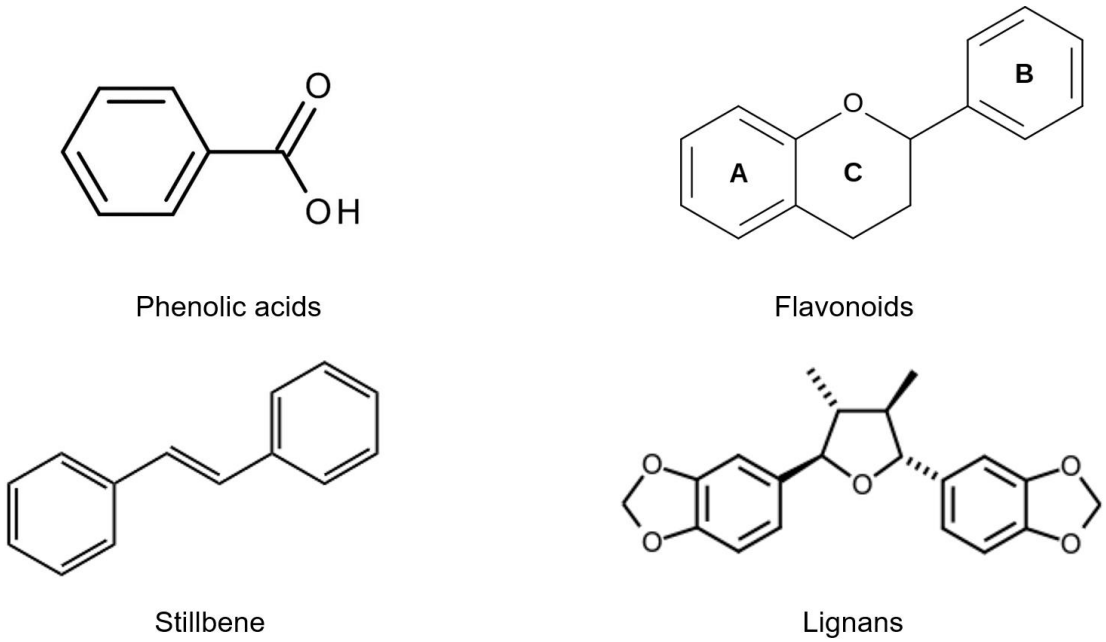

Figure 1.1: Major classes of plant phenolics (A, B and C rings of Flavonoids)

The structure of these compounds owe to the potential for electron delocalization. Therefore, the phenolic groups are readily ionizable and act as weak acids. Apart from this, the other main feature is substitutions on the parent structure that imparts specific chemical reactivity and enables them to form stable complexes with other molecules (Cheynier et al., 2013). For example, the interaction of hydroxyl groups with the π-electrons of the aromatic ring, gives the ability to stabilize the generated free radical through electron delocalization (Cheynier et al., 2013). These key features makes them the best antioxidants in the entire plant kingdom, along with other properties like single oxygen quencher and radical scavenger (Guo et al., 1999). Thus, nature of the substituent and surrounding reactants have a great impact on the functional properties of these compounds.

Inspired by their wide distribution in nature and functional properties, humans have exploited phenolic compounds extensively as bioactive food components on the account of their therapeutic value. One of the epidemiological concepts that has significantly drawn

attention to plant polyphenol research is the "French paradox", an observation of lower incidence of coronary heart diseases among French people in spite of their high fat diet, as an outcome of regular wine drinking habit. Wine and red wine in particular, is extremely rich in polyphenols like flavanols, anthocyanins, hydroxylated stilbenes, proanthocyanin oligomers, pyrogallols derived from grapes and ellagitannins, ellagic acid from oak barrels (German and Walzem, 2000; Quideau et al., 2011). Further recognition of health benefits of green tea, coffee, chocolate, cider, fruits and berries has sparkled a new appraisal for plant-derived polyphenols (Quideau et al., 2011). They are considered as the major non-nutrient constituent that has been proven to possess variety of therapeutic benefits (Adebooye et al., 2018). Their reputation has been uplifted currently due to encouraging clinical studies in a range of disease profiles, that appear to confirm efficacy (Goszcz et al., 2017).

Due to the antioxidant property, they exhibit cardio-protective, neuro-protective, anti-cancer, anti-ageing activities and so on. Apart from antioxidation, other properties like anti-inflammatory, anti-platelet, anti-proliferation, anti-diabetic, immunomodulation, metal chelation, UV protection have been reported. These range of bioactivities has broadened their utilization in cosmetic applications (Pandey and Rizvi, 2009). Asides from this, they are also utilized in the fields of food technology, dyeing industry, pesticides, polymer synthesis and so on.

Recently, the spectroscopic properties of these compounds have gained attention as fluorescent tracers for biological applications (Duval and Duplais, 2017). The structural features of plant phenolic compounds and their surrounding environment, influence the electronic distributions and thus their UV-Visible absorption and luminescence properties.

1.3. UV-Visible spectroscopy of plant polyphenols

Molecules have distribution of charges and spins with electric and magnetic field, which are altered upon interaction with light. These interactions enable the molecules to undergo electronic transitions from lower electronic state (S_0) to higher energy state (S_1, S_2) (Cantor and Schimmel, 1980; Lakowicz, 2013). Such electronic transitions can take place in UV, visible and near-infrared spectral regions. A molecule consists of various molecular orbitals, namely – σ orbital (involving s atomic orbitals or p orbitals with collinear symmetrical axis); π orbital (between two laterally overlapping p atomic orbitals) and n orbital (non-bonding orbital with lone pair of electron). Transitions involving promotion of a π electron to

antibonding orbital π* is called π- π* transition. Molecules possessing heteroatoms like oxygen or nitrogen, undergoes n- π* transitions. While, the transitions involving σ electrons are high energy demanding (Valeur and Berberan-Santos, 2012). (**Fig 1.2**)

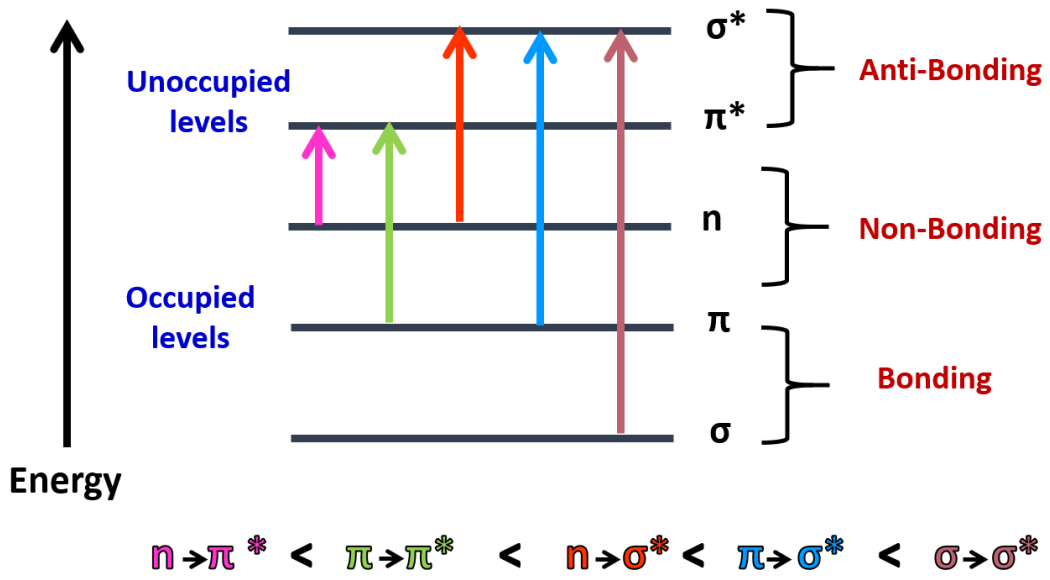

Figure 1.2: Electronic energy levels and transitions (Adapted and redrawn from Pavia and Lampman, 2009)

The molecule absorbs energy that involves the electron being promoted from Highest occupied molecular orbitals (HOMO) to Lowest unoccupied Molecular orbitals (LUMO) to undergo electronic transitions (Pavia and Lampman, 2009; Cantor and Schimmel, 1980). Aromatic compounds typically undergo π-π* transitions assigned to conjugated system and n-π* transitions to the nature of substituents (Pavia and Lampman, 2009). The absorption transition moments of π-π* occurs in the plane of the molecule, whose direction about the molecular axis determines the electronic state upon excitation. The transition moment along short axis corresponds to S_0-S_1 transition. While the transitions along long axis corresponds to S_0-S_2 transitions (Valeur and Berberan-Santos, 2012). The differences in the absorption spectrum are influenced by ionization potential (IP), electron affinity (EA), hardness (η) and electrophilicity (ω) of the compound (Anouar et al., 2014).

Unlike monocyclic compounds, polyphenols have extended conjugation due to which the electronic energy levels move closer. This reduces the energy required to produce transition, thus causing bathochromic shifts along with hyperchromism (Pavia and Lampman, 2009). Flavonoids are the most abundant and well-studied class of polyphenols. They have

two aromatic rings – A and B linked through a heterocyclic pyran ring C (**Fig 1.1**). In general, they display two major bands – 240-295 nm (band II) corresponding to the A- ring and 300-400 nm (band I) to the B-ring (Farajtabar and Gharib, 2013; Kumar and Pandey, 2013).

For most of the flavonoids, the LUMO clusters are located on carbonyl group or delocalized over molecular moiety containing the carbonyl group whereas the HOMO clusters are delocalized on the B ring. Therefore, the HOMO-LUMO transition involves intramolecular charge transfer (Marković and Tošović, 2015). Other flavonoid classes like neoflavonoids and isoflavonoids have weak conjugation between B and C rings and a twisted structure due to rotation of phenyl ring with respect to chromone part. This demands larger excitation energies for transition which results in shorter peaks (Cornard et al., 1997; Marković and Tošović, 2015; Tošović and Marković, 2017). On the other hand, flavones, flavonols and anthraquinones have shorter HOMO and LUMO gap due to which the spectra appears at a longer wavelength and produce intense absorption bands due to transitions from these clusters (Marković and Tošović, 2015; Tošović and Marković, 2017). **Figure 1.3** depicts an example of HOMO and LUMO clusters of flavonoid Luteolin.

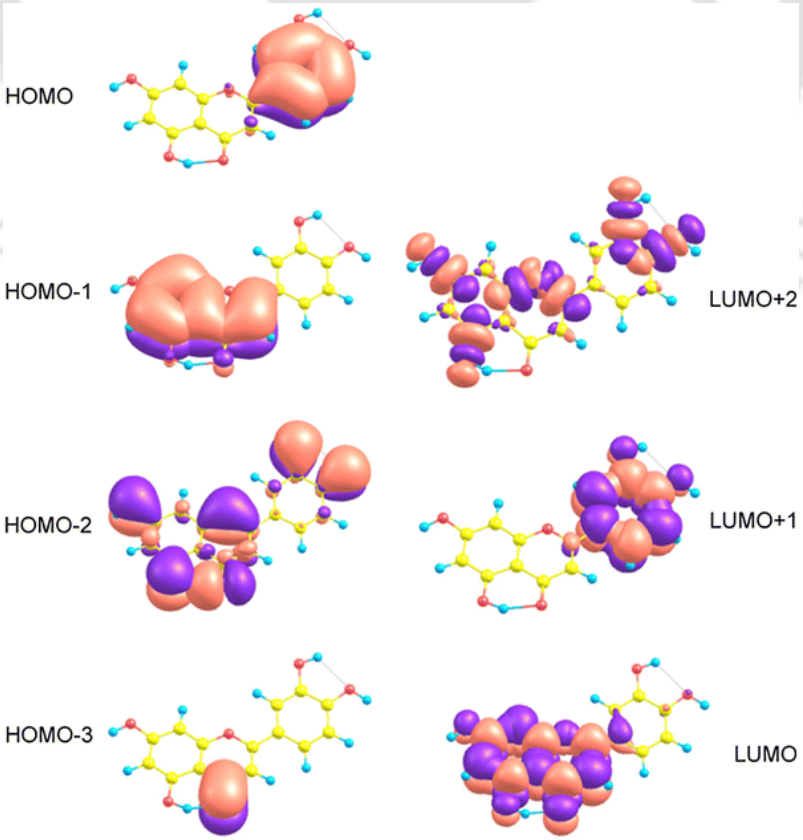

Figure 1.3: Selected bonding (HOMO-3 – HOMO) and antibonding (LUMO-LUMO+2) Natural Localized molecular orbital clusters of Luteolin (Adapted from Tošović and Marković, 2017). The pink and violet regions refer to the molecular orbitals with alpha and beta electron densities.

Aside from the substitutions, the geometry of molecule too greatly influences the spectral properties. Quercetin is speculated to exist in different conformers that differ in torsional angle between (A+C) and B ring and attains dynamic stability in non-polar environment. For these conformers, only the initial H-bonds and van der Waals interaction exists between C and B ring without any specific interactions (Brovarets' and Hovorun, 2020). Myricetin exhibited absorption at 390 nm, but in the twisted state ($\theta = 90^{o}$) the transitions are blue shifted (338 nm) and intensity of absorption is reduced. It attains planarity after excitation resulting in delocalization of HOMO and LUMO over the entire molecule (Vojta et al., 2017). Also the positions of hydroxyl group decide the torsional orientation of the phenyl ring with respect to the benzopyran moiety. Flavonoids with hydroxyl groups at C5 and C3 are stabilized by intramolecular hydrogen bonding and thus attain energetically preferred conformations (Michalík et al., 2020). The absence of C2-C3 double bond disrupts the conjugation between the rings which separates HOMO and LUMO on B and A rings respectively, causing hypsochromic shifts (Farajtabar and Gharib, 2013; Rajendran et al., 2013).

1.4. Sensitivity of polyphenols to surrounding

Solvent is a discontinuum characterized by molecular properties like dipole moment, electronic polarizability, hydrogen bond donor and hydrogen bond accepting properties and so on (Reichardt, 2007). Solvatochromism is described as the prominent change in the position and intensity of UV-Visible absorption band of the solute molecule due to change in the polarity of the medium (Nigam and Rutan, 2001). The solvent effects mainly originate from specific and non-specific interactions between solute and solvent. The non-specific interactions occurs in neutral or ionic solute molecules, with stable electronic polarizability, permanent dipole moment or charge. They interact with solvent through dipole-dipole, dipole-induced dipole and induced dipole-induced dipole interactions (Reichardt, 2007).

The specific solute/solvent interactions involve chemical interactions such as hydrogen bonding, complexations, acid-base chemistry and charge transfers. One of the commonly observed specific interactions is hydrogen- bonding between solute and solvent molecules. For instance, Rosmarinic acid exhibits bathochromic shift with increase in solvent

polarity due to hydrogen bonding with polar protic solvents (Danaf et al., 2016). Curcumin shows broad structureless absorption with larger shifts in polar solvents, whereas it displayed structured spectrum in non-polar solvents, especially in cyclohexane. Also, bathochromic shift was observed with increase in solvent polarity (**Fig 1.4**) (Nardo et al., 2008). The spectral changes were also ascribed to different conformations of curcumin due to hydrogen bonding differences in different solvent environments (Adhikary et al., 2009; Balasubramanian, 1991; Khopde et al., 2000; Nardo et al., 2008; Priyadarsini, 2009). Certain anthocyanins like peargonidin-3-O-glucoside on the other hand, undergoes solvatochromism inversely proportional to the solvent polarity (Iosub et al., 2014; Reichardt and Welton, 2011; Sinopoli et al., 2019).

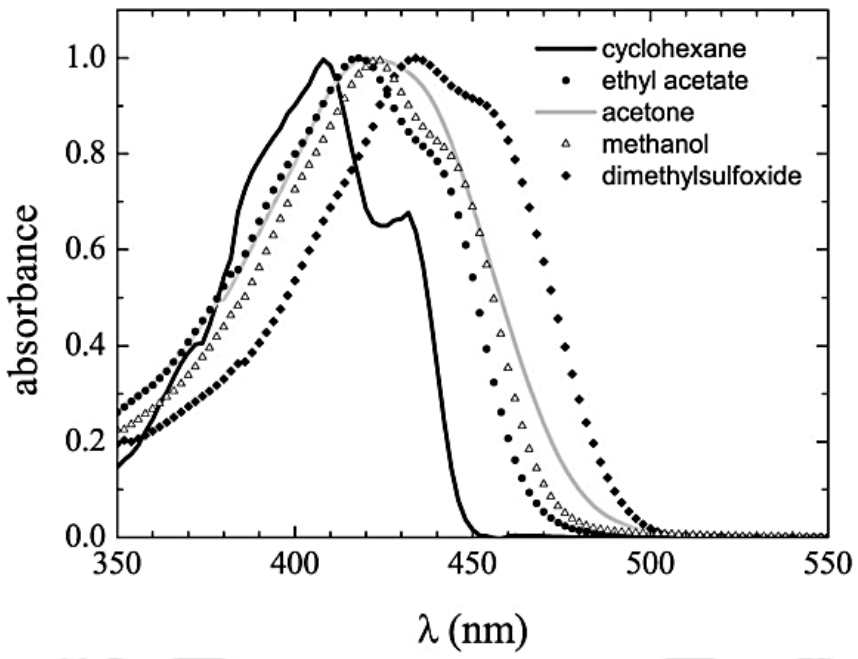

Figure 1.4: Absorption spectra of curcumin in: cyclohexane (solid black line), ethyl acetate (dots), acetone (solid grey line), methanol (triangles), dimethyl-sulfoxide (diamonds). The peak absorbances were normalized to 1. (Adapted from Nardo et al., 2008)

It should be noted that these interactions are different from the actual proton transfer reactions (Nigam and Rutan, 2001). Furthermore, solvents are categorized as highly structured solvents (such as water with strong HB capabilities and formation of cavities with intermolecular networks) and less structured solvents (such as hydrocarbons filling space in regular manner with weak dispersion forces) (Cheremisinoff, 2003; Fawcett, 2004; Marcus, 2002, 1998; Reichardt, 2007; Wypych, 2001).

Another commonly studied specific solute/solvent interactions is acid-base chemistry. With increase in pH of the solution, the absorption band of flavonoids can switch from UV-B (280-290 nm) to UV-A (≈325 nm) or from UV-A to visible region (Biler et al., 2017). Rosmarinic acid displayed notable red-shift in both absorption and fluorescence spectra corresponding to various protonated and deprotonated forms (**Fig 1.5 a and b**) (Danaf et al., 2016).

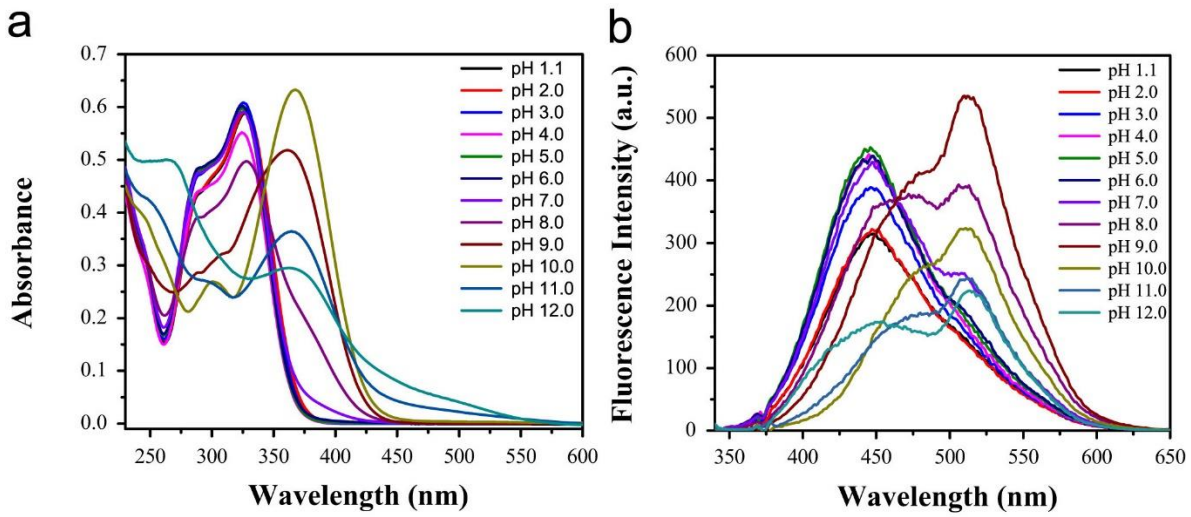

Figure 1.5: (a) UV–Vis absorption spectra of Rosmarinic acid at different pHs. (b) Fluorescence emission spectra (scattering corrected) of RA at different pHs, the excitation wavelength was 330 nm (Adapted and rearranged from Danaf et al., 2016)

Plant silymarin flavonolignans like silybin, silychristin, silydianin under acidic conditions exhibit two absorption bands – band I in UV-B region (280-290 nm) corresponding to S_0-S_3 transition and shoulder band II in UV-A region (335 nm) to S_0-S_1 transition. Upon deprotonation in alkaline conditions, the UV-A peak dominates over the other (Biler et al., 2016). Apigenin, fisetin and luteolin have undetectable fluorescence in acidic pH but with increase in pH, fluorescence is enhanced (Favaro et al., 2007; (Funes et al., 2007). Anthocyanins at acidic pH displays pink-red hues while at alkaline pH, it displays blue hues where the absorption maxima shifts from 510 nm to 607 nm (Sigurdson et al., 2018).

Solvent mixtures on the other hand, can have improved physical properties like solvation power, viscosity, density, refractive index, relative permittivity, freezing and boiling points (Reichardt, 2007). Solvent-solvent interactions have a great influence in the solvation behaviour of molecules, affecting their spectral behaviour. Quercetin in binary solvent mixtures deviated from linear solvatochromism as an effect of solvent-solvent

interactions and preferential solvation (Faraji and Farajtabar, 2020). Even amongst different binary solvent mixtures, there can be differences. Morin exhibits dual fluorescence in acetonitrile and water mixtures (385 nm and 500-560 nm) but not in aqueous methanol mixtures (495 nm) which is ascribed to the stabilizing effect on intramolecular hydrogen bonding (Park et al., 2015). Curcumin displayed increase in absorption peak at 429 nm with decrease in 357 nm peak with increasing ethanol concentration in water due to different proportions of diketo-enolic forms (**Fig 1.6**) (Bhatia et al., 2016)

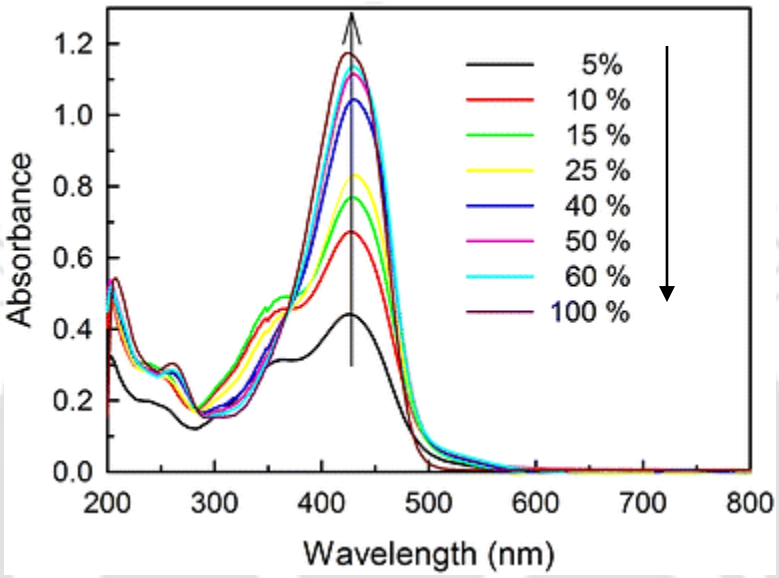

Figure 1.6: Absorption spectra of curcumin (25 mM) in solutions of different volume percentages of ethanol at pH 7.0 (Adapted from Bhatia et al., 2016)

Curcumin in binary mixtures of toluene and methanol showed decrease in the fluorescence decay (170 to 30 ps) with increase in methanol concentrations, when taken at red edge of the emission spectrum (Saini and Das, 2012). In 1:1 ethanol-water mixtures, Karanjin (furanoflavonoid) exhibited two absorption bands- band I at 307 nm (n-π*) and intense band II at 262 nm (π- π*) (Aslanoğlu and Öge, 2005; Janjua et al., 2009; Yang et al., 2004). Conversely, karanjachromene (pyranoflavonoid) has only one peak at 270 nm corresponding to π- π* transition (Arshad et al., 2013). In binary mixtures of methanol and water, Karanjin displayed decrease in the absorbance at 261 nm and 309 nm with increasing water concentration (Singh et al., 2021).

1.5. Plant polyphenols: drug-delivery challenges and strategies

Plant polyphenols, in spite of showing promising results in *in vitro* studies, were not replicable in *in vivo* studies in many cases, which attributed to low bioavailability of these compounds. This is as the result of low solubility and stability under gastrointestinal conditions like acidic pH, enzymes and influence of other nutrients, lower diffusion through lipid-bilayer cell membranes and dose: solubility ratio (Chen et al., 2012; Kaur and Kaur, 2014; Li et al., 2015). The lower absorption corresponds to their polarity and substitution groups, according to "Lipinski rule" (Biasutto et al., 2014; Lipinski et al., 2001). On the other hand, it is important to consider cell permeability properties of the compound along with its aqueous solubility. Based on this property, polyphenols are classified as (1) high solubility but poor cell membrane permeability; (2) low solubility and poor cell membrane permeability; and (3) low solubility but high cell membrane permeability (Hu et al., 2017).

There are various strategies employed for balancing the aqueous/lipid solubility, increasing bioavailability and efficacy (**Table 1.1**).

Table 1.1: Various strategies for enhancing bioavailability of polyphenolic compounds (Kaur and Kaur, 2014, with modifications)

Method	**Working**	**References**
Prodrug	Using precursor molecule to disguise polyphenols as a 'reversible cap' during absorption and released by suitable kinetics to revive the parent compound at the target site.	Biasutto et al., 2014
Food-grade macromolecules	Biopolymers like protein, carbohydrates, fats and their conjugates based nanoparticles, nanocomplexes, nanoemulsions, nanoencapsulates.	Hu et al., 2017; Huang et al., 2010
Self-microemulsification	Oil in water microemulsions using surfactants and co-surfactants.	Balakrishnan et al., 2009; Neslihan Gursoy and Benita, 2004
Solid dispersion	Preparation of eutectic mixtures of drug and hydrophilic carriers through phase change	Kumar et al., 2022; Serajuddin, 1999

Antisolvent method	Precipitation of drug using antisolvent, then stabilizing and processing using high pressure homogenization, syringe pump, evaporative precipitation and supercritical methods	Kaur and Kaur, 2014
Nanoparticles	Metal nanoparticles, nanoformulation, nanofilms,	Chandrakala et al., 2022; Chen et al., 2011; Shetab Boushehri et al., 2020

Surfactants and protein based carrier systems are discussed in detail.

1.5.1. Surfactants

The term surfactant is derived from "Surface Active Agents", which has the tendency to absorb at interfaces. They possess both hydrophobic and hydrophilic characteristics (Dave and Joshi, 2017; Holmberg, 2007). The hydrophilic part has stronger affinity to polar solvent while the hydrophobic part has attraction for the oil/hydrophobic core. The polar head group constitutes the hydrophilic portion and the hydrophobic part constitutes of a long chain hydrocarbons (**Fig 1.7**).

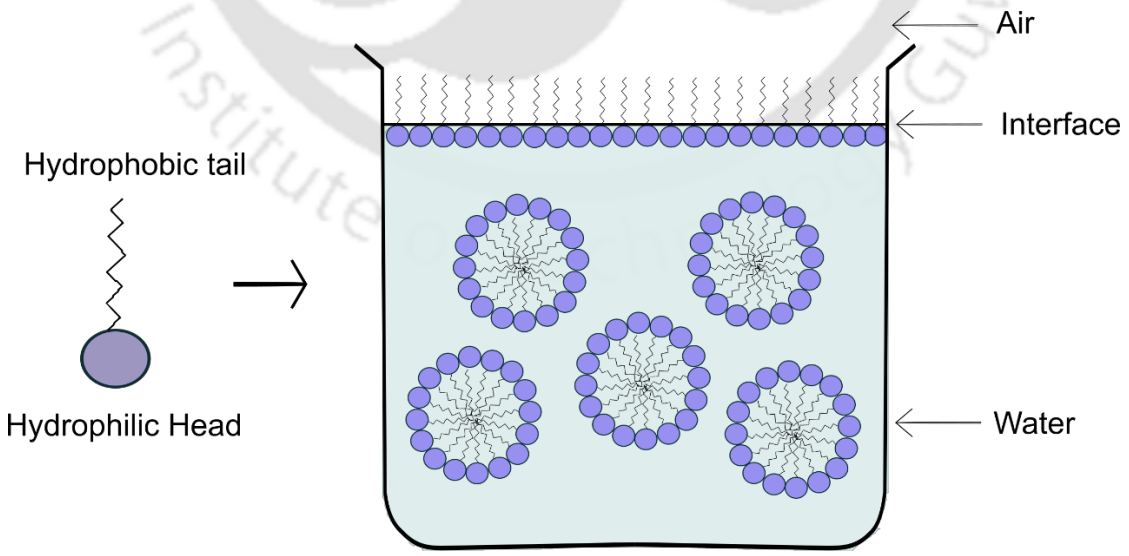

Figure 1.7: Schematic representation of surfactant molecule and its micelle formation in water.

The fundamental characteristic of the surfactant is its tendency to self-aggregate in solution to form molecular assemblies called micelles. Here, the polar heads form the outer shell in contact with the water and hydrophobic tails are cocooned in the interior. There exists monolayer of surfactant molecules at the air/water interface, with the head groups interacting with the water and hydrophobic tails in the air (**Fig 1.7**). The formation of micelles only occurs beyond a surfactant concentration called Critical Micelle Concentration (cmc). The size and shape of the micelle varies from spherical-to-rod- or disc-like to lamellar, depending on the chemical nature of head and tail group and the bulk solution properties. Ionic surfactants form smaller micelles than non-ionic surfactants, due to electrostatic repulsions between head groups, which is greater than the steric repulsion between non-ionic head groups (Dave and Joshi, 2017).

The surfactants are classified into seven major categories (Dave and Joshi, 2017; Janakiraman et al., 2019; Yuan et al., 2014)–

(1) *Anionic surfactants*: They are negatively charged when dissociated in water. It has employed as foaming agents, antistatic agents, stabilizers, dispersants and detergents. Types of hydrophilic groups constituting anionic surfactants are sulphates, sulphonates, carboxylic acid salts, phosphate ester, fatty acid salts.

(2) *Cationic surfactants*: They have positive head groups. They are reported to be good emulsifying agents. Based on the chain arrangement, they are further classified into heterocyclic group type, open-chain surfactants, bonded intermediate connection type surfactants. They find applications in topical antiseptics and germicides in hand washes/sanitizers. Apart from this, it is also used for mineral flotation applications.

(3) *Non-ionic surfactants*: They ionize in water, but do not possess electric charge and less hardness sensitive. The hydrophilic groups in this surfactant category are further classified as polyethylene glycol, glycosidic, polyhydric alcohols and polyether types. They are highly potent in grease removal due to which they find applications in laundry products, dishwashers and liquid handwashes. They are also frequently used in pharmaceutical industry for drug-delivery applications.

(4) *Zwitterionic surfactants*: They are amphoteric with both anionic and cationic groups. They are classified into betaine, lecithin, imidazoline and amino acid-type, based on the anionic type in the molecule. They are very mild surfactants making them popular in personal

care and household cleaning products. They have great dermatological properties due to which it is used in shampoos and other cosmetics products.

(5) *Specialty surfactants*: They possess distinct features like high thermal and chemical stability, heightened surface activities. Elements like Thallium, Germanium, Titanium are added to enhance the surfactant molecules. They are employed in mineral processing, fire protection, pesticides, leather and chemical industries.

(6) *Macromolecular surfactants*: They constitute the polymeric surfactants with molecular mass over 10000 Da. Based on the source, they are segregated into natural, modified natural materials and composing materials. They are applied as gelling agents, thickener, emulsifying agent, antistatic and dispersing agent.

(7) *Bio-surfactants*: They are involved in dissolving out surface-active metabolites in their metabolism. Depending on the chemical structure, they are classified into proteins, phospholipids, sugar and polysaccharide esters. They are extensively used as emulsifiers, anti-static, foaming and wetting agents. They are utilized applications like cosmetic, textile, pharmaceutical, food industries and so on.

The surfactant works through three mechanisms- Roll-up, emulsification and solubilization. Roll-up mechanism involves reduction of the interfacial surface tension of oil/solution and surface/solution and thereby removing the oil. Emulsification involves preparation of simple oil emulsion by sinking oil/solution interfacial tension. Solubilization works by interfacing of solute molecules with surfactants in solvent resulting in liquification of the solute to make a pure and uniform solution (Janakiraman et al., 2019). The surfactant characteristics are highly influenced by the presence of salt in the solution which can influence the micelle shape, size, cmc and interfacial behaviour (Hooshyar and Sadeghi, 2015). However, the reports of the effect of different salts on plant polyphenols in surfactants are very limited.

For enhancing the aqueous solubility of flavonoids and drug-like compounds, pharmaceutically tolerant surfactants and co-surfactants are used. Surfactant-based drug delivery carriers have been used for improving bio-efficacy and bioactivities. Non-toxic and non-ionic surfactants like alkyl esters, alkylamides, and fatty acid esters, along with cholesterols were used for preparing nano-formulations like Niosomes. Some examples with enhanced biological activity in niosomes are quercetin for skin water-locking effect,

polyphenol-rich propolis for antibacterial activity, curcumin with paclitaxel for improved chemotherapeutic efficacy and so on (Yang et al., 2020). Another popular technique is Microemulsion containing surfactant and also co-surfactant in most cases. Surfactants like Aerosol OT and Tween 80 were used for enhancing the intradermal delivery of curcumin and resveratrol (Yutani et al., 2012). Licorice flavonoids loaded in microemulsions made of laureth-9, propylene glycol and isopropyl myristate exhibited higher transdermal penetration and retention of the flavonoids (Xin et al., 2021). Microemulsion of Chrysin has displayed improved bioactivities like anti-inflammatory and anti-hyperalgesic (Ramalho et al., 2022). While its Nanoemulsion have shown stability of Chrysin without affecting its antioxidant and cholinesterase inhibition (Ting et al., 2021).

Surfactants play an important role in pharmaceutical industries, where they are used in drug delivery systems. Amongst the current drug delivery approaches, the use of polymeric surfactant micelles are still considered as smart substitute. **Fig 1.8** summarizes the pharmaceutical applications of surfactants (Suhail et al., 2019).

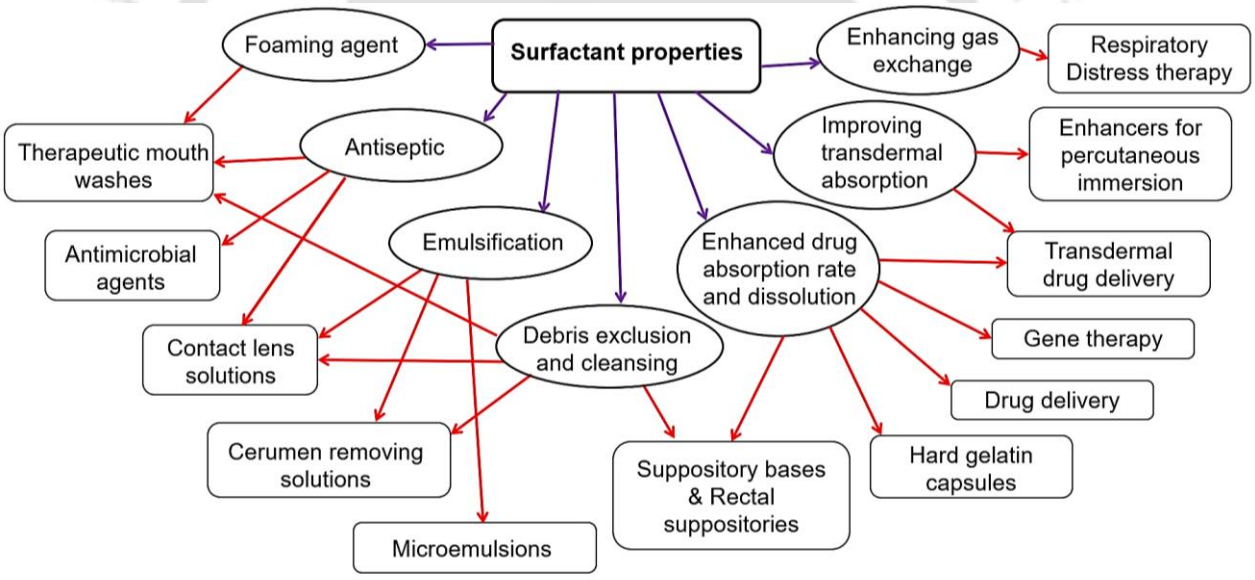

Figure 1.8: Surfactant properties and its pharmaceutical applications

1.5.2. Food-based protein carriers

Proteins adopt folded conformation depending on the amino acid sequence. It folds such that the hydrophobic side chains of amino acids form the hydrophobic core while the polar and charged amino acid side chains interact with water. The final three-dimensional structure of the protein is a delicate balance of these interactions (Kralova and Sjöblom, 2009). Proteins

are classified as Bio-surfactants. They can aggregate with each other or with other macromolecules via various chemical interactions, majorly involving hydrogen, hydrophilic and ionic bonding. They are governed by external conditions like ionic strength, pH, salt concentration and type, mechanical force, temperature and so on. Thus by altering such conditions, the aggregation of proteins can be either triggered or reversed (Chiti and Dobson, 2006; Tomadoni et al., 2020). The aggregation propensity depends hugely on the nature and charge of the amino acids. The aggregates expose the hydrophobic regions which tend to further mature and form fibrils. Protein fibrils are characterized by canonical cross-β structure and the presence of repetitive hydrophobic or polar interactions along the axis of the fibrils (Chiti and Dobson, 2006).

Such aggregating macromolecules can serve as potent molecule carriers. Amongst the proteins, the ones from the food source have gained attention due to their edibility, biocompatibility and biodegradability (Sahu et al., 2008). Many proteins from different sources like whey proteins, milk proteins, egg white proteins, gelatin, soy proteins are well known as emulsifiers in production of various dairy products and baked goods (Kralova and Sjöblom, 2009). Their aggregates and assemblies have exhibited promising results as drug-carriers (Chang et al., 2022; Daniloski et al., 2021; Li et al., 2019; Tomadoni et al., 2020). They enhance gastrointestinal absorptivity of the drugs and nutrients and also provide protection from chemical degradation by external factors like temperature, oxidation, formulation and food processing (Chang et al., 2022). **Table 1.2** summarizes various food-based drug carriers, their preparation, characteristics and examples where they were utilized as carrier for plant polyphenols.

Table 1.2: Food-based drug carriers, preparation, characteristics and applications as carrier for plant polyphenols.

Source	Proteins	Preparation and Characteristics	Application	References
Milk	Caseins	Self-assembly; pH <4.5 with slow heating. Formation of spherical micelles (50-500 nm); gel matrix	Catechin, gallic acid, quercetin, caffeic acid, vanillin for anti-cancer activities. Encapsulation of curcumin for anticancer and anti-hemolysis	Hu et al., 2017; Mehanna et al., 2014; Tomadoni et al., 2020; Tosif et al., 2021

Whey	β-lactoglobulin α-lactalbumin, bovine serum albumin: immunoglobulin and lactoferrin.	Prolonged heating at low pH 2 and ionic strength. Forms Globular and spherical ; fibril	EGCG, curcumin, resveratrol In anticancer, photostability, hydrosolubility	Chang et al., 2022; Gao et al., 2017; Hu et al., 2017; Tomadoni et al., 2020
Egg protein	Globulins, Lysozyme, Ovalbumin, Ovatransferrin	Self-assembly; low pH, heating and mechanical force. Forms granular/fibrous assemblies	Renal drug targeting; EGCG for treating ulcerative colitis; enhanced antioxidant activity of quercetin and kaempferol	Chang et al., 2022; Gou et al., 2018; Kok et al., 1998; Zhou et al., 2022
Food promalin	wheat (gliadin), barley (hordein), rye (secalin), corn (zein), sorghum (kafirin), and as a minor protein, avenin, in oats	Antisolvent precipitation, ultrasonic homogenization with sodium stearate. Formation of spherical micelles	Curcumin, resveratrol, gallic acid with enhanced antioxidant activity	Chang et al., 2022; Hu et al., 2017; Xu et al., 2022; Zhou et al., 2018
Soy proteins	Soy albumins, soy globulins	Salting out, heating at 90/100 ºC results in self-assembling	Nanocomplexation with curcumin, resveratrol, folic acid, vitamin-B_{12}, β-carotene	Chang et al., 2022; Tang, 2019
Gelatin	-	Hydrolysis of collagen; glutaraldehyde cross-linking	Nanostructures to encapsulate food ingredients	Ali et al., 2019; Chang et al., 2022; Tomadoni et al., 2020

1.6. *Mesua ferrea* and its significance

Mesua ferrea L. is a flowering plant belonging to the family Calophyllaceae of Malpighiales order (Sharma et al., 2017). *Mesua* is a large genus comprising of 48 species, and *M. ferrea* is the most studied plant (Chahar, 2013). It is commonly known as 'Nagakesar' or Ceylon Ironwood. It is a medium to large (20-30 m height) evergreen tree with dark red heartwood. The young leaves are red which turn dark green upon maturation and have a waxy bloom below (Chahar, 2013; Sharma et al., 2017). It is found in many Asian countries like India, Indo-China region, Malaysia, Myanmar, Nepal, Sri Lanka, Thailand, Sumatra, Phillipines,

Burma and Cambodia (Asif et al., 2017). In India, it is distributed in Himalayan region, Northeast India, deccan peninsula and Andaman islands (Sahu et al., 2014). It grows in moist fertile soil with neutral pH, but also reported to grow in stress conditions due to tolerance to heavy metals (Mitra et al., 2021; Sahu et al., 2014).

It has found immense uses amongst locals in various countries. In Malaysia and Thailand, its seeds are used for treating wounds, while the leaves and roots decoction is used by the women after child birth in Malaysia (Arora et al., 2019; Asif et al., 2017). In India, the fruits are used as antiseptic, antihelminthic, expectorant, antipyretic, purgative agent. The oil is used for treating skin infections, rheumatism and scabies. The leaves and flowers are used to treat snake and scorpion bites (Sharma et al., 2017). The ashes of the leaves are used to treat sore eyes and the flower paste along with butter and sugar are used for treating piles and burns (Arora et al., 2019).

Due to its ethnopharmacological uses, they have been implemented in a variety of Ayurvedic formulations. It is used as ingredients in 'Brahma Rasayana' and 'Chyawanprash' for immune booster; Indian Siddha medicine 'Yelaathi Churanam' for treating Chancres, ulcers, leprosy; Ashwagandharishta for its cardioprotective properties (Asif et al., 2017); Dasamoolarishta, Mahakaleshwara rasa and various other churnas for treating various disease conditions. In Unani system, Jawarish Shehryaran is a tonic for stomach and liver problems; Halwa-isupari pack is a tonic for general uses and Hab Pachaluna as an appetizer (Arora et al., 2019; Chahar, 2013). In Thai traditional medicine, it is used as antiasthamatic, carminative, cardiotonic, expectorant, antipyretic and diuretic agent (Arora et al., 2019).

Due to extensive utilization in traditional medicines, its phytochemical extracts and their individual constituents were further explored and researched for specific biological activities. **Fig 1.9** summarizes the bioactivities reported from various extracts of *M. ferrea* (Arora et al., 2019; Asif et al., 2017; Sharma et al., 2017). As depicted in **Fig 1.9**, the extracts of seeds, leaves and flowers have been explored for a wide range of biological activities. However, their molecular mechanism of the crude extracts are not well studied.

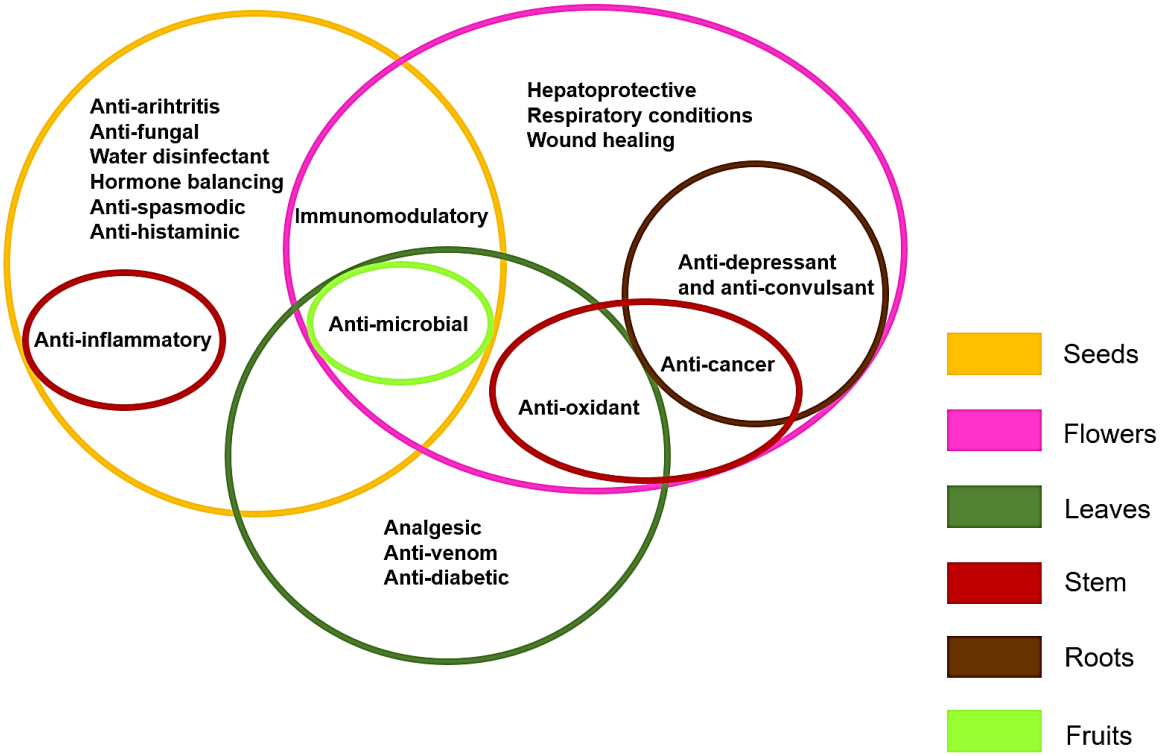

Figure 1.9: Schematic representation of the bioactivities of *M. ferrea* extracts of various plant parts

Phytochemical studies have revealed that the *Mesua* species are rich in a wide range of secondary metabolites like xanthones, phenylcoumarins, triterpenoids and so on (Chahar, 2013). Different secondary metabolites reported from different parts of the plant is tabulated in **Table 1.3**.

Table 1.3: Phytochemical constituents from different parts of *M. ferrea*

Source	**Phytochemical**	**Reference**
Seeds	Mesuol, Mesuagin, Mammeisin, Mesuagin, Mesuone, Mammeigin	Bala and Seshadri, 1971; Chahar, 2013; Sharma et al., 2017
Stamen	α- and β- Sitosterol, Mesuaferrones A and B, Euxanthone 7-methyl ether	Chahar, 2013; Raju et al., 1976
Stem bark	1,5-dihydroxyxanthone (II), Euxanthone 7-methyl ether (IV) and β-Sitosterol Mesuaxanthone A and Mesuaxanthone B Ferruol A, Ferrxanthone A	Chow and Quon, 1968; Govindachari et al., 1967b, 1967a; Walia and Mukerjee, 1984
Flowers	Mesuaferols D–F and iso-Mesuaferol F	Wang et al., 2020

Roots	Mesuaferrin C, Caloxanthone C, Macluraxanthone, 1,5-dihydroxyxanthone, Tovopyrifolin C, Mesuaferrin A and Mesuaferrin B, Caloxanthone C, 1,8-dihydro-3-methoxy-6-methylanthraquinone, β-Sitosterol, Friedelin, Betulinic acid	Teh et al., 2017, 2013, 2011
Leaves	12, 13-furano-8-hydroxy napthyl-6-0-β-2',3',4',6' tetrahydroxy-5',5' dimethyl cyclohexyl ether	Rahman et al., 2010

Apart from its medicinal benefits, it has various other applications like cosmetic production, synthesis of biosorbants and resins, feedstock production, biofuel production, environmental applications like phytoremediation, carbon sequestration, phytoremediation (Mitra et al., 2021).

Out of these phytochemicals reported, the focus of the thesis is on Mammeigin from seeds of *M. ferrea.*

1.7. Mammeigin from *M. ferrea* seeds

Mammeigin (MMG) is a neoflavonoid (IUPAC name: 5-hydroxy-8,8-dimethyl-6-(3-methylbutanoyl)-4-phenylpyrano[2,3-h]chromen-2-one). (**Fig 1.10**)

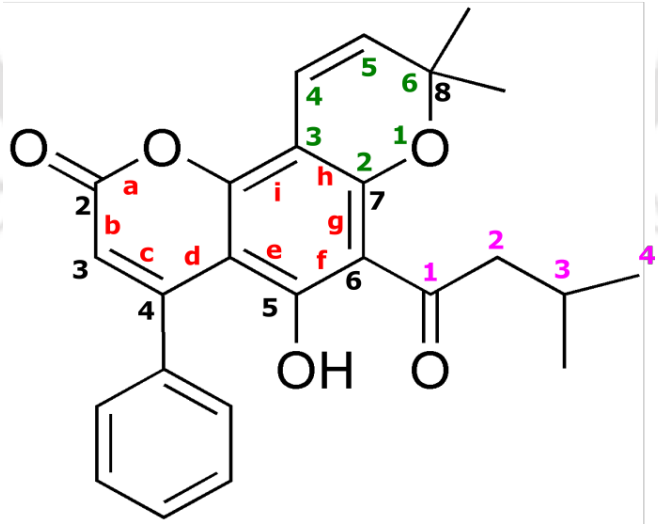

Figure 1.10: Structure of Mammeigin. [Numbering in black refers to the parent ring; numbering in green refers to fused pyran ring, numbering in pink refers to butanoyl side chain and letters in red refers to bonds of parent ring]

It was reported in *M. ferrea* seeds by Bala and Seshadri, (1971). The biological activities of this compound is tabulated in **Table 1.4**.

Table 1.4: Biological activities of Mammeigin reported

Bioactivity	Host / target molecule	Bioactive concentration	Solvent carrier	References
Anti-malarial	*Plasmodium falciparum* strain 3D7	1.02 µg/mL	-	Tanjung et al., 2016
	Plasmodium falciparum	45.62±3.12 µM	DMSO	(Chaniad et al., 2022)
Anti-cancer	SW-480, HT-29, HCT-116 (Human colon cancer)	32-42 µM	DMSO	Yang et al., 2005
	COLO205 and KM12 (Colon cancer)	> 1 mM	-	Cunha et al., 2016
	Human Recombinant Aromatase	7.2 µM	2% DMSO	Ninomiya et al., 2016
	P-388 (blood), KB (oral), Col-2 (colon), BCA-1 (breast), Lu-1 (lung) cell lines	>20 µg/mL	-	Reutrakul et al., 2003
	MCF-7 (breast), H-460 (lung), SF-268 (central nervous system)	>10 µg/mL	-	López-Pérez et al., 2005
	B cell-specific Moloney murine leukemia virus insertion region 1 (BMI1) promoter inhibitory activity against cancer cell lines (DU145, Huh7, and HCT116)	33.7 µM	DMSO	(Fujii et al., 2022)
	Sarcoma 180 tumor cells	>5 µg/mL	-	Finnegan et al., 1972
Androgen- related diseases	Testosterone 5-α-reductactase	> 100 µM	DMSO	Morikawa et al., 2020
Insecticidal	Mustard beetles, house flies	0.5 µg/mL	-	Crombie et al., 1972, 1970

Advanced glycation end-products (AGE) inhibition, Endothelial dysfunction	Vesperlysines-type AGE and Pentoside-type AGE	>3mM and 0.6 mM respectively	-	Dang et al., 2014
Anti-viral	HIV (Recombinant Virus)	123 µM	-	Bedoya et al., 2005
Anti-bacterial	Multi-drug resistant *Staphylococcus* and *Enterococcus* species	> 128 µg/mL	DMSO	Verotta et al., 2004

From the table, we can note that MMG has highest bioactivity as anti-malarial, anti-aromatase and insecticidal. There was also another report on antimalarial activity, which showed low activity (**Table 1.4**). In some cases, it displayed moderate activity like anti-cancer against certain colon cancer cells, while it showed average to poor activities in other biological assays. It can also be noted that the solvent carrier used was DMSO and has not been mentioned in most of the cases. MMG is a non-polar compound insoluble in aqueous medium. Therefore, at such low concentrations of DMSO, there is likely chance that MMG could have undergone precipitation. The extent of precipitation can depend on the percentage of DMSO used. Due to this, the effective concentration for bioactivity could be less and inconsistent leading to error in the results, as the case of antimalarial report cited in **Table 1.4**. There is a need for approaches that can increase the bioavailability of MMG for therapeutic applications. Based on this motivation, the objectives of the thesis were formulated.

1.8. OBJECTIVES OF THE THESIS WORK

The major challenge in testing of drug lead molecules and its development is the bioavailability, which is directly linked to its aqueous solubility and cell permeability properties of the molecule. MMG is a neoflavonoid compound from *M. ferrea* seeds, with potential but selective therapeutic properties. Therefore, surfactants of different charges were used as model to investigate MMG behavior in self-assembling entities. Like other plant polyphenols, MMG could display sensitivity to its surrounding environment. Therefore, in this thesis work, UV-Visible spectroscopic techniques were used to investigate the immediate solvent environment of MMG in organic, binary solvents, different pH conditions. Similarly interactions of MMG with surfactants and Hen Egg-White Lysozyme aggregates were explored. Lastly, the influence of salt on the MMG-surfactant interactions were investigated.

Therefore, the objectives of thesis work were decided as follows:

1. **Extraction, Isolation and Identification of Mammeigin from *M. ferrea* seeds.**
2. **Investigation of intrinsic spectroscopic properties of Mammeigin in various solvent environments including surfactant micelles**
3. **Investigating the spectroscopic properties of Mammeigin in Hen Egg-White Lysozyme aggregates.**
4. **Investigating Mammeigin as acid-base pH indicator in surfactant systems and its structural characterization in alkaline conditions**
5. **Investigating the effect of salts on the spectroscopic properties of Mammeigin in micro-heterogenous systems.**

Chapter 2

Extraction, Isolation and Identification of Mammeigin from *M. ferrea* seeds

2.1. Introduction

M. ferrea seed oil, commonly known as Nahor or Kesar oil is popular in the market for its high oil produce (Sahu et al., 2014; Sharma et al., 2017). The seeds produce yellow and malodourous oil of about 70-75 % yield (w/w) and the seed coat contains about 29% (w/w) of oil (Mitra et al., 2021). The oil consists of saturated and unsaturated fatty acids such as palmitic, stearic, arachidic, oleic, linoleic, hexadecenoic and octadecanoic acids (Arora et al., 2019; Chahar, 2013; Sahu et al., 2014). The seed oil has the potential to substitute petroleum gasoline, due to which *M. ferrea* is known as biofuel crop (Chahar, 2013). Biodiesel blends of *M. ferrea* with 10% diesel displayed improvements in exhaust emission features and engine performance (Mitra et al., 2021). Other potential applications of the seed oil includes natural disinfectant (Asif et al., 2017; Chahar, 2013), synthesis of biosorbants and resins (Chahar, 2013; Mitra et al., 2021), perfume and beauty products, nanofibers, nanocomposites, biomedical and biotechnological applications (Mitra et al., 2021).

M. ferrea is the most chemically well studied species of *Mesua* genus. They are rich in phytochemicals like phenylcoumarins, xanthones and triterpenoids (Chahar, 2013; Sharma et al., 2017). The seed oil is reported to have abundant 4-phenylcoumarins or neoflavonoids such as mesuagin, mammeigin, mammeisin, mesuone, mesuol, mesuarin (Bala and Seshadri, 1971; Chahar, 2013; Sahu et al., 2014; Sharma et al., 2017) (**Fig 2.1**).

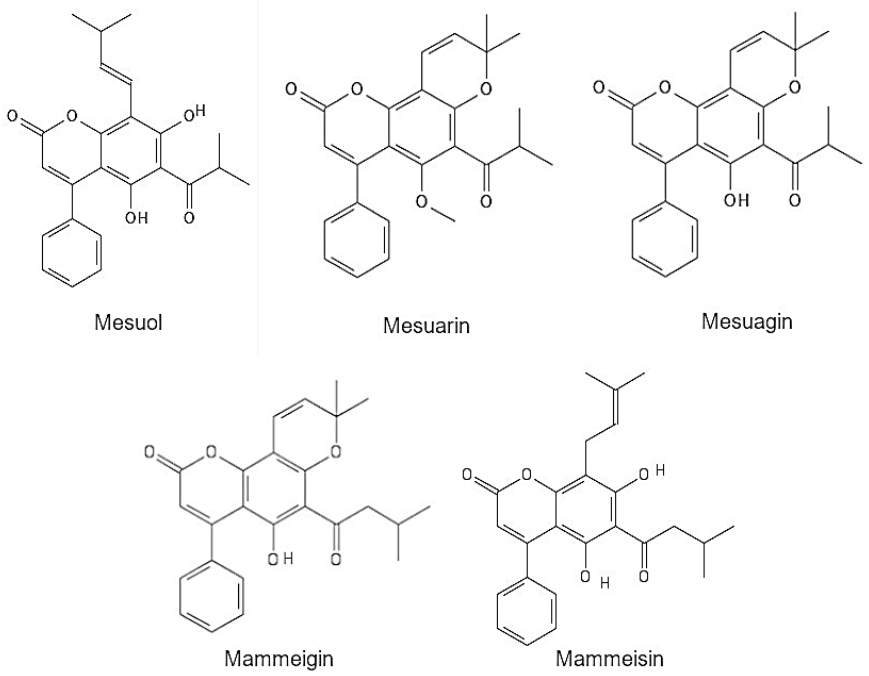

Figure 2.1: 4-phenylcoumarins reported in *M. ferrea* seed oil

These phytochemical pools from the seeds have various therapeutic benefits. For instance, *M. ferrea* seed extracts have shown anti-arthritis (Asif et al., 2017) and anti-spasmodic activity (Chahar, 2013) *in vivo*. The kernels are used to treat wounds, skin eruptions, cutaneous infection and embrocation in rheumatism (Arora et al., 2019; Chahar, 2013). Methanolic extract of the seed and few individual chemical constituents exhibited bioactivities against some strains of fungi and bacteria (Arora et al., 2019). The seed oil fraction containing phenols displayed anti-histaminic activity both *in vitro* and *in vivo* for isoprenaline-induced relaxation of tracheal smooth muscles (Arora et al., 2019). Apart from the extracts, individual compounds have also shown potential bioactivities. Mesuol has demonstrated immunomodulatory and hormone balancing activities (Arora et al., 2019; Asif et al., 2017), while mesuarin displayed antibacterial activities against gram positive and negative bacteria (Sahu et al., 2014). The toxicology studies conducted on rat models has revealed non-toxic nature of different extracts from *M. ferrea* seeds suggesting their safe usage (Asif et al., 2017).

Due to diversity in the chemical composition and applications of *M. ferrea* seed oil, this chapter focuses on extraction and isolation of Mammeigin from the seed oil. Firstly, oil extraction from mature seeds of *M. ferrea* is explained. Secondly, isolation and purification of polyphenolic compound from the seed oil through a series of steps is highlighted and lastly, characterization of its chemical structure using various analytical techniques is discussed.

2.2. Materials and methods

2.2.1. Sample collection

The seeds were collected from *M. ferrea* trees (**Fig 2.2 A**) growing in Indian Institute of Technology Guwahati (IIT Guwahati) campus during the months of April-June. Mature and partially mature fruits (**Fig 2.2 B**) were collected and packed in a closed, dark and near airtight environment for 3-4 days to speed up the ripening process. The mature seeds with fully brown colored seed shells were separated from the fruits, deshelled and the kernels were air-dried. The dried kernels were subjected to further processing or stored in dark at room temperature (**Fig 2.2 C**).

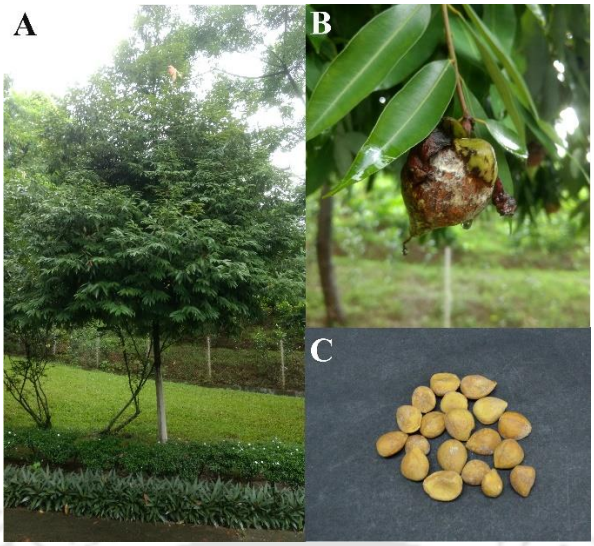

Figure 2.2: (A) *Mesua ferrea* tree in its natural habitat, (B) Partially mature fruit of *M. ferrea* and (C) Dried kernels of *M. ferrea*

2.2.2. Preparation of organic extracts

The dried seed kernels (50 g) were made into fine powder and subjected to Soxhlet extraction using n-hexane (Rankem, India) solvent. The extraction was done till the solvent in the extractor chamber was colorless, thus ensuring complete extraction. The hexane extract was then concentrated (using device discussed in Appendix section) to obtain seed oil. The seed oil was subjected to methanol wash to separate polar fraction from oil fats. Around 200 ml methanol (Merck, India) was added to the oil, vigorously shaken and allowed to separate in a separating funnel. The process was repeated four times and the methanol fractions obtained were pooled together. The fractions were concentrated and stored at room temperature (Bala and Seshadri, 1971).

2.2.3. Isolation and purification of polyphenolic compound

The methanolic re-extract of the seed oil was used as crude extract for further fractionation and isolation of compounds. The fractionation of the crude extract was carried by silica gel chromatography. A glass column (3 x 50 cm) was packed with silica gel 60-120 mesh (Merck, India) in hexane (Rankem, India). The column was well equilibrated prior to sample addition. For sample preparation, the crude extract was dissolved in acetone and added to a small amount of silica gel in a beaker. The solvent was allowed to air-dry completely overnight and the dried sample was loaded onto the pre-packed silica gel column. The sample was eluted as a step-wise gradient of ethyl acetate in hexane (Rankem, India). The elution of

compounds from the column was monitored by Thin Layer Chromatography (TLC) (silica gel 60 F254 0.25 mm, Merck, Germany) using appropriate solvent mobile phases. Based on the TLC, 10 fractions were obtained out of which 3 fractions seemed to have crystalline compounds. Out of those, the first fraction was further investigated as it was found to be consistent in every seed batch.

The fraction I was then purified using a series of techniques. Firstly, it was subjected to preparative TLC. The silica gel infused with calcium sulphate (Sisco Research Laboratories (SRL), India) was made into a slurry with water and added as a thin layer on glass slides. The silica plates were dried and baked to remove moisture. Fraction I extract was loaded onto the silica plates and run in mobile phase of 5% ethyl acetate in hexane. Three bands were separated from the fraction and scrapped off from the silica plates. They were added with acetone and filtered to remove silica gel. The band 3 yielded mixture containing crystalline compound.

The band 3 filtrate from preparative TLC was subjected to multiple rounds of re-crystallization in the aqueous acetone, acetonitrile and ethanol, sequentially. The impurities formed white colloidal suspension, which were separated from the crystalline fraction by careful pipetting in each round. Before the subsequent round of re-crystallisation, the crystals were washed with deionised water. This process of re-crystallization was carried out till the bulk solution was clear of major impurities. To further remove minute impurities adhering on the crystal surfaces, the sample was purified using reverse phase-high performance liquid chromatography (RP-HPLC). The stationary phase was C18 column (250 x 4 mm), mobile phase employed was 5-100% acetonitrile in water (0-10 min); 100 % acetonitrile (10-15 minutes); 5% acetonitrile in water (15-25 minutes) and detected at 286 nm. The retention time of the compound was 18.2 min. The solvents used were HPLC grade (Merck, India), which were filtered and degassed prior to use. The purified sample obtained from RP-HPLC was lastly subjected to two rounds of re-crystallization in mixtures of distilled ethanol (Merck, Germany) and water. The purified compound (named C1-S-MF) obtained was dried and stored in dark at room temperature in crystalline form until further use.

2.2.4. Structural characterization of C1-S-MF

To elucidate the chemical structure of isolated compound, the following techniques were applied:-

2.2.4.1. Fourier Transform - Infrared Spectroscopy (FT-IR): FT-IR (Shimadzu IRAffinity-1S) analysis was carried out to identify the chemical groups in the C1-S-MF. About 1 mg of C1-S-MF was crushed to fine powder along with 10 mg of anhydrous potassium bromide (Himedia IR grade, India) and made into a thin disc of 1 mm thickness with hydraulic pressure. The disc was then mounted onto sample holder and spectra was collected in the range of 400-4000 cm^{-1}.

2.2.4.2. Liquid Chromatography - Mass Spectrometry (LC-MS): The analysis was carried out in Waters ACQ-TQD, QBB1152 using Electrospray Ionization (ESI) method. The sample was separated through LC prior to MS. The molecular mass was recorded in positive ion and negative ion modes.

2.2.4.3. Nuclear Magnetic Resonance (NMR) : The C1-S-MF of nearly 1.5 mg was dissolved in 650 µl of deuterated chloroform ($CDCl_3$) (Merck, Germany) and added to 5 mm NMR tube. NMR analysis like ^{1}H, ^{13}C, Correlated Spectroscopy (COSY), Heteronuclear Single Quantum Coherence spectroscopy (HSQC), Distortionless Enhancement by Polarization Transfer 135º (DEPT 135º) were carried out in Bruker Ascend 600 MHz. The $CDCl_3$ peak (δ) at 7.26 ppm for ^{1}H NMR and 76.7 ppm for ^{13}C NMR were used as reference. The spectra were analysed using MestRenova software.

2.2.4.4. Single Crystal - X-Ray Diffraction (SC-XRD): The exact structure of C1-S-MF was confirmed using SC-XRD (Agilent). A highly concentrated solution of C1-S-MF was dissolved in acetonitrile and allowed to undergo slow evaporation at room temperature. Rod shaped crystals were formed from which single crystals were selected and stored in silicone oil on a glass slide, which was analysed by XRD. The structure was solved and refined using crystal ALISpro and Autochem software. Crystal data like cell parameters, cell density, chemical formula, crystal space group were obtained. The crystal structure was visualized and analysed using Mercury software.

2.2.4.5. UV-Vis spectroscopy: C1-S-MF was dissolved in ethanol and UV-Vis absorption spectra were collected in the range of 220-500 nm in Perkin Elmer Lambda 25 spectrophotometer. The absorption maxima (λ_{max}) from the spectra was noted and compared with the literature.

2.2.4.6. Biochemical test: Ferric chloride test was carried out for C1-S-MF (Pasto, 1979 with modifications), where 1 mg of C1-S-MF was dissolved in 1 ml of ethanol. To this, 1-2 drops

of 1% (w/v) aqueous ferric chloride was added. The colour change was noted and compared with control (without ferric chloride). The results were matched with the reported literature.

2.3. Results and Discussions:

2.3.1. Quantification and Qualification of C1-S-MF

M. ferrea is a biofuel plant and has a high oil yield. From 50 g of seeds, 38.1 g seed oil of 42.5 mL volume was obtained. Thus, the density of *M. ferrea* seed oil was determined to be 0.89 g/L, similar to the reported value (Bora et al., 2013). The oil yield in the seeds collected from IIT Guwahati campus was 76.18 % (w/w of seeds) which was in the range reported (Konwer et al., 1989). The crude extract for isolation of polyphenolic compound obtained from *M. ferrea* seed oil was 9.47 g after methanol re-extraction. Upon fractionating the crude extract through silica gel chromatography, the desired fraction obtained was 2.3 g. After purification using preparative TLC, multiple rounds of re-crystallization and RP-HPLC purification, the purity of the final product was 99% (**Fig 2.3**).

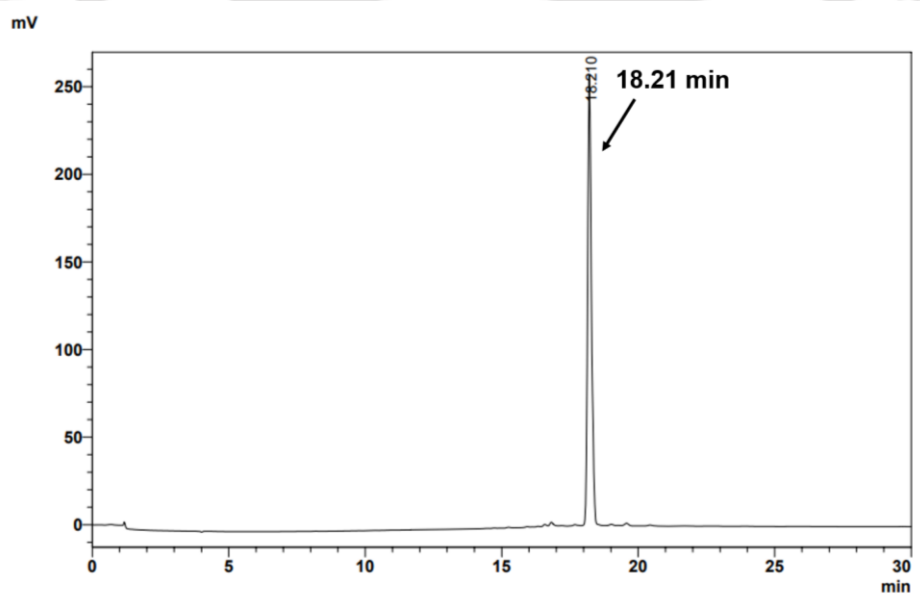

Figure 2.3: RP-HPLC chromatogram of purified C1-S-MF with detection at 286 nm. The retention time of C1-S-MF was 18.2 ± 1.1 minutes.

The purified compound was yellow coloured needle shaped crystals (**Fig 2.4**). The C1-S-MF obtained after purification was 320.15 mg and thus the yield obtained was 0.64 % (w/w of seeds).

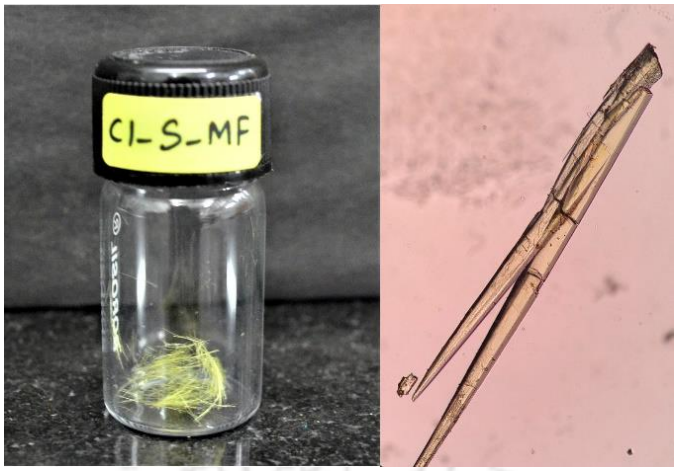

Figure 2.4: Purified C1-S-MF morphology and microscopic image (40X)

2.3.2. Structural characterization of C1-S-MF

2.3.2.1. Fourier transform – Infrared spectroscopy (FT-IR)

The chemical groups of C1-S-MF were identified through FT-IR analysis (**Fig 2.5**).

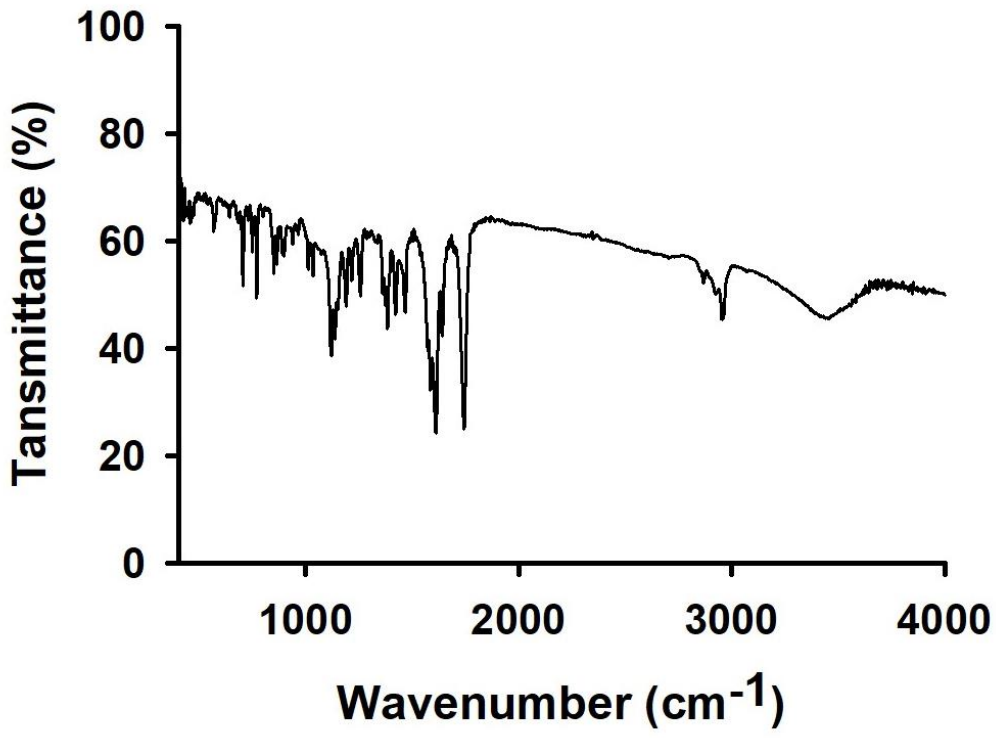

Figure 2.5: FT-IR spectra of C1-S-MF using KBr method

Sharp peak at 1737.9 cm^{-1} was distinctive of carbonyl group and broad peak at 3458.4 cm^{-1} represented hydroxyl group. Repetitive sharp peaks in the range 1776.4 – 1965.5 cm^{-1} referred to phenyl overtones and C-C phenyl stretch at 1614.4 cm^{-1} suggested the presence of

aromatic group(s). Peak at 769. 6 cm^{-1} corresponded to out of plane (OOP) bending of C=C-H bonds of alkenes substituent patterns or aromatic systems. Peaks at 2870.1 cm^{-1}, 1737.9 cm^{-1} and 2960.7 cm^{-1} referred to methylene C-H stretch, C=O group and C-H alkyl stretch respectively, that could correspond to possible side groups. Two fork like peaks at 1423.5 cm^{-1} and 1467.8 cm^{-1} were signatures for C-H methyl bends. **Table 2.1** lists the signature peaks of possible chemical groups in C1-S-MF.

Table 2.1: FT-IR peak signatures of C1-S-MF and corresponding chemical groups

Wave number (cm^{-1})	Peak signature
769.6	OOP C=C-H
1423.5, 1467.8	C-H Methyl Bend
1614.4	C-C phenyl stretch
1737.9	C=O
1776.4-1965.5	Phenyl overtones
2870.1	Methylene C-H stretch
2960.7	C-H alkyl stretch
3458.4	-OH

2.3.2.2. Liquid Chromatography – Mass Spectrometry (LC-MS)

The compound was subjected to LC to separate it from minor impurities followed by MS in positive and negative modes. The positive mode yielded mass of 405.4 Da representing $[M+H]^+$ (**Fig 2.6A**), while the negative mode yielded 403.2 Da representing $[M-H]^-$ (**Fig 2.6B**). Thus the molecular mass of the compound was 404 Da.

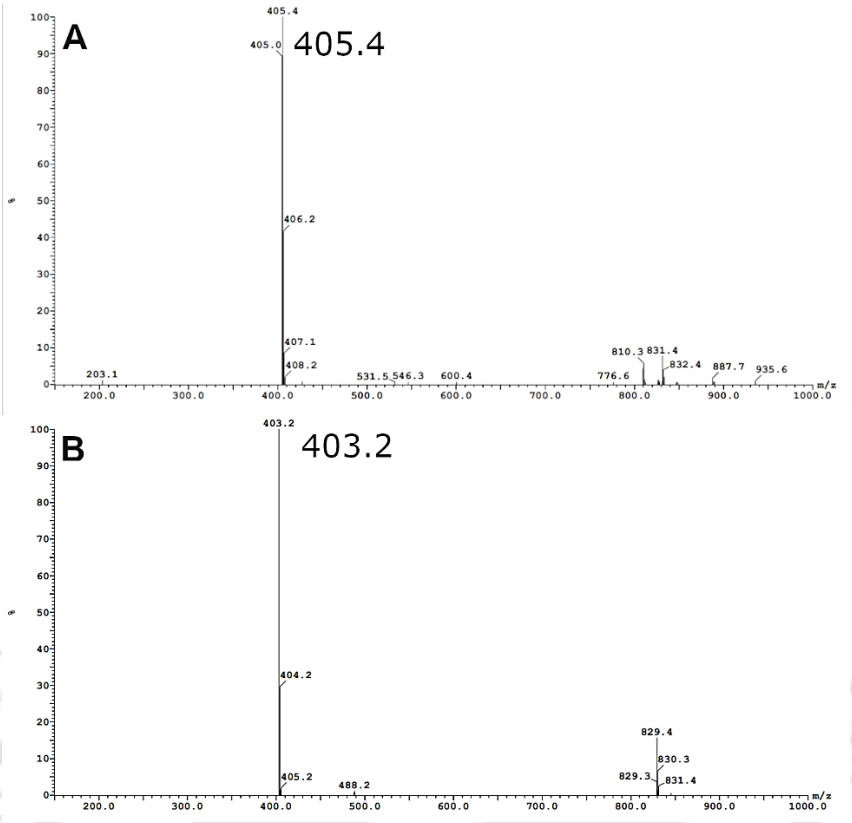

Figure 2.6: Mass spectrometry analysis of C1-S-MF using ESI method in (A) positive mode and (B) negative mode

2.3.2.1. Nuclear Magnetic Resonance (NMR)

The final structure of the compound was derived from NMR analysis. One dimensional NMR - ^{1}H and ^{13}C spectra (**Fig 2.7 A & B**) were correlated with FT-IR results to identify and correlate the chemical groups. For example in ^{1}H NMR spectra, multiplet peaks at 7.31-7.39 ppm represents the aromatic rings, singlet at 14.83 to -OH group, high intensity peaks integrating to 6H at 1.63, 1.62 ppm and doublet at 0.98 ppm clearly represented pairs of methyl groups suggesting presence of secondary carbon/branched hydrocarbon side chains. In ^{13}C spectra, peaks in the range of 100-160 ppm corresponded to aromatic rings or alkylene substitutions, the peaks below 100 pm represented alkyl side groups and 206.8 ppm corresponded to carbonyl group due to high deshielding.

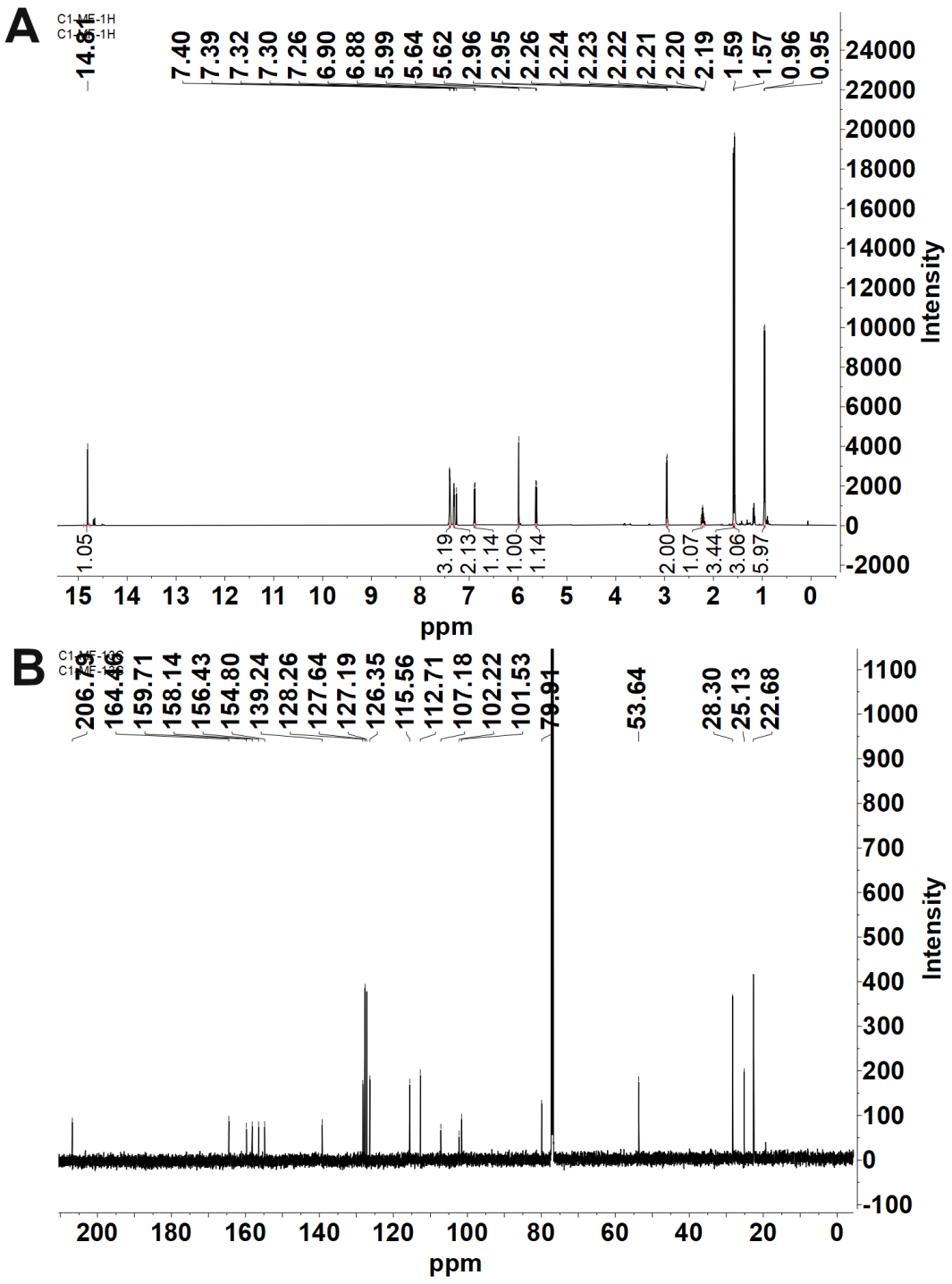

Figure 2.7: (A) ^{1}H NMR spectra (B)^{13}C NMR spectra of C1-S-MF

The whole structure was elucidated with the help of two-dimensional NMR spectra like COSY (^{1}H-^{1}H), HSQC (^{1}H-^{13}C) and DEPT 135º. COSY analysis revealed correlation between 6.89 pm and 5.63 ppm doublet peaks which represents ethylene group in a ringed structure (**Fig 2.8A**).

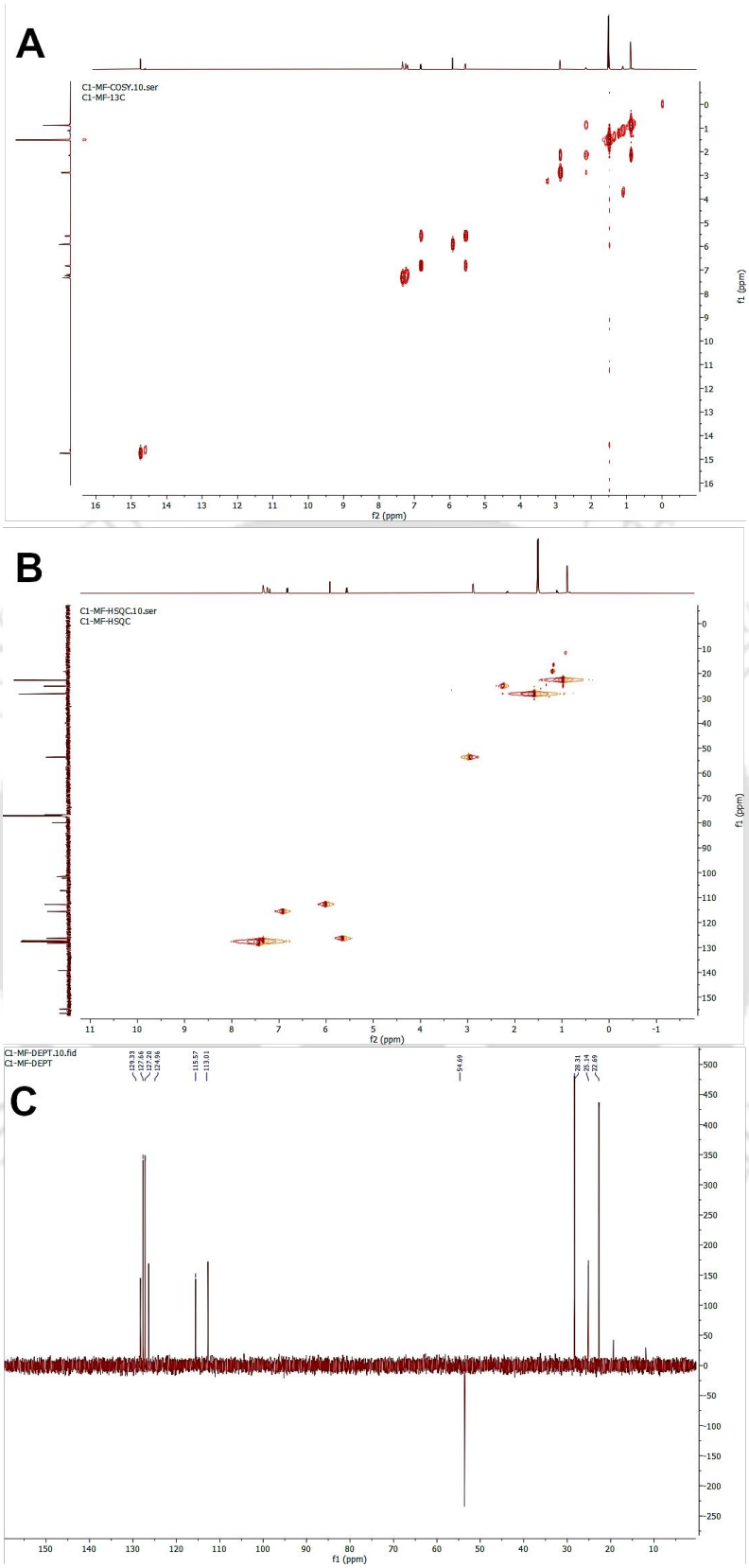

Figure 2.8: (A) Correlation Spectroscopy (COSY), (B) Heteronuclear Single Quantum Coherence spectroscopy (HSQC), (C) Distortionless Enhancement by Polarization Transfer 135º (DEPT 135º) analysis of C1-S-MF

Also correlation between 2.95 ppm and 2.22 pm; 2.22 pm and 0.96 ppm, correspond to alkyl group substituent. The HSQC analysis confirmed the interpretations of ^{13}C spectra and the DEPT 135º revealed that 53.6 ppm peak in ^{13}C spectra belongs to -CH_2, which was also backed by HSQC spectra and the splitting pattern of 2.95 ppm in ^{1}H spectra (**Fig 2.8B & C**).

The conclusions of the NMR analysis is tabulated in **Table 2.2** and the labelled compound interpreted from the results. Thus compiling the results from the NMR spectra, FT-IR and also LC-MS, the structure of C1-S-MF was elucidated to be Mammeigin (MMG) (**Fig 2.9**), a 4-phenyl coumarin reported from *M. ferrea* previously (Bala and Seshadri, 1971). The experimental NMR spectra were also matched with the reported values (Verotta et al., 2004) for further confirmation.

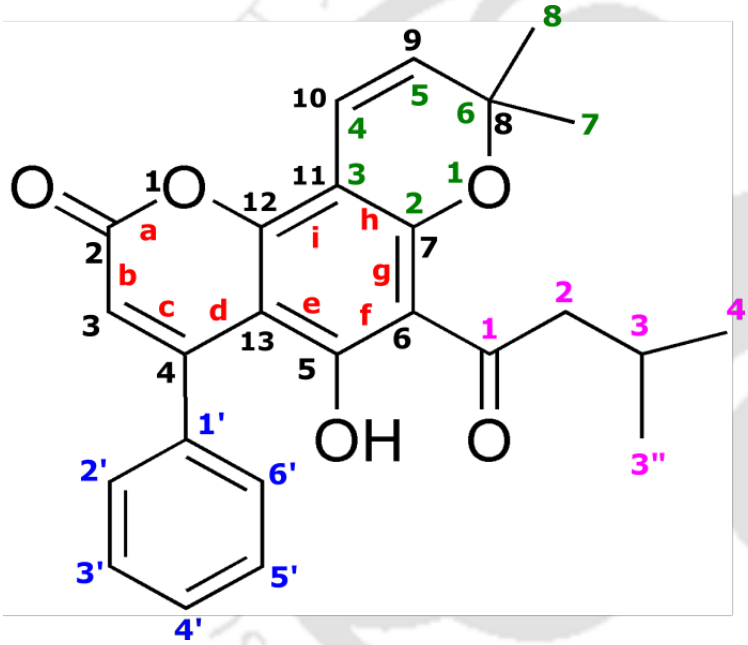

Figure 2.9: Structure of C1-S-MF (Mammeigin). Numbered according to IUPAC name: 5-hydroxy-8,8-dimethyl-6-(3-methylbutanoyl)-4-phenylpyrano[2,3-h]chromen-2-one. [Number Label of each part of the compound is colour coded. Black – Parent ring; Blue – Phenyl ring; Green – Fused pyran ring; Pink – butanoyl side chain; Red – Bonds of the parent ring]

Table 2.2: ^{1}H and ^{13}C NMR analysis of C1-S-MF (Colour coded atom numbering as per **Fig 2.9**)

Atom labelling	^{1}H (δ in ppm, J in Hz)	^{13}C (δ in ppm, J in Hz)
2		159.7
3	5.99, s	112.71
4		156.43
5		164.46
6		107.18
7, 2		154.8
8, 6		79.91
9, 5	5.63, d (J=12.0 Hz)	126.35
10, 4	6.89, d (J=12.0 Hz)	115.56
11, 3		101.53
12		158.14
13		102.22
1'		139.29
2' and 6'	7.39-7.31, m	127.19
3' and 5'		127.64
4'		128.26
7 and 8	1.59, 1.57, s	28.30
1		206.79
2	2.95, d (J=6.0)	53.64
3	2.22, sept	25.13
3" and 4	0.96, d (J=6.0 Hz)	22.68
-OH group	14.83, s	

2.3.2.4. Single Crystal – X-Ray Diffraction (SC – XRD)

The validation of the structure elucidated using the above techniques was carried out by SC – XRD. The chemical formula of the compound generated was $C_{25}H_{24}O_5$. Based on the cell parameters (**Table 2.3**), the crystal space group was found to monoclinic (Cc) (**Fig 2.10**).

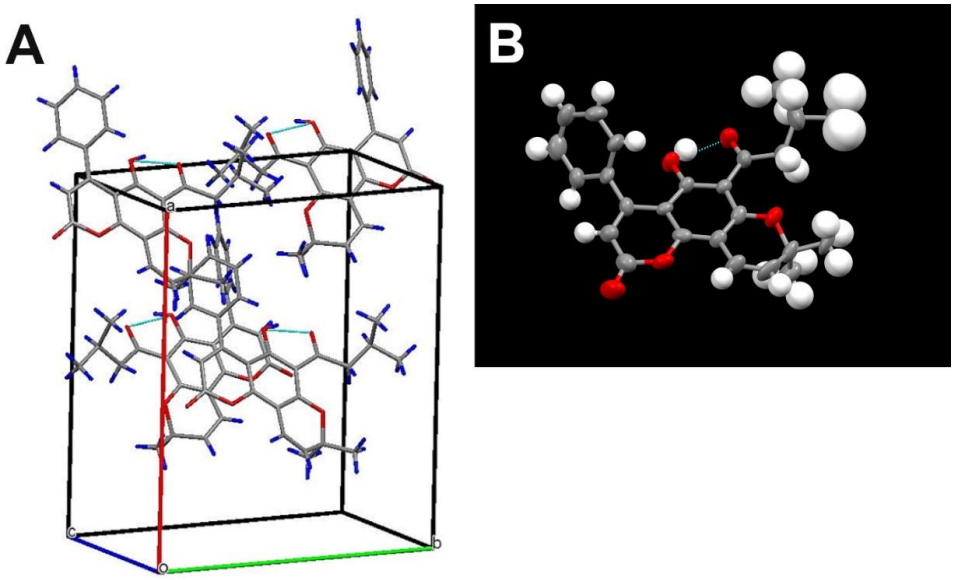

Figure 2.10: (A) Crystal packing of C1-S-MF in a unit cell, (B) Ball and stick plot of the molecular structure

Table 2.3: Crystal data of C1-S-MF

Parameters	**Crystal data**
Chemical formula	C_{25} H_{24} O_5
Chemical formula weight	404.4 g/mol
Crystal morphology	Yellow needle shaped
Crystal space group	Monoclinic (Cc)
Cell parameters	a= 16.989 ; b= 14.3162 ; c= 8.7884 α= 90.0° ; β= 90.003° ; γ= 90.0°
Cell formula units	4
Cell volume	2137.6
Refinement method	SHELXL-97, Olex 2

Each cell had 4 units and the cell volume was 2137.6 cubic units. The SC-XRD results matched the reported crystal data of MMG (Doriguetto et al., 2006). Based on these facts, the compound was confirmed to be MMG. This result was also useful in distinguishing from other possible isomeric forms of MMG, which otherwise would yield similar results in the above techniques mentioned.

2.3.2.5. UV-Vis absorption spectroscopy and Biochemical test

Further confirmation was also carried out by comparing absorption spectral peaks of the compound. The absorption spectrum of the compound in ethanol yielded λ_{max} at 234 nm, 286 nm and 369 nm (**Fig 2.11A**), which matched with the reported values (Nagem and Silva, 1988).

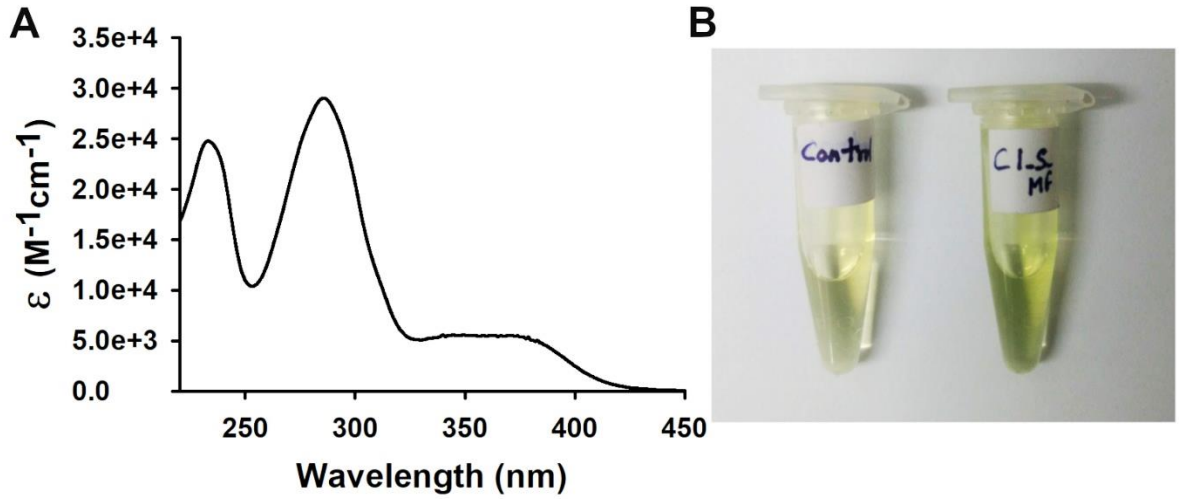

Figure 2.11: (A) UV-Vis Absorption spectrum of C1-S-MF (B) Ferric chloride test of C1-S-MF

Ferric chloride test is commonly used test to distinguish between compounds with different chemical substitutions or isomeric forms. Ferric chloride was used to identify the right isomer of MMG (Nagem and Silva, 1988), where addition of 1% aq. ferric chloride to ethanolic solution of the compound was carried out. The isolated compound resulted in distinctive olive green colour formation which was different from the pale yellow coloration of the control (without ferric chloride) (**Fig 2.11B**). Thus the isolated and purified compound was characterized and confirmed to be Mammeigin (MMG).

MMG was first identified in *Mammea americana* (Finnegan and Mueller, 1965) and later in *M. ferrea* seeds and flowers (Bala and Seshadri, 1971; Verotta et al., 2004). It belongs to neoflavonoid (4-phenylcoumarins), a subcategory of polyphenols which are less abundant in plant kingdom. MMG is reported predominantly in plant species belonging to Calophyllaceae of *Mammea* genus (Carpenter et al., 1971; Finnegan and Mueller, 1965; Ninomiya et al., 2016; Reutrakul et al., 2003), *Mesua* (Bala and Seshadri, 1971; Bandaranayake et al., 1975), *Marila* (López-Pérez et al., 2005) and *Kielmeyera* (Cruz et al., 2001; Gramacho et al., 1999; Nagem and A. e Silva, 1988; Nogueira et al., 2008). The yield

of MMG using the procedure followed in this work, was found to be higher than reported in the literature so far. This could as a result of better combination of techniques used in our method or due to naturally lower amounts of MMG in other plant species reported. Thus, the procedure optimized in this work resulted high yield of MMG (0.64 % w/w) with the purity of 99%.

2.4. Conclusions

M. ferrea seeds were investigated for isolation of polyphenolic compound. Seed oil of yield 76.18 % (w/w) was obtained by Soxhlet extraction. The seed oil was subjected to further processing and fractionation. The first fraction was subjected to purification procedures like preparative TLC, recrystallization and RP-HPLC. The purified compound was yellow coloured needle shaped crystals with purity of 99%. The compound was characterized to be Mammeigin, which was previously reported from this plant. The overall yield of MMG was 0.64 % (w/w of seeds), higher than the previous reports.

Chapter 3

Investigation of Intrinsic Spectroscopic properties of Mammeigin in various solvent environments including surfactant micelles

3.1. Introduction

Neoflavonoids are a group of natural compounds belonging to flavonoid class, based on the 4-phenylcoumarin backbone (Garazd et al., 2003). Depending on the substitution pattern and plant sources, they are categorized into 4-arylcoumarins (neoflavones), 4-arylchromanes, dalbergiones and dalbergiquinols (Kumar et al., 2020). Due to the aromatic structure, the electron distribution of such compounds makes them susceptible to the surrounding environment. Solvent is characterized by molecular properties like dipole moment, electronic polarizability, Hydrogen bond donor and Hydrogen bond accepting properties (Reichardt, 2007). Such solvent properties influences the solubility, hydrophobicity, spectroscopic properties and biological activities of the dissolved compound (Liu and Guo, 2006a). The chemical structure of Mammeigin (**Fig 1.10 and 2.9**) consists of three aromatic rings and the chemical substituents like pyran ring, carbonyl, hydroxyl and alkyl groups which could influence its chemical properties and in turn spectroscopic properties in different solvent systems.

Neoflavonoids have been reported to display a variety of *in vitro* biological activities and therapeutic roles in traditional medicines (Kumar et al., 2020). In terms of biological potential, MMG is reported to show high insecticidal activity by targeting the oxidative phosphorylation of the insect host (Crombie et al., 1970). It is also reported for high anti-malarial activity than chloroquine (Tanjung et al., 2016) and high anti-aromatase activity (Ninomiya et al., 2016). Otherwise, it displayed moderate anti-oxidant (Tanjung et al., 2016; Yang et al., 2005), anti- cancerous (López-Pérez et al., 2005; Reutrakul et al., 2003; Yang et al., 2005), testosterone 5-α reductase inhibition (Morikawa et al., 2020), endothetial dysfunction (Dang et al., 2014b), anti-HIV activities (Bedoya et al., 2005) and antibacterial (Verotta et al., 2004) activities.

Majority of the drugs and therapeutic molecules are non-polar, which affects their solubility, stability and bioavailability in biological systems (Mondal et al., 2016). Thus, focus on development of effective drug carrier systems is the key for their safer delivery to the target sites. Encapsulation in self-assembling molecular entities like surfactant micelles is one such technique. They have been found to protect the drug molecules from adverse environmental conditions and facilitate drug absorption. Several pharmacological and pharmacokinetic properties of the drug and their efficacy can be predicted through drug and micelles interaction studies (Saraf et al., 2018). These molecular organized assemblies not

only share similarities to the cell, membranes and proteins in biological systems, but also have rich diversity in their microstructures (Liu and Guo, 2006b). They have benefits over other methods due to smaller hydrodynamic size, enhanced cell permeability and ease of large-scale production (Lu et al., 2018). Micelle systems differ from surrounding bulk solution due to restricted movement of water molecule in the confined system of micelles, which influences various characteristic properties (Bhattacharyya and Bagchi, 2000). Therefore, their stability and physical properties are influenced by chemical nature of the surfactant, charge on the surfactant, temperature, nature of the bulk solution and presence of additives like salts, polyelectrolytes and so on (Mabrouk et al., 2021; Prajapati and Patel, 2012; Qazi et al., 2020).

This chapter focuses on investigating the spectroscopic behaviour of MMG in organic solvents of different dielectric constants and binary solvent systems. It also investigates the interaction of MMG with surfactant micelles. The role of surfactant charges and the presence of salt additives on interaction, solubilization and stability of MMG was investigated.

3.2. Materials and Methods

3.2.1. UV-Vis absorption of MMG in organic and binary solvent systems

UV-Vis spectroscopic studies of MMG in different organic solvents of increasing dielectric strengths (**Table 3.1**) were carried out in Perkin Elmer Lambda 25 spectrophotometer, in the range of 220-600 nm. Organic solvents used for spectroscopic studies were of HPLC grade (Merck, India) and de-ionized water (Merck Millipore) was used.

Table 3.1 : Dielectric constants (k) of different solvents under investigation at 25^{o}C

Solvent	Dielectric constant (k) at 25 ^{o}C
Hexane	1.88
Ethyl acetate	6.02
Ethanol	24.55
Methanol	32.7
Acetonitrile	37.5
Water	78.4

Extinction coefficient of MMG in different solvents was determined by Beer-Lamberts law (Valeur and Berberan-Santos, 2012) –

$$A = log_{10} \frac{I_0}{I} = \varepsilon cl \quad \text{..... (3.1)}$$

Where 'A' is absorbance of the sample, 'I_0'and 'I' are the intensity of the incident light and the transmitted light respectively, 'Ɛ' is molar extinction coefficient of the sample, 'c' is the concentration and 'L' is the path length of the sample cell. The Ɛ was estimated from slope of absorbance vs concentration of compound (5 µM, 10 µM, 12 µM, 15 µM, 17 µM, 20 µM) for each of the solvent. The Ɛ of MMG was initially determined in ethanol and further used to calculate concentration of MMG. To determine Ɛ for other solvents, the MMG stock was prepared in ethanol and then diluted such that the concentration of ethanol in the samples was ≤ 0.2 % (v/v).

To study the absorption properties of MMG in binary solvent system, MMG (10 µM) was added to binary mixtures, with increasing concentrations of water in ethanol from 0-99 % (v/v). Absorption spectrum was collected for different combinations of solvent composition. The reverse was also carried out where concentration of ethanol was increased from 1-100 % (v/v) and absorption spectrum was recorded.

3.2.2. Preparation of surfactants

MMG was investigated in three surfactants of different charges – Sodium dodecyl sulphate (SDS) (negatively charged), Cetyltrimethylammonium bromide (CTAB) (positively charged) and Tween 20 (T20) (neutral) (**Fig 3.1**).

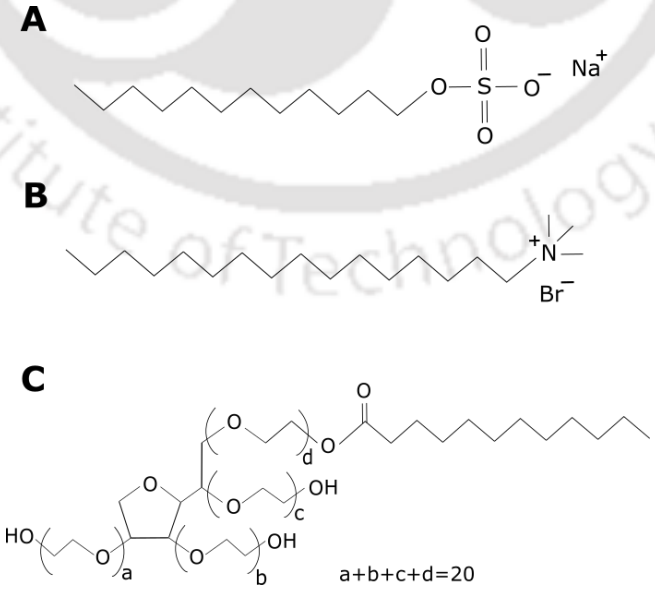

Figure 3.1: Chemical structure of surfactants, (A) SDS, (B) CTAB and (C) T20

For preparation of surfactant micelles, stock solutions were prepared at surfactant concentrations higher than their Critical Micelle Concentration (cmc), i.e., SDS (20 mM), CTAB (5 mM) and T20 (0.5 mM). The stock solutions were placed in mild hot water bath for a short period of time for complete solubilization (this step was not carried out for T20). The solutions were brought down to room temperature for further use. The stock solutions were always freshly prepared for experiments.

3.2.3. Optimization of co-solvent concentration for surfactant systems

For optimizing the concentration of ethanol co-solvent for solubilizing MMG in the surfactant micelle systems, MMG from ethanol stock was diluted in surfactant micelle solution, such that the MMG concentration was 15 µM and ethanol concentrations of 1 - 5% (v/v). The samples were vortexed at room temperature for 5 minutes and incubated over 1 hr prior to collecting absorption spectra. Absorbance of MMG at 287 nm was noted and compared for each ethanol concentration in the sample.

3.2.4. Determining extinction coefficient in surfactant micelles

Extinction coefficient in SDS (20 mM), CTAB (5 mM) and T20 (0.5 mM) was determined using Beer-Lambert law (**Equation 3.1**) using MMG concentrations of 10 µM, 12 µM, 17 µM, 20 µM and 22 µM.

3.2.5. Absorption of MMG at different surfactant concentrations

Absorption spectra of MMG (15 µM) in different concentrations of surfactants, SDS (0-19 mM), CTAB (0-4 mM) and T20 (0-0.4 mM) were investigated. Absorbance of MMG at the λ_{max} 234 nm, 287 nm and 374 nm was plotted against different concentrations of surfactants. Further to investigate the effect of salt, 200 mM of sodium chloride was added to the samples of MMG (15 µM) in different concentrations of surfactants.

3.2.6. Stability of MMG in the surfactant micelles

In order to investigate the stability of MMG in the surfactant micelles at room temperature (26-32 ºC) over time, MMG at 15 µM concentration was added to SDS (20 mM), CTAB (5 mM) and T20 (0.5 mM) micelles. Absorption spectra were recorded and absorbance at 287 nm was noted at time intervals of 1 hr, 2.5 hrs, 12 hrs and 24 hrs.

3.2.7. Investigation of fluorescence properties

Fluorescence of MMG was recorded in organic solvents, binary solvents system and surfactant micelle systems, at λ_{ex} 286 nm and 369 nm in HORIBA FluoroMax Plus 4C spectrofluorometer. Fluorescence quantum yield (Q_F) of MMG in the above mentioned solvent systems were determined using a standard reference fluorophore for appropriate wavelengths (Brouwer, 2011). The Q_F of MMG was determined at λ_{ex} = 369 nm for which Quinine sulphate (QS) (Laboratory Rasayana, India) was used as standard reference. The concentration of MMG was kept the same (1 μM) and the absorbance (O.D) in each solvent system was noted. The concentration of standard was taken such that its absorbance ($O.D_R$) was less than 0.04 and their values were noted for each wavelength. Fluorescence spectrum was collected and integrated for MMG (I) and for the standard (I_R) in the range of 386-800 nm. The excitation slit of 2 nm and emission slit of 10 nm was kept constant for all the sample readings. For fluorescence emission collected at λ_{ex} = 369 nm, 490 nm long pass filter was used to remove second diffraction peak. Refractive indexes of the solvents were acquired at 25 ºC using DR-A1 Abbe Refractometer (Atago, Japan).

The Q_F of MMG was calculated using the equation below –

$$Q_F = Q_R \frac{I}{I_R} \frac{O.D_R}{O.D} \frac{n^2}{n_R^2} \quad \text{..... (3.2)}$$

Where, Q_F is the quantum yield of the sample, Q_R is the quantum yield of the reference, I is the integrated fluorescence intensity of the sample, I_R is the integrated fluorescence intensity of the reference, O.D is absorbance of sample, $O.D_R$ is absorbance of reference, n is refractive index of sample and n_R is refractive index of standard.

3.3. Results and Discussion

3.3.1. Spectroscopic properties of MMG in neat organic solvents

Absorption spectrum of MMG was investigated in hexane, ethyl acetate, ethanol, methanol and acetonitrile. It displayed three absorption bands - Band I (232-234 nm), band II (286-370 nm) and band III (332-370 nm) (**Fig 3.2A**). The highest absorbing peaks (band I and II) could correspond to S_0-S_2 transitions and the weak band III due to S_0-S_1 transitions.

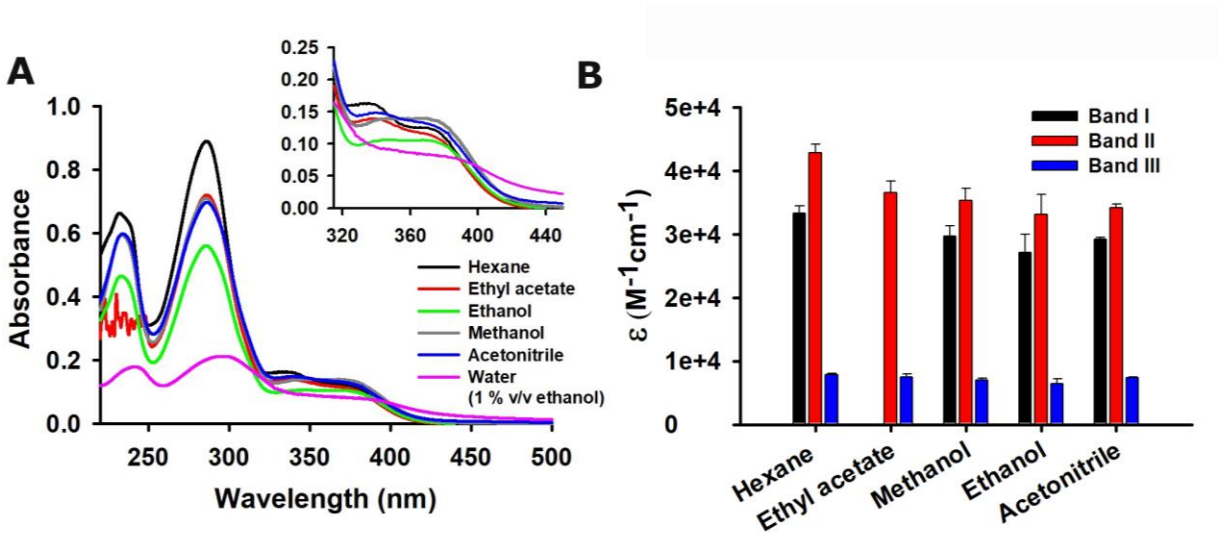

Figure 3.2: (A) Absorption spectra of MMG in different organic solvents. Inset: Band III (332-370 nm). (B) Extinction coefficient (Ɛ) in different organic solvents [Band I of MMG in ethyl acetate was omitted due to spectral overlap with solvent intrinsic absorption]

The bands I and II were similar in all the solvents, while Band III was slightly susceptible to the solvent type. In hexane and ethyl acetate, the band III resolved into two peaks i.e., 332-339 nm and 369-370 nm (**Fig 3.2A inset**). The presence of 339 nm peak was also observed in acetonitrile. The intensity of 332-339 nm peak was higher than 369 nm peak in these aprotic solvents. Resolution of this peak was lost in protic solvents like ethanol and methanol, that have hydrogen bonding properties. However, the 332-339 nm peak was not entirely diminished, resulting in a broad shoulder with slightly higher intensity at 369 nm in methanol and ethanol. It can thus be suggested that the 339 nm peak corresponds to group or moiety of MMG involved in intramolecular hydrogen bonding, which existed more in aprotic solvents than in protic solvents.

Overall, the absorption spectra of MMG showed low sensitivity to solvents of different polarities. Such less evident shift indicated that the ground-state energy distributions were unaffected in the solvents, mostly due to non-polar nature of the compound in its ground-state than in the excited state (Evale et al., 2009). It also holds for compounds undergoing local transitions, which does not involve strong intermolecular hydrogen bonding with the solvent or non-existence of charge transfer bands (Homocianu et al., 2011).

Molar extinction coefficient (Ɛ) was determined for MMG in the organic solvents using Equation 3.1 to compare their absorption properties, relative solvent environments and also determining concentration of MMG. The Ɛ for MMG in ethanol was determined initially,

i.e., $\varepsilon_{233\ nm}$ = 27405.33 ± 3423 $M^{-1}cm^{-1}$, $\varepsilon_{286\ nm}$ = 33110.67 ± 4188.5 $M^{-1}cm^{-1}$ and $\varepsilon_{369\ nm}$ = 6450 ± 837 $M^{-1}cm^{-1}$, which was found to be comparable to the reported values (Nagem and Silva, 1988). The $\varepsilon_{286\ nm}$ in ethanol was used to estimate concentration of MMG in ethanol stock and appropriate dilutions were made to prepare samples for all the upcoming experiments. When comparing ε of MMG in different solvents, the highest value was obtained for hexane and lowest in ethanol (**Fig 3.2 B**), which further suggested non-polar nature of MMG. Overall, ε was nearly the same for all the organic solvents under investigation. **Table 3.2** summarizes the ε obtained in the organic solvents at absorption maxima of the three bands.

Table 3.2: Extinction coefficient (ε) of MMG in different organic solvents

Solvents	Band I	ε (M^{-1} cm^{-1})	Band II	ε (M^{-1} cm^{-1})	Band III	ε (M^{-1} cm^{-1})
Hexane	232	33290 ± 1190	286	42827.4 ± 1314	332, 368	7836.4 ± 246, 6013.4 ± 200
Ethyl acetate	-	-	286	36588 ± 1737	339, 370	7488.4 ± 525.4, 6058 ± 361
Methanol	233	29643 ± 1702	286	35318 ± 1939	366	7029 ± 276
Ethanol	233	27405.33 ± 3423	286	33110.67 ± 4188.5	369	6450 ± 837
Acetonitrile	234	29177 ± 358	286	34160.4 ± 564	339	7389 ± 111

3.3.2. MMG in ethanol – water binary solvent system

MMG is insoluble in water and ethanol was used as co-solvent for this study. To investigate the solubilization of MMG, 15 µM of the compound was added to different compositions of ethanol-water binary mixtures. Upon increasing the amounts of water from 0-99 % v/v in ethanol stock of MMG, a decrease in the absorbance of MMG was observed (**Fig 3.3 A**). For concentrations of water ≥ 60-70 % (v/v), a rapid decrease in the absorbance was noticed as a result of insolubility leading to precipitation (**Fig 3.3 B**). There was a mild red-shift (Δ=5 nm) in the spectrum observed at higher concentrations of water. Furthermore, a reverse titration was carried out, where ethanol concentration was increased from 1-100 % (v/v) in water, similar trend was observed. Increase in the absorbance was observed with increasing

concentration of ethanol, along blue-shift in the spectra (**Fig 3.3C & D**). Thus, the precipitation of MMG below 30-40 % v/v aq. ethanol was found to be reversible in nature. However, the extent of decrease of the absorbance below the transition point in **Fig 3.3B**, was not observed for 5-100 % (v/v) ethanol (**Fig 3.3D**). The reason could be due to longer duration of sample incubation in MMG insoluble solvent system, in case of 0-99 % v/v water in ethanol, which was not the case for 1-100 % v/v ethanol in water.

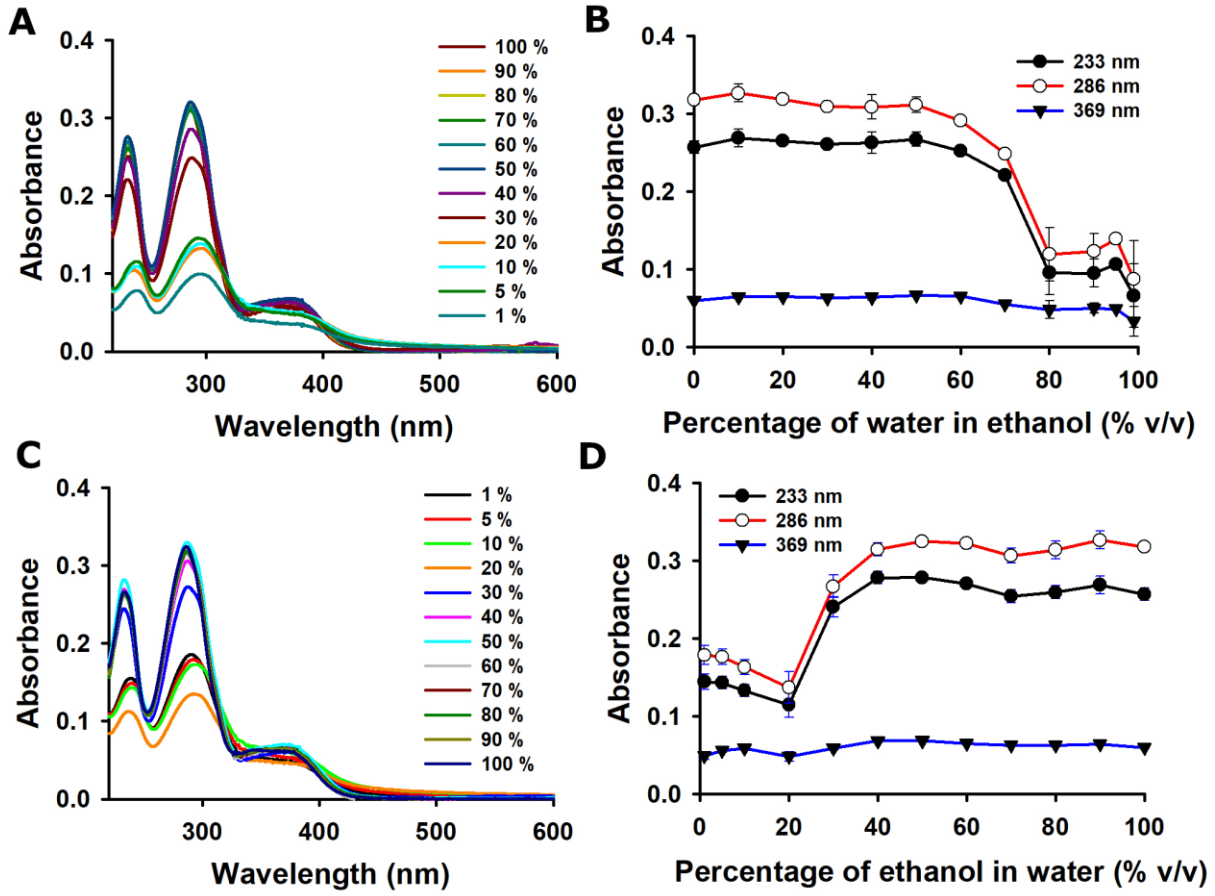

Figure 3.3: (A, C) – Absorption spectra of MMG (15 µM) in binary system of ethanol and water, from 100-1 % and 1-100 % aq. ethanol respectively. (B, D) – Absorbance of MMG (15 µM) at 233 nm, 286 nm, 369 nm for binary solvent system of 100-1 % and 1-100 % aq. ethanol respectively

When a binary solvent system is observed at a microscopic level, self-associated clusters of ethanol and water exists resulting in a bi-continuous phase separation. Thus, a binary system provides a micro-heterogenous environment leading to deviation from ideal behaviour at low and intermediate concentrations of ethanol in water (Bhatia et al., 2016). At high concentrations of ethanol, the local environment around MMG was still ethanol, resulting in high absorption. However, as the amount of ethanol was decreased below 40 % (v/v), the hydrogen bonded water clusters increased resulting in precipitation of MMG

leading to the reduction of absorbance. Further higher concentrations of water led to red-shift in the spectra. Similar behaviour was observed for other flavonoids like quercetin-3-O-rhamnoside, which also displayed reduced absorbance and red-shifted spectra with increase in water concentration (Liu et al., 2009). Likewise, a dip in absorbance was observed for furanoflavonoid karanjin, around 50 % and 90 % v/v methanol-water binary mixtures owing to karanjin aggregation (Singh et al., 2021). For curcumin, conformational transition from enol to keto form took place at concentrations ≤ 50-40% (v/v) of ethanol in water, due to intermolecular hydrogen bonding with the solvent (Bhatia et al., 2016; Mondal et al., 2016). Thus, the hydrogen bonding of ethanol is dominated by stronger hydrogen bonding of water at concentrations above 50-60 % (v/v) water in such ethanol-water binary mixtures, causing spectral changes of MMG.

3.3.3. Absorption behavior of MMG in micro-heterogenous systems

Absorption spectra of MMG in surfactant micelle – SDS (20 mM), CTAB (5 mM) and T20 (0.5 mM) revealed similar spectra as that in the organic solvents, with the λ_{max} 234 nm, 287 nm and 374 nm (**Fig 3.4**). Thus based on the absorption spectra obtained, it can be concluded that the solubility of MMG was significantly enhanced in surfactant micelle as compared to water (1 % v/v ethanol). The micelles provided the non-polar pockets in the aqueous medium, appropriate for MMG solubilization.

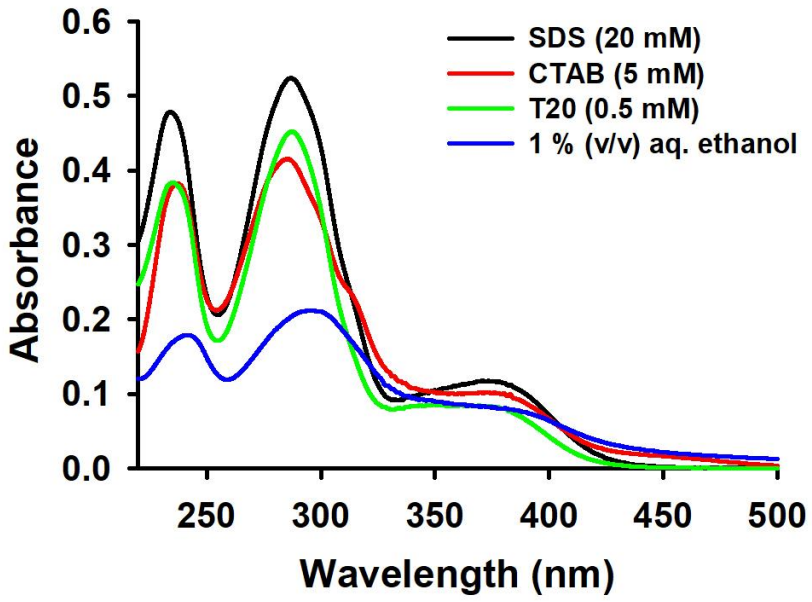

Figure 3.4: Absorption spectra of MMG in surfactant micelles

Amongst the surfactants, MMG in SDS and T20 displayed high extinction coefficient (**Table 3.3**). Hydrophobic and/or electrostatic interactions are involved in solubilization of molecules in micelles (Saraf et al., 2018). Since SDS is negatively charged and T20 is neutral, strong hydrophobic interaction would be the driving force for interaction with the micelles. The increased absorption of MMG could be due to internalization into the micelles, either into the core or palisade layer (Chatterjee and Suresh Kumar, 2016), since MMG is non-polar. While in case of CTAB, MMG yielded broader peaks resulting in lower absorption. It has been previously reported that CTAB provides a relatively alkaline environment which could have led to deprotonation of MMG by disrupting the acid-base balance (Liu et al., 2001). Thus there could exist two forms of MMG in the presence of CTAB, ionized and nonionized form. The ionic MMG could have a red-shifted spectra due to which, the overlapping of ionic and nonionic forms of MMG resulted in broadening of the peaks and decrease in absorbance.

Table 3.3: Extinction coefficient (Ɛ) of MMG in surfactant micelles

Solvents	**Band I** ε_{234} **(M^{-1} cm^{-1})**	**Band II** ε_{287} **(M^{-1} cm^{-1})**	**Band III** ε_{374} **(M^{-1} cm^{-1})**
SDS (20 mM)	23290.3 ± 251	25498 ± 284.5	5708.5 ± 67
CTAB (5 mM)	18268 ± 246	19747 ± 284.5	4924 ± 34
Tween 20 (0.5 mM)	20904 ± 712	24566 ± 817	4642 ± 147

3.3.4. Optimization of co-solvent concentration for surfactant systems

MMG was not soluble in surfactant solutions when dissolved directly in their solid form and thus co-solvent was required for solubilization. Ethanol is a commonly used co-solvent for various biological systems, which was chosen for this study as well. Furthermore, the amount of ethanol required to sufficiently solubilize MMG needed to be optimized, for which 1 to 5 % (v/v) ethanol was investigated as co-solvent in the mentioned surfactant micelle solutions. **Fig 3.5** revealed that the absorbance of MMG at 287 nm in 1% v/v ethanol was similar to that in 5% v/v ethanol in all the surfactant micelle solutions. Moreover, the acceptable limit of ethanol co-solvent for biological systems is ≤ 2.5 % (v/v) (Hamzeloo-Moghadam et al., 2014; Nguyen et al., 2020). Since the difference in the absorbance with increasing concentration of

ethanol was not significant, 1% (v/v) ethanol was optimized for solubilizing MMG in surfactant systems. This concentration was used for all the upcoming related experiments.

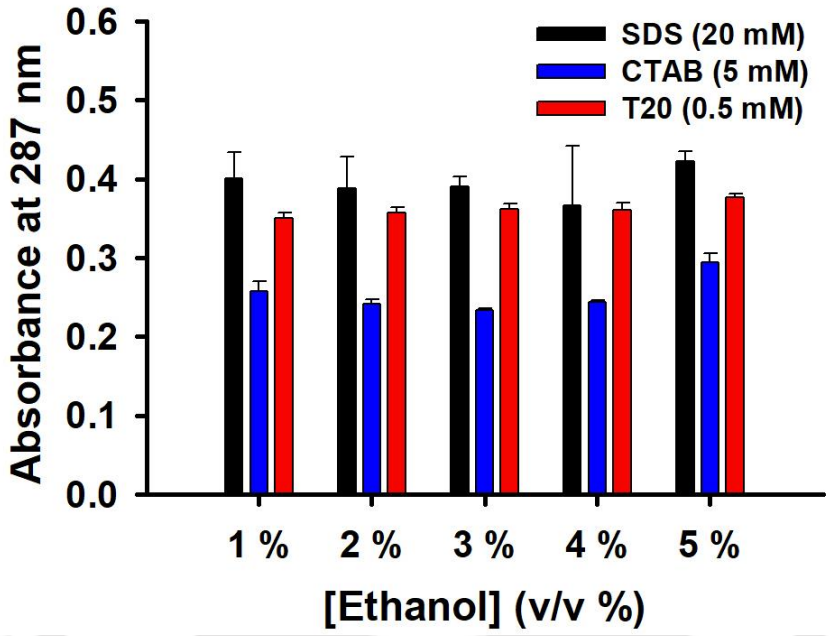

Figure 3.5: Absorbance of MMG at 287 nm in SDS (20 mM), CTAB (5 mM) and T20 (0.5 mM) in 1-5 % (v/v) ethanol co-solvent

3.3.5. Comparing the relative environment of MMG in surfactant micelles

Fig 3.6 A, B, C depicts the Molar extinction coefficient (Ɛ) calculation of MMG for Band I, II and III in selective neat organic solvents (hexane and ethanol), the surfactant micelles and ethanol-water solvent mixture. **Fig 3.6 D** summarizes the Ɛ values of MMG in these solvent systems.

Compared to organic solvents like ethanol (protic) and hexane (aprotic), the Ɛ was marginally lower in surfactants. On the other hand, Ɛ in 40% (v/v) aq. ethanol was similar to that of surfactant micelles. Thus, the environment of MMG in surfactant micelles was neither fully hydrophobic nor hydrophilic, but partially semi-polar.

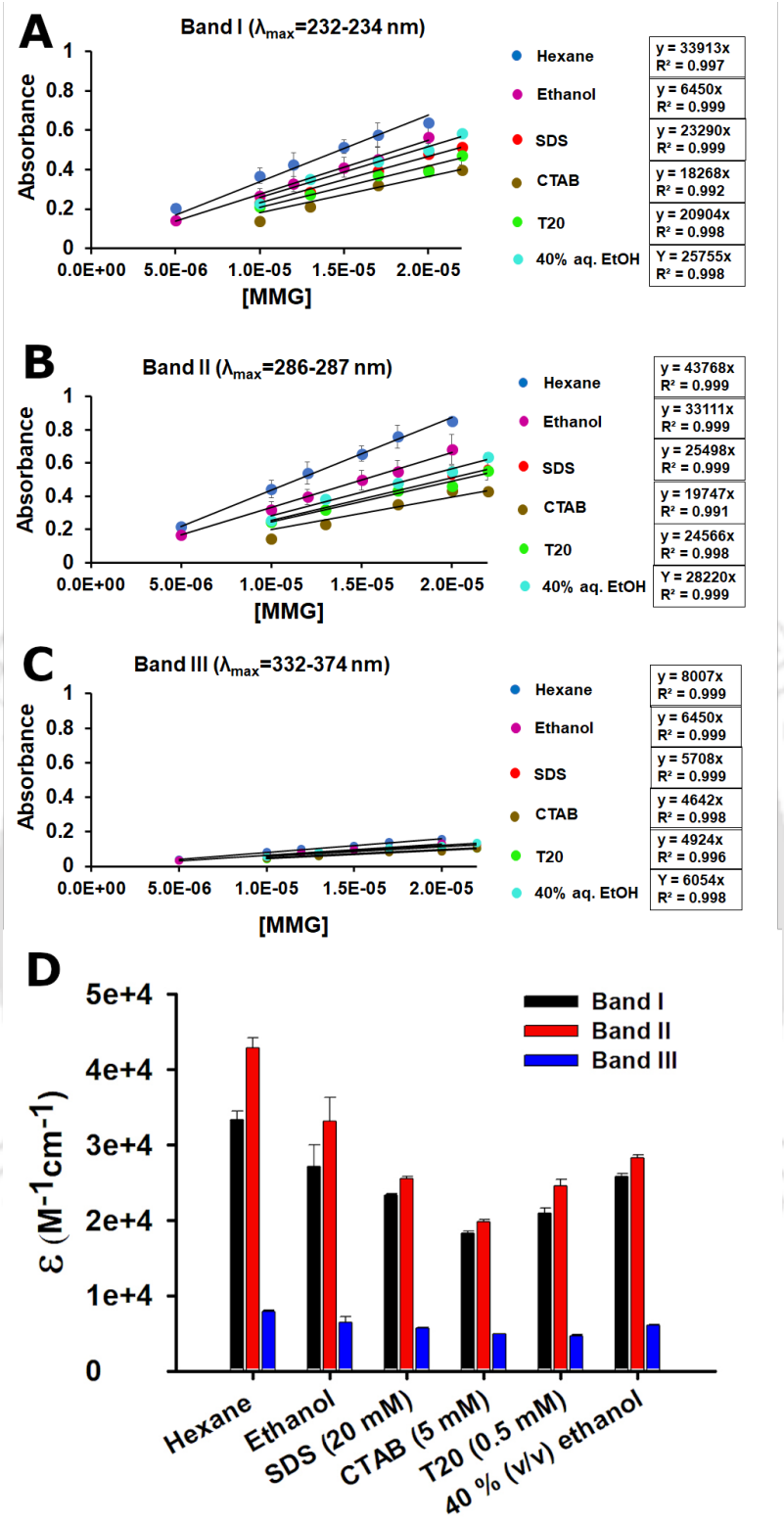

Figure 3.6: Molar Extinction coefficient (Ɛ) calculation of MMG in hexane, ethanol, SDS (20 mM), CTAB (5 mM), T20 (0.5 mM) and 40% v/v aq. Ethanol (EtOH) for (A) Band I (232-234 nm) (B) Band II (286-287 nm) and (C) Band III (332-374 nm). (D) Comparison of Ɛ of MMG in organic solvents, binary solvent and surfactant micelles

Fig 3.7 depicts the possible binding sites of MMG in surfactant micelles. In all the three surfactants, scenarios I, II and III depicted is likely to exist. In case of SDS and T20, MMG would be more internalized into the hydrophobic core of the micelle and thus the scenario III is likely to be more prevalent. But in CTAB, it can be speculated that MMG binds to the palisade layer of micelles where the hydrophobic part of the compound is exposed to micelle core and the ionic part of the compound to charged head group of the surfactant (Saraf et al., 2018). Thus the scenario II is likely to predominate.

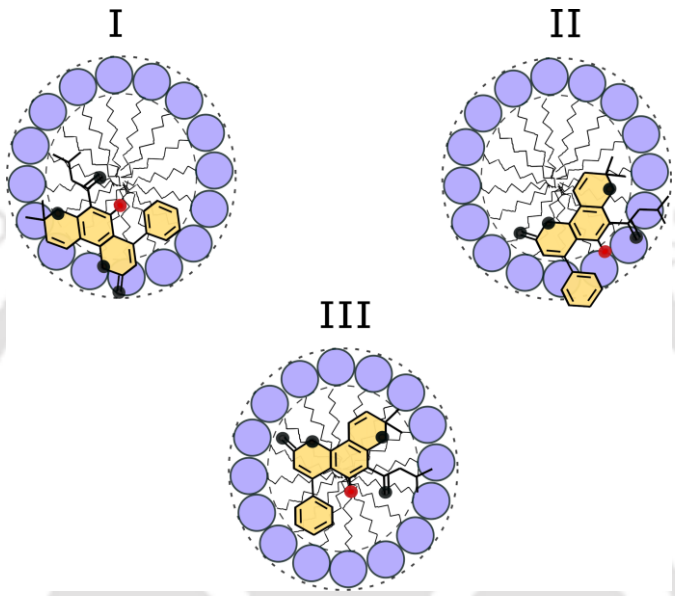

Figure 3.7: Possible scenarios of MMG (Aromatic rings – yellow-coloured, oxygen atoms-black circles and a hydroxyl group – red circle) interacting with SDS, CTAB and T20 micelles (polar head groups - Blue circles, nonpolar tails - zig-zag lines, stern layer – dashed lines).

3.3.6. Absorption spectra of MMG at different surfactant concentrations

A water-insoluble compound solubilises in surfactants only beyond its cmc and thus changes in the relative environment influences the spectroscopic properties of the compound (Mabrouk et al., 2021). The absorption spectrum of MMG (15 µM) at varying concentrations of the surfactants i.e., pre-cmc, cmc and post-cmc was investigated. The results displayed an overall increase in absorbance of MMG at its λ_{max} 233, 287, 374 nm, with increase in concentrations for all the surfactants, prominently in SDS and CTAB. This was due to increased solubilization of MMG with micelle formation driven by hydrophobic and electrostatic interactions (Saraf et al., 2018). However, around the cmc of SDS (7-11 mM), there was precipitation of MMG resulting in drastic decrease of absorbance at those concentrations (**Fig 3.8A**). These observations could be due to electrostatic repulsions (Liu and Guo, 2006b). Also, the structure of the micelle is flaccid and flexible at the cmc due to

and Guo, 2006b). Also, the structure of the micelle is flaccid and flexible at the cmc due to loose spherical shape of the micelle, making them highly permeable to bulk solvent (Aygün et al., 2020; Chatterjee and Suresh Kumar, 2016). This might make them susceptible to physical disturbances like mixing or vortexing of samples.

Similarly, a dip in the absorbance at 0.8-1 mM CTAB cmc concentrations was observed (**Fig 3.8B**). Unlike SDS, the decrease in the absorbance in CTAB was not highly prominent and was not due to precipitation. Thus in CTAB, the interaction between MMG and positively charged head group could have contributed to the stabilizing effect at premicellar and micellar concentrations of the surfactant. The absorbance dip could be due to local solvent change for MMG with higher water content inside the micelles at cmc, resulting in reduction of Ɛ (Aygün et al., 2020; Liu and Guo, 2006a).

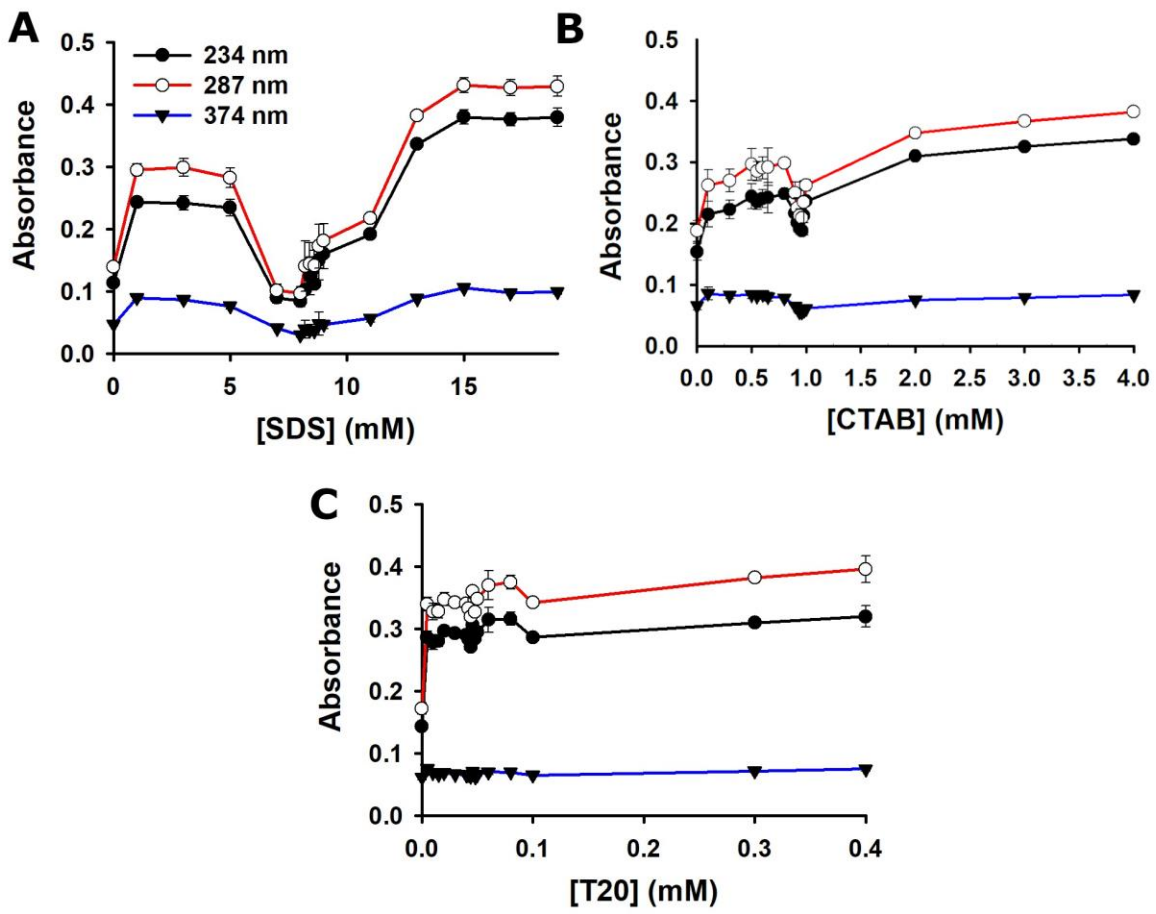

Figure 3.8: (A) Absorbance of MMG (15 µM) at 234 nm, 287 nm and 374 nm in different concentrations of (A) SDS, (B) CTAB, (C) T20.

In case of T20, there was mild precipitation in the samples below and at cmc, resulting in

irregular absorbance. Unlike SDS and CTAB, no decrease in absorbance was observed (**Fig 3.8C**). Since there is no electrostatic interactions involving in T20, hydrophobic force was the major driving factor for interactions of MMG with T20 micelles. Whereas at pre-cmc concentrations, hydrophobic interactions were not the dominant forces. Thus the binding of MMG to T20 molecules at those concentrations could be through weak intermolecular hydrogen bonding with OH groups (Liu and Guo, 2006a).

At post-cmc concentrations of surfactants, there was dramatic rise in the absorbance was observed for SDS at all the wavelengths, while CTAB and T20 exhibited modest increase. MMG is neutral and thus gets fully internalized into the SDS micelles core due to hydrophobic forces resulting in increase in absorbance, which was lower for T20. While in case of CTAB, MMG gets distributed in the micelle core as well as palisade layer leading to lower absorbance than SDS.

Since charges of the surfactant plays a role in interaction with MMG and to further explain the dip in the absorbance at cmc, the effect of high ionic strength at different surfactant concentrations was investigated. Upon addition of 200 mM NaCl, the dip in absorbance around cmc values was absent in both SDS and CTAB accompanied by slight increase in the absorbance of MMG (**Fig 3.9A & B**). Moreover, the absorbance of MMG was stabilized at concentrations greater than 3 mM SDS and 0.6 mM CTAB.

Salt ions interacts with the charged head of the surfactant, which leads to weakening of electrostatic repulsion between the adjacent surfactant molecules in micelle and results in decrease of cmc. Thus the micelles are more compact and forms ellipsoidal or lamellar shaped micelle. Such compact structures have reduced inflow of bulk solvent into the micelle, thus providing relatively more hydrophobic environment (Aygün et al., 2020; Chatterjee and Suresh Kumar, 2016). This could have contributed to the increase in MMG absorption. On the contrary, T20 displayed high precipitation at concentrations below and around the cmc values (**Fig 3.9C**). This could be attributed to disruption in the interaction between the T20 molecules in the presence of salt, as it does not possess any charge.

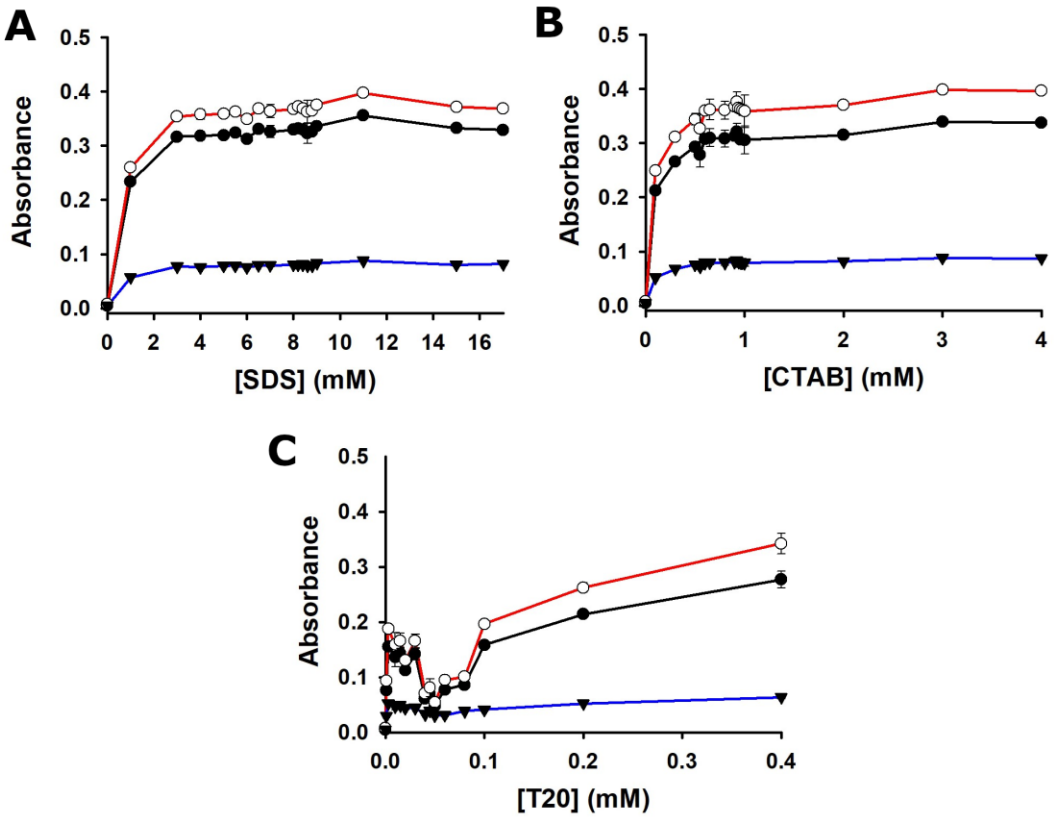

Figure 3.9: (A) Absorbance of MMG (15 µM) at 234 nm, 287 nm and 374 nm in different concentrations of (A) SDS, (B) CTAB, (C) T20 in the presence of 200 mM NaCl.

3.3.7. Stability of MMG in the surfactant micelles

The stability of MMG in the surfactants at room temperature (26-32 ºC) was investigated in the surfactant micelles with time. It was found that MMG was stable in SDS and CTAB over 25 hrs, along with a mild increase in absorbance over time suggesting improved binding. On the other hand, the stability of MMG reduced gradually with time in T20 micelles (**Fig 3.10**). This indicated that strong hydrophobic and electrostatic interactions were essential for stable binding of MMG in micelles. The SDS provided hydrophobic environment inside the micelles which results in stable binding over time, whereas CTAB involves relatively more stable interaction with MMG due to electrostatic attraction between MMG and CTAB, along with hydrophobic interacting forces (Dutta et al., 2013; Saraf et al., 2018). Although the mode of interaction of MMG with SDS and T20 micelles were similar, yet the stability varied. Thus, the hydrophobic interactions of T20 micelle was weak and insufficient to hold MMG intact over time. Another possible reason could be autooxidation of T20 in solution over time (Donbrow et al., 1978), leading to instability of MMG.

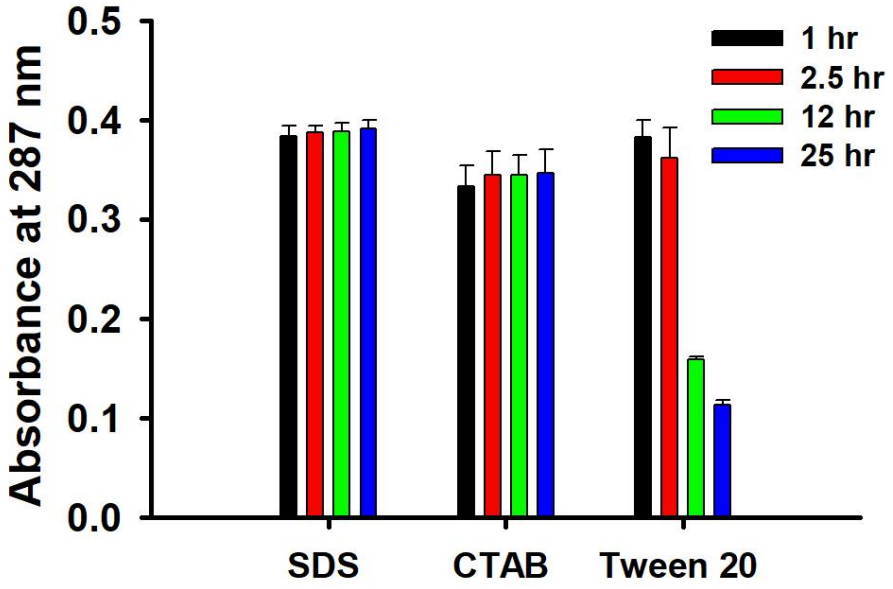

Figure 3.10: Absorbance of MMG (15 μM) at 287 nm in aq. SDS (20 mM), CTAB (5 mM) and T20 (0.5 mM) over a period of 25 hrs at room temperature (26-32 ºC)

3.3.8. Investigation of fluorescence property of MMG

Fluorescence emission properties of MMG was investigated in various solvent systems under study at λ_{ex} 286 nm and 369 nm. The emission from λ_{ex} = 286 nm was inconsistent, sometimes non-existent, low and overlapping with Raman peak resulting in fluctuations (data not shown). Thus 286 nm excitation was not investigated further. However at λ_{ex} = 369 nm, MMG exhibited fluorescence emission, but was quite low with a large Stokes shift in the range of 10,151-10,787 cm^{-1} (**Fig 3.11A**)

Quantum yield (Q_F) is a commonly used method to quantify fluorescence emission of a compound. The Q_F of MMG was determined at λ_{ex} = 369 nm in various solvent systems using Equation 3.2. **Table 3.4** summarizes the Q_F obtained for the organic solvents, 40 % v/v aq. ethanol and surfactant micelle. MMG in SDS micelles displayed relatively higher Q_F than other solvents. This could be due to restricted motion of MMG in the micelles resulting in lower non-radiative decay. Since MMG is non-polar, hexane yielded second highest Q_F, although its absorption properties in hexane was higher than SDS. However, the Q_F was still quite low compared to the standards (**Fig 3.11B**).

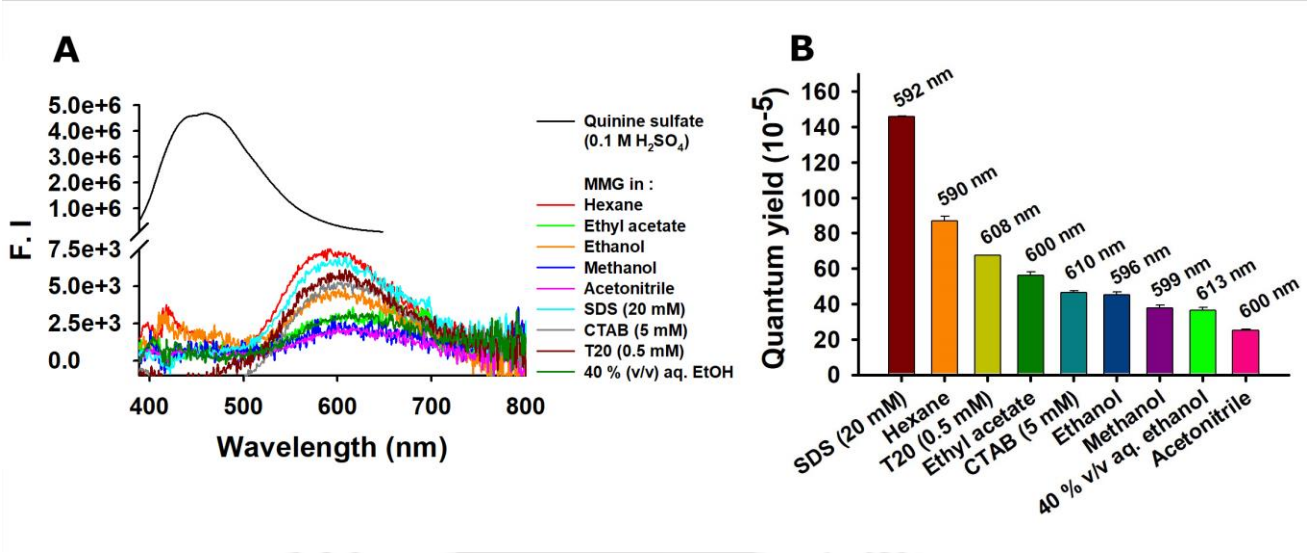

Figure 3.11: (A) Fluorescence emission spectra of MMG (1 µM; OD_{369} = 0.004-0.008) in different solvent systems and Quinine sulfate (OD_{369} = 0.008) with λ_{ex}= 369 nm. Long pass filter (WG-490) was used in the range of 700-800 nm region to remove second diffraction peak. (B) Fluorescence quantum yield of MMG in different solvent systems. [Emission peaks are mentioned above the histogram bar of each solvent system]

Table 3.4: Fluorescence quantum yield of MMG in various solvent systems

Solvents	**λ_{ex} = 369 nm**		
	Q ($x10^{-5}$)	**λ_{em} (nm)**	**Stokes shift (cm^{-1})**
Hexane	87.1 ± 2.55	590	10,151
Ethyl acetate	56.2 ± 1.8	600	10,434
Methanol	37.9 ± 1.3	599	10,406
Ethanol	45.3 ± 1.4	596	10,322
Acetonitrile	25 ± 0.81	600	10,434
40 % (v/v) aq. ethanol	36.3 ± 1.82	613	10,787
SDS (20 mM)	146 ± 0.12	592	10,208
CTAB (5 mM)	46.6 ± 0.86	610	10,707
T20 (0.5 mM)	67.2 ± 0.19	608	10,653

In heteroatomic polyphenols with 5-OH group such as MMG, π-π* and n-π* states are closer resulting in near degeneracy of these energy states. Such molecules undergo rapid internal conversion resulting in low fluorescence emission and larger Stokes shifts (Liu et al., 2009). It has been reported that neoflavonoids have weak conjugation between B and C rings

(Marković and Tošović, 2015). This could result in non-planarity of B-ring with respect to the molecule causing rapid movement of the ring in the solvent, resulting in low fluorescence emission.

3.4. Conclusions

Spectroscopic properties of MMG were investigated in various solvent systems. The absorption spectra of MMG revealed three major absorption bands, with the high absorption peaks at 234 nm and 286 nm and a shoulder peak at 332-369 nm. MMG displayed insensitivity to organic solvents of different polarities. It was insoluble in water and required concentrations ≤ 40 % (v/v) of ethanol in water binary mixtures for solubilization. The solubility of MMG was enhanced in aqueous medium in the presence of surfactant micelles (SDS, CTAB and T20), which were driven by hydrophobic and electrostatic interactions. MMG displayed variations in the absorption spectra at pre-cmc and cmc of the surfactants. The stability of interactions at cmc's of ionic surfactants improved in the presence of salt additives. However, the stability of MMG with time was achieved in case of SDS and CTAB, not T20. The fluorescence properties of MMG was explored in various solvent systems, which displayed poor fluorescence yield. Therefore, the surfactant micelles were successful in encapsulating MMG, solubilizing and stabilizing it in aqueous medium, which could be used to develop improved drug delivery strategies.

Chapter 4

Investigating the Spectroscopic properties of Mammeigin in Hen Egg-White Lysozyme aggregates

4.1. Introduction

Lysozyme is an exceptionally abundant protein found in Fowl egg whites which functions as anti-bacterial agent and also source of nutrition for early embryogenesis (Sears, 2019). They are natural emulsifiers, utilized for applications in dairy industry (Kralova and Sjöblom, 2009). Hen Egg-White Lysozyme (HEWL) is a water-soluble protein, whose aggregation under various conditions has been extensively studied. Aggregation and fibrillation of HEWL can be made to occur in acidic pH at elevated temperature, alkaline pH at room temperature, concentrated solution of aqueous ethanol, molecules like SDS, guanidine hydrochloride (Swaminathan et al., 2011).

Protein aggregation is initiated by partial unfolding of the native structure, facilitating intermolecular interactions involving hydrophobic and electrostatic forces which are required to initiate polymerization. This leads to formation of spherical oligomers, which further associate to form amorphous aggregates and pre-fibrillar intermediates called protofibrils. They then mature to form structured assemblies called fibrils (**Fig 4.1**).

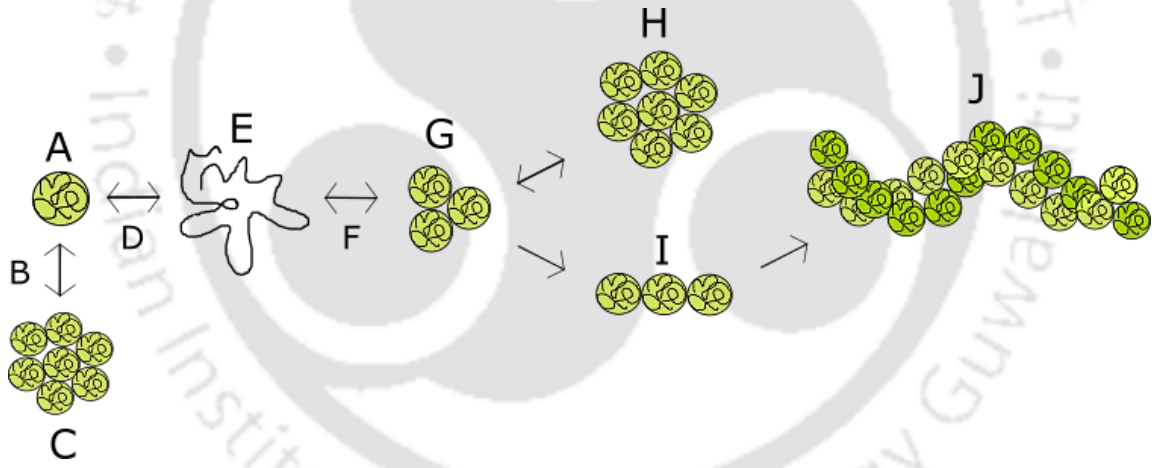

Figure 4.1: Process of protein aggregation and fibrillation. A – native protein; B – off-pathway; C – amorphous aggregates; D – upon stress conditions like pH, temperature, solvent additives; E – partially unfolded protein; F – on-pathway; G – oligomer; H – amorphous aggregates; I – protofibril; J – mature fibril

The aggregation can occur via two different pathways or their hybrids, namely – Nucleation-Dependant Polymerization (NDP) and Isodesmic Pathway. NDP pathway involves formation of a concentration-dependent nucleus intermediate which acts as a seed for aggregation. While Isodesmic polymerization follows a linear trend where aggregation can begin from any of the monomeric subunits (Chiti and Dobson, 2006; Frieden, 2007; Kumar and Udgaonkar, 2010; Soto and Pritzkow, 2018).

There have been numerous reports on the interaction of plant polyphenols with HEWL aggregates, where the phenolic compounds have shown disassembly, inhibition or reduction of aggregates and fibrils. The mechanism involves blocking hydrophobic interactions between prefibrillar aggregates, disrupting the π-π stacking interactions between protein units, interference with aggregation processes, reducing oxidative stress and hydrogen bonding with the protein backbone (Furkan et al., 2019; Shariatizi et al., 2015; Stefani and Rigacci, 2013).

Preliminary studies of MMG interaction with HEWL aggregates at different pH conditions were carried out, which revealed no significant anti-aggregation or anti-fibrillation activities. Thus, the focus of the study was diverted to investigating the interactions of MMG with the HEWL aggregates and fibrils for possible application as protein drug carrier, similar to surfactants. Thus, the current chapter focuses on studying interactions of MMG with HEWL aggregates at pH 2, pH 5 and pH 9, thereby attempting to recreate surfactant micelle like environment.

4.2. Materials and Methods

4.2.1. Preparation of HEWL aggregates at pH 2 and pH 5

HEWL (Sigma Aldrich, India) stock was prepared in deionized water and the concentration was determined using ε_{280} = 37,970 $M^{-1}cm^{-1}$. HEWL (1.36 mM) was prepared in pH 2 (0.01 M Glycine) buffer with 0.02 % (w/v) sodium azide (Sigma Aldrich, India) and incubated for 5 days at 65 ºC. For every 24 hrs upto 96 hrs, the HEWL sample was diluted 10 fold in the same buffer and mixed with MMG (5 µM, 15 µM, 30 µM and 50 µM) with 1% (v/v) ethanol. Corresponding controls were taken in the buffer. The samples were vortexed, incubated for 2 hrs and centrifuged (10,500 rpm for 3 minutes) before taking readings. Absorption spectra were recorded from 300-600 nm and absorbance at 374 nm was noted. Absorption spectra in the range 220-300 nm were avoided due to overlapping of HEWL and MMG high absorbing bands. Extinction coefficient was determined for MMG-HEWL aggregate complex at wavelengths 300nm, 317 nm, 374 nm and 442 nm using Beer-Lambert law (equation 3.1). The contribution of HEWL aggregates was subtracted from MMG-HEWL aggregate samples.

HEWL (100 µM) was prepared in pH 5 (0.1 M Citrate) buffer with 0.02 % (w/v) sodium azide and incubated for 5 days at 65 ºC. For every 24 hrs upto 96 hrs, HEWL sample

was aliquoted and added with MMG (5 µM, 15 µM, 30 µM and 50 µM) with 1% (v/v) ethanol. Corresponding controls were taken in the buffer. The samples were vortexed, incubated for 2 hrs and centrifuged (10, 500 rpm for 3 minutes) before taking readings. Absorption spectra were recorded from 300-600 nm and absorbance at 374 nm was noted. (With modifications from Ansari et al., 2018)

As a monomer control, HEWL in pH 7 (50 mM phosphate) buffer was added with MMG (5 µM, 15 µM, 30 µM and 50 µM) with 1% (v/v) ethanol at room temperature (25-30 ºC) and absorption spectra were collected in the similar manner.

4.2.2. Thioflavin T fluorescence assay

Thioflavin T (ThT) stock was prepared in deionized water and the concentration was determined using ε_{416} = 26,620 $M^{-1}cm^{-1}$. Aliquots of appropriate volume from the ThT stock were stored in microfuge tubes at -20ºC until further use. These aliquots were only prepared for single time use.

HEWL samples were diluted in pH 7 buffer (50 mM phosphate, 100 mM NaCl) and added with ThT such that ThT : protein ratio was 20 µM:10 µM. The sample was mixed well by flushing with micropipette and fluorescence emission was recorded immediately. The λ_{ex} was 450 nm (Ex. slit = 1 nm) and fluorescence emission was recorded in HORIBA Fluorimax-4 spectrofluorimeter and integrated in the 470-550 nm range (Em. slit = 5 nm). (With modifications from Ravi et al., 2014a).

4.2.3. Time-dependent interaction of MMG with HEWL aggregates

At pH 2, HEWL (1.36 mM) was incubated with MMG (150 µM) for 6 days at 65 ºC. In the time intervals of 2 hrs, 72 hrs and 144 hrs, the samples were 10 fold diluted in the pH 2 buffer. The sample was centrifuged (10,500 rpm for 3 minutes) before recording the absorption spectra and absorbance at 374 nm. ThT fluorescence was also recorded.

While at pH 5, HEWL (100 µM) was incubated with MMG (15 µM) for 6 days at 65 ºC. In the time intervals of 2 hrs, 72 hrs and 144 hrs, The sample was aliquoted and centrifuged (10,500 rpm for 3 minutes). The absorption spectra, absorbance at 374 nm and ThT fluorescence were recorded.

4.2.4. Preparation of MMG-polycationic HEWL aggregate complex in pH 9

HEWL (120 µM) was incubated at pH 12.2 (0.02 N NaOH) with 0.02 % (w/v) sodium azide for 5 days at room temperature (25-32 ºC) (Ravi et al., 2014b). The HEWL from pH 12.2 was 10 fold diluted into pH 9 (0.1 M Tris) buffer and mixed with MMG (50 µM). Subsequently, different concentrations of MMG (5 µM, 15 µM, 30 µM and 50 µM) were added to polycationic HEWL aggregates (pHEWL), corresponding MMG control in pH 9 buffer and HEWL in pH 12.2. The samples were centrifuged (10,500 rpm for 3 minutes) prior to taking readings. Absorption spectra were recorded from 300-600 nm and absorbance at 300 nm, 317 nm, 374 nm, 442 nm was noted. The Ɛ was estimated using equation 3.1. While determining Ɛ for MMG-pHEWL complex, the contribution of pHEWL was subtracted.

4.2.5. MMG in surfactant micelles at pH 9

Surfactant micelles – SDS (20 mM), CTAB (5 mM) and T20 (0.5 mM) were prepared in pH 9 buffer (0.1 M carbonate-bicarbonate). From the stock, different concentrations of surfactants were prepared in pH 9 buffer and added with MMG (15 µM). The samples were vortexed and incubated over 1 hr prior to collecting absorption spectra.

4.3. Results and discussion

4.3.1. Investigating the MMG interaction at different stages of HEWL aggregation at pH 2 and pH 5

MMG of various concentrations were added to different stages of HEWL aggregation and fibrillation and their interactions were investigated. MMG was found to be insoluble in pH 2 and pH 5. But when added to HEWL aggregates at pH 2, there was increase in absorption observed in a concentration-dependant manner of MMG (**Fig 4.2 A**). However, there was decrease in the MMG-HEWL absorption observed at time intervals ≥ 2 hrs especially at high MMG concentrations, yet higher than the HEWL control (**Fig 4.2 B-E**). On the contrary, MMG added to HEWL aggregates at pH 5 displayed same absorption spectra as HEWL aggregate control at all the time intervals, with no increase or decrease in the absorption (**Fig 4.2 F-J**).

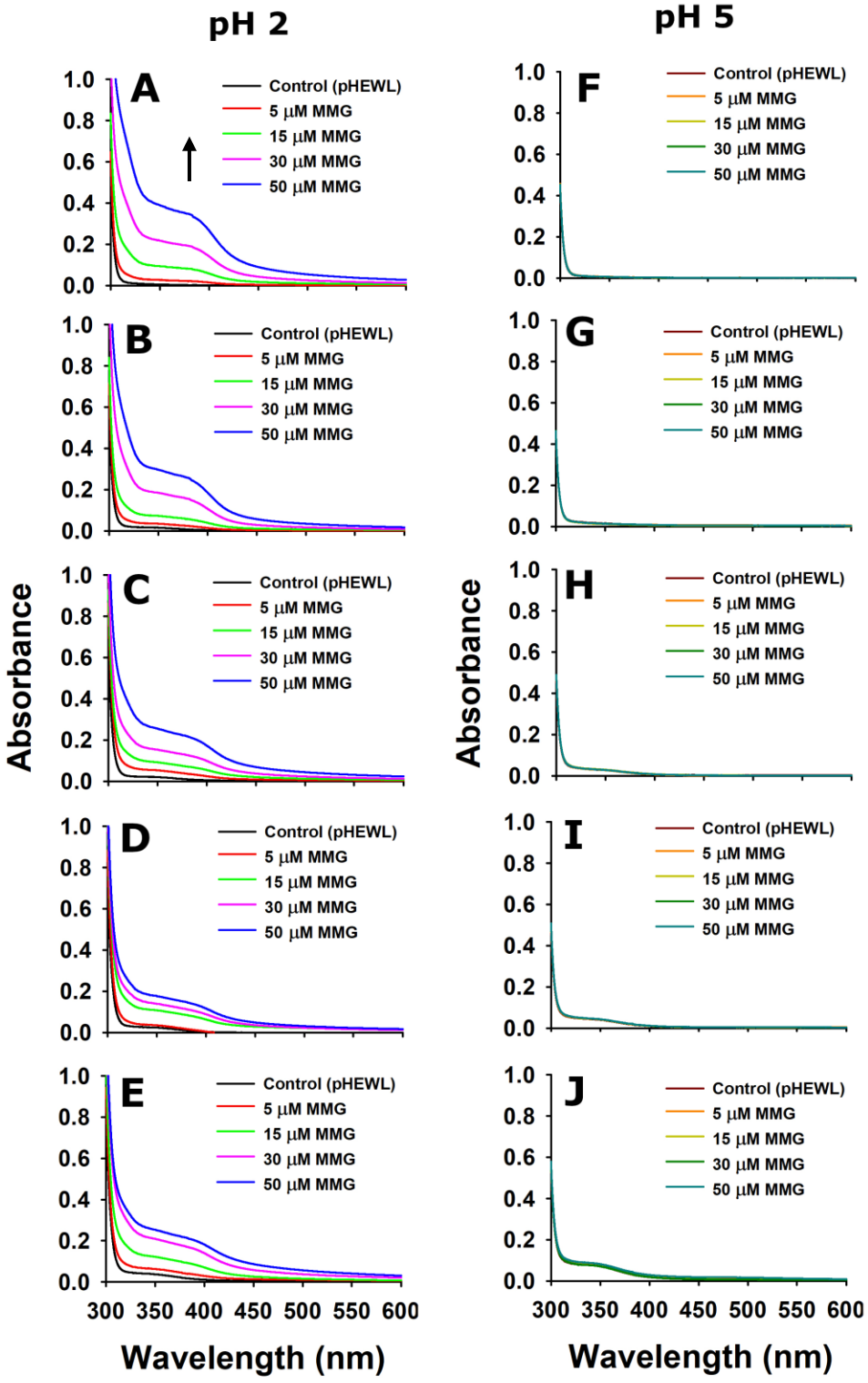

Figure 4.2: Absorption spectra of MMG (5 µM, 15 µM, 30 µM, 50 µM) in HEWL aggregates (136 µM) at pH 2 at different time intervals - (A) 2 hrs, (B) 24 hrs, (C) 48 hrs, (D) 72 hrs and (E) 96 hrs. Absorption spectra of MMG (5 µM, 15 µM, 30 µM, 50 µM) in HEWL aggregates (100 µM) at pH 5 at different time intervals- (F) 2 hrs, (G) 24 hrs, (H) 48 hrs, (I) 72 hrs and (J) 96 hrs. Arrow mark indicates increase in absorption.

To ensure the interaction only occurred with HEWL aggregates and not the monomer, HEWL at pH 7 was added with the given concentrations of MMG. Upon addition of MMG, there was high precipitation of the samples observed due to MMG insolubility. After removal of the precipitates, the absorption spectra revealed no absorption in the 300-600 nm region from MMG-HEWL interactions, without affecting the HEWL monomers (**Fig 4.3**). This confirms that the interactions only occurred with aggregates not with the monomers.

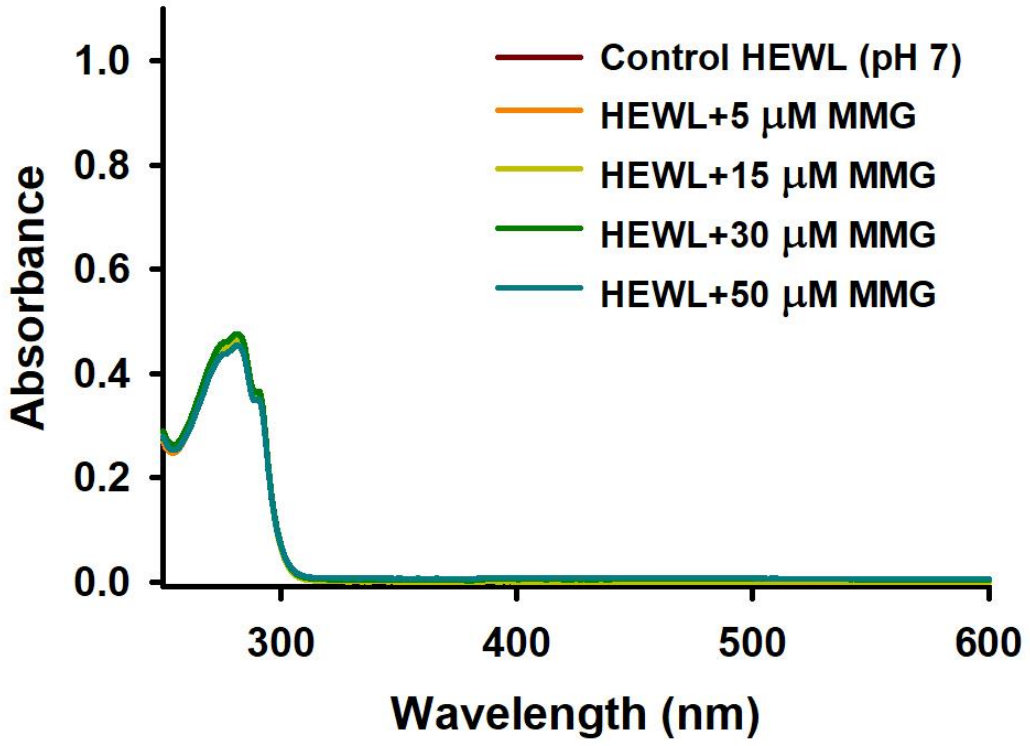

Figure 4.3: Absorption spectra of HEWL (12 µM) at pH 7 added with different concentrations of MMG (5, 15, 30, 50 µM). The samples were centrifuged due to precipitation upon addition of MMG to HEWL at pH 7.

To further get a clear understanding, the absorbance at 374 nm was plotted for different concentrations of MMG in HEWL aggregates at pH 2 and pH 5. At the beginning of the aggregate formation (time = 2 hrs), there was a linear increase in the absorption of MMG-HEWL aggregate complex with increase in MMG concentration (**Fig 4.4 A**). But as the aggregates began to mature and fibril formation occurs, the absorbance started to reduce compared to the initial aggregate stage, prominently observed at higher MMG concentrations. Compared to pH 2, MMG in HEWL aggregates at pH 5 clearly did not display any kind of interactions (**Fig 4.4 B**).

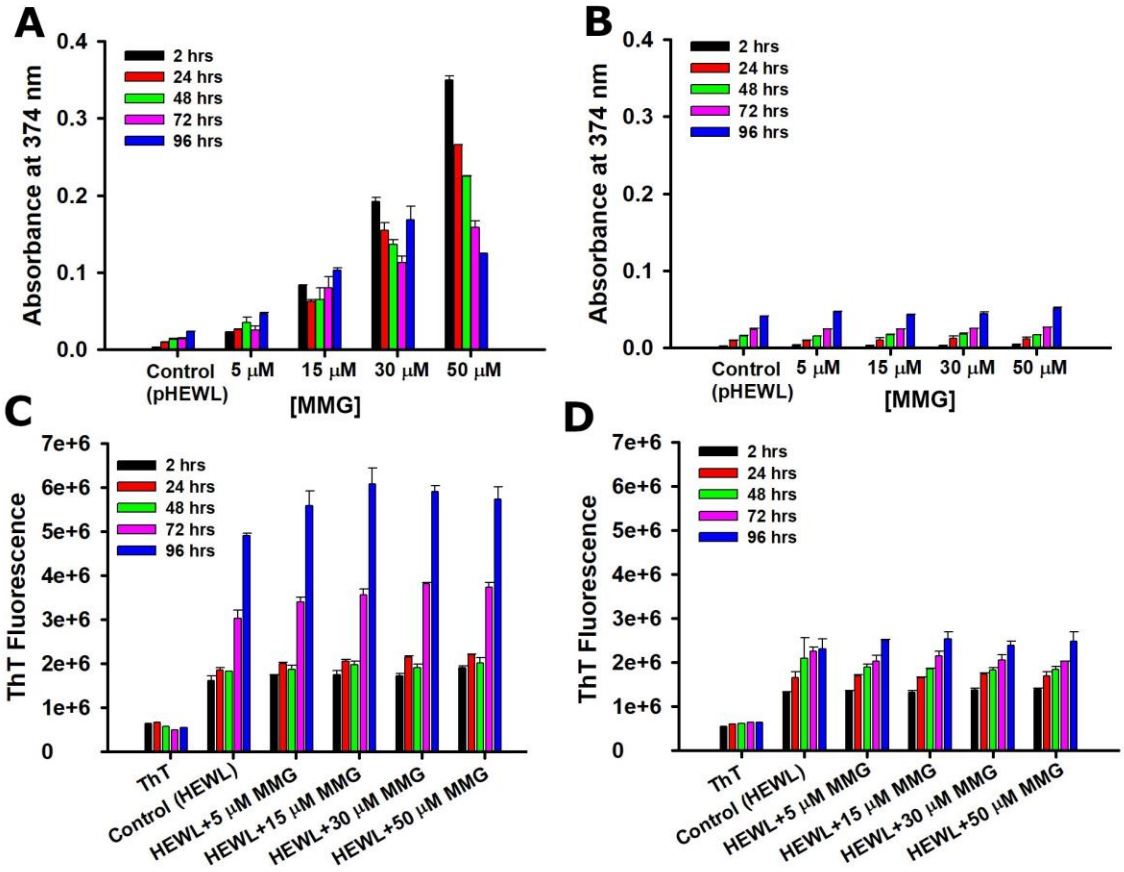

Figure 4.4: Absorbance of MMG (5 μM, 15 μM, 30 μM, 50 μM) added to (A) HEWL aggregates (136 μM) in pH 2 and (B) HEWL aggregates (100 μM) in pH 5, at 374 nm. ThT assay for MMG (5 μM, 15 μM, 30 μM, 50 μM) in (C) HEWL aggregates (136 μM) in pH 2 and (D) HEWL aggregates (100 μM) in pH 5.

The results can be explained as follows: when the HEWL aggregates just begins to form, it undergoes partial unfolding. The MMG gets the chance to interact with the aggregates. But as the aggregates start to mature and eventually form fibrils, MMG experiences reduced accessibility into the aggregates. Another possible explanation could be dissociation of HEWL aggregates by MMG at higher concentrations, which is often reported for such polyphenolic compounds. To validate these theories, Thioflavin T (ThT) fluorescence assay was carried out. The dissociation of aggregates would result in reduced hydrophobic regions, which causes decrease in ThT fluorescence. **Fig 4.4 C and D** revealed increasing ThT fluorescence with time suggesting that there was no HEWL aggregates dissociation at the given concentrations of MMG in both pH 2 and pH 5. Thus, the decrease in absorbance at higher MMG concentrations was attributed to reduced access for MMG into HEWL aggregates at later stages, leading to low stability of MMG at pH 2.

Although it was the same protein, the aggregates formed at different pH exhibited varied interactions with MMG. Ansari et al., (2018) had reported the differences in the aggregate formation of HEWL at pH 2 and pH 5. HEWL have reduced aggregation and/or forms of smaller aggregates at pH 5, in comparison with pH 2. Thus, there will exist more HEWL monomers than aggregates in the beginning of the aggregation (time = 2 hrs) at pH 5, due to which the interaction of MMG was not observed. However, even at later stages of aggregation, the same results were observed.

Since MMG was added to preformed aggregates, it was denied the accessibility for interaction. Therefore, a study was carried out where MMG was allowed to interact with HEWL aggregates during the entire aggregation process. For this, MMG was incubated with HEWL sample at pH 2 and pH 5 for 6 days.

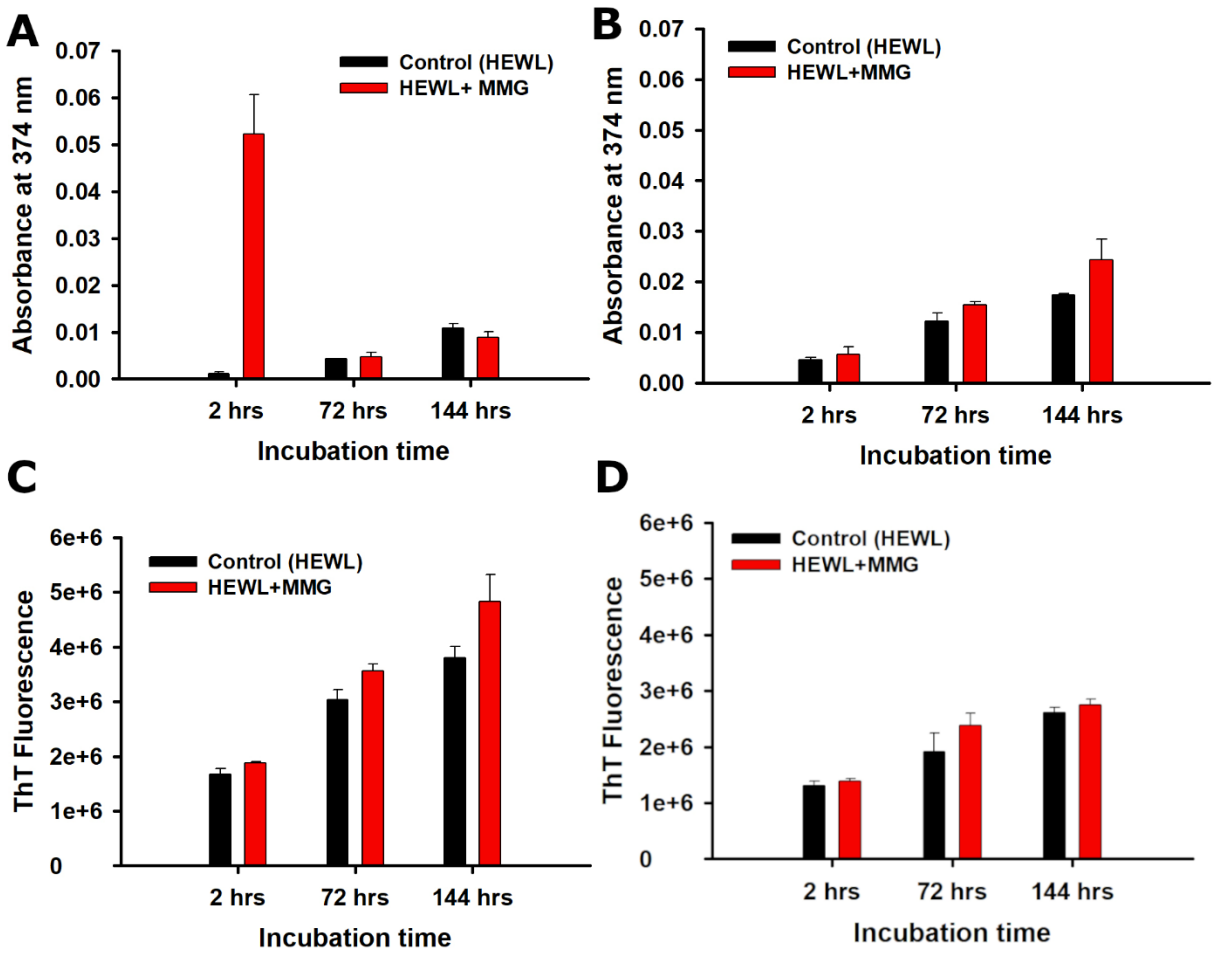

Figure 4.5: Absorbance of MMG (15 µM) at 374 nm in (A) HEWL aggregates (136 µM) at pH 2 and (B) HEWL aggregates (100 µM) at pH 5 over 144 hrs. ThT fluorescence assay of MMG (15 µM) in the presence of (C) HEWL aggregates (136 µM) at pH 2 and (D) HEWL aggregates (100 µM) at pH 5 over 144 hrs.

Even in this case, the interaction occurred in the initial aggregation stage at pH 2 but not during further maturation and fibrillation stages (**Fig 4.5 A**). While at pH 5 condition, there was no interaction observed at all time intervals (**Fig 4.5 B**), even though MMG was allowed to interact with HEWL throughout its aggregation. The ThT fluorescence revealed no inhibition of HEWL aggregates with time at both the pH (**Fig 4.5 C and D**).

It can thus be suggested that the nature of interaction could be transient hydrogen bonding and other non-covalent weak forces, which only existed at the initial stage of HEWL aggregation when the protein is partially unfolded and exposed. But these interactions were not sufficient for stable binding of MMG to the mature aggregates and fibrils.

4.3.2. Interaction of MMG with polycationic HEWL aggregates at pH 9

In the previous section, it was suggested that the partially unfolded HEWL or exposed hydrophobic regions of the aggregates in the beginning of aggregation was involved in the interaction with MMG. To strengthen this hypothesis, MMG was added to partially exposed polycationic HEWL aggregates (pHEWL) formed from matured aggregates. Ravi et al., (2014) have prepared pHEWL by transferring the aggregates formed at pH 12.2 to pH 7. In the current work, the mature HEWL aggregates obtained after 5 days incubation at pH 12.2 were transferred to pH 9 (below its pI ≈ 11). As a consequence, the protein attains high positive charges causing the mature aggregates to open up due to coulombic repulsions and then refold back.

MMG at high concentration (50 μM) was added at the partial unfolding stage of pHEWL aggregates (12 μM) at pH 9. There was increase in the absorption of MMG-pHEWL complex compared to pHEWL control and MMG control at pH 9, similar to pH 2 condition (**Fig 4.6**) indicating the occurrence of interaction. But MMG in pH 9 buffer and MMG-HEWL in pH 12.2 displayed red shift in the spectra, which appeared to have blue-shifted in MMG-pHEWL complex.

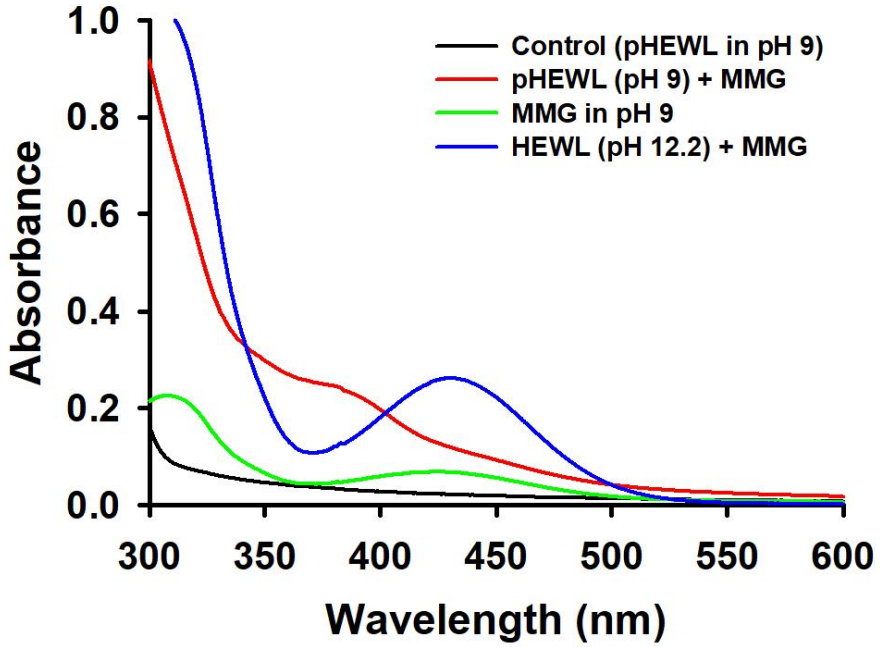

Figure 4.6: Absorption spectra of MMG (50 µM) in pHEWL aggregate complex at pH 9 along with pHEWL, MMG-HEWL at pH 12.2 and MMG in pH 9 buffer controls

Upon addition of different concentrations of MMG (5 µM, 15 µM, 30 µM and 50 µM) to pHEWL in pH 9, the peak was more broader (350-450 nm) at lower MMG concentrations, which resolved into a relatively sharper peak at 374 nm with linear increase in absorbance (**Fig 4.7 A**). While MMG at pH 9 displayed red-shifted spectra with λ_{max} at 442 nm in pH 9, due to ionization MMG (**Fig 4.7 B**). The shift of the peak from 442 nm to 374 nm in MMG-pHEWL complex indicates that the binding/interaction site in pHEWL should be in the interior of aggregate and protects MMG from the external solution. This assessment was also further validated when MMG was added to HEWL mature aggregate at pH 12.2. The spectra obtained was a fully red-shifted and does not reveal any protective aggregate interiors for MMG, unlike the case of pH 9 (**Fig 4.7 C**). The high absorption at pH 12.2 could be due to higher number of ionic form of MMG with higher aqueous solubility. Therefore, this effectively proves that the partial exposed regions of the aggregates are essential and possibly the sites for MMG interactions. **Fig 4.7 D** summarizes the changes in absorbance at 374 nm of MMG added to different HEWL systems, where MMG-pHEWL displayed highest absorbance due to hypsochromic spectral shift.

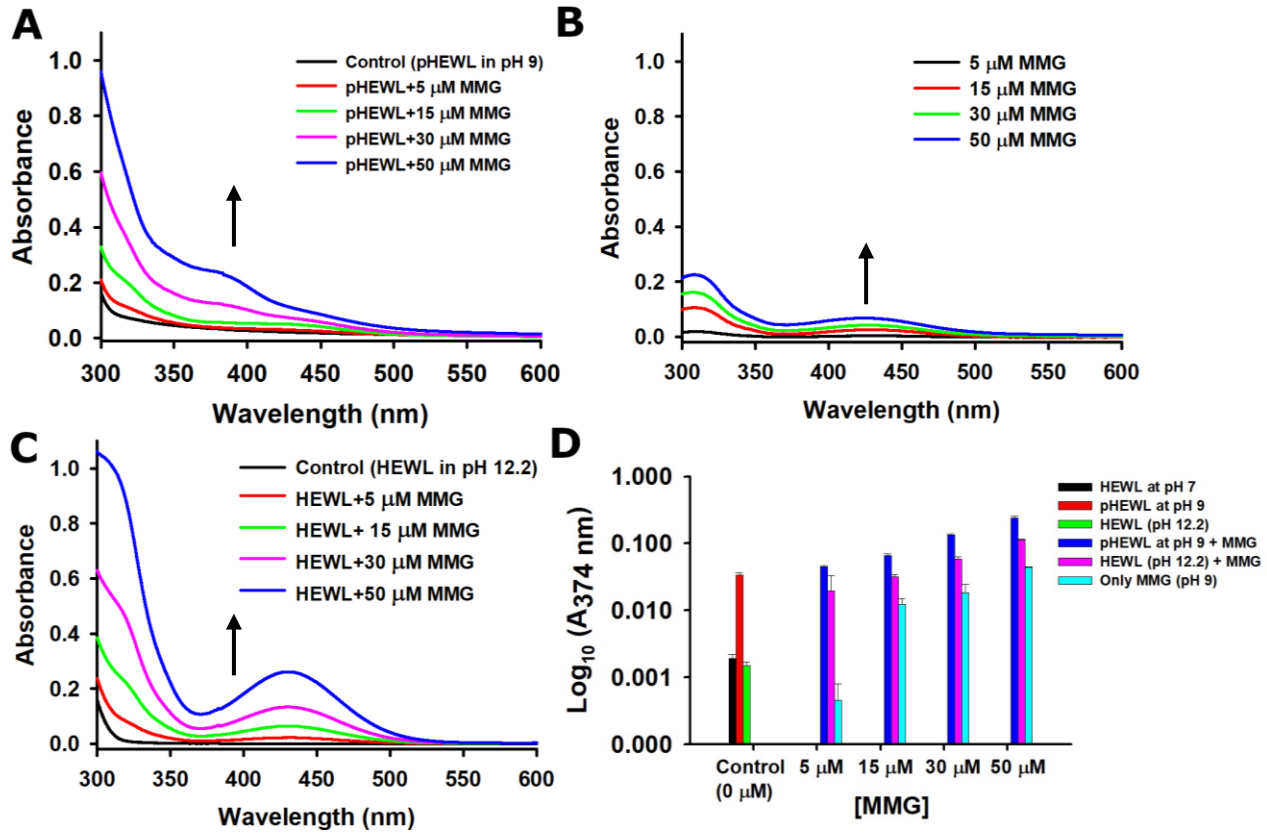

Figure 4.7: Absorption spectra of MMG at different concentrations (5 μM, 15 μM, 30 μM and 50 μM) in (A) pHEWL at pH 9, (B) pH 9 buffer, (C) HEWL at pH 12.2. (D) Absorbance (in $\log_{10}$ scale) of MMG at 374 nm in different conditions. Arrow mark indicates increase in absorption. [Arrow marks indicate increase in absorbance]

Such protective effect of proteins to nutrients molecules was demonstrated in previous studies, where protein prevents direct contact of food nutrients with the aqueous medium and in turn improving its solubility and stability (Chang et al., 2022).

4.3.3. MMG in surfactant micelles at pH 9

In the previous section, it was observed that MMG upon entering an enclosed environment like protein aggregates gets protected from being ionized in alkaline environment resulting in the absorption spectral differences. Mimicking the same in the surfactant micelles at pH 9, further validated the results. MMG was added to the surfactant micelles of different charges at pH 9, at concentrations above and below their cmc.

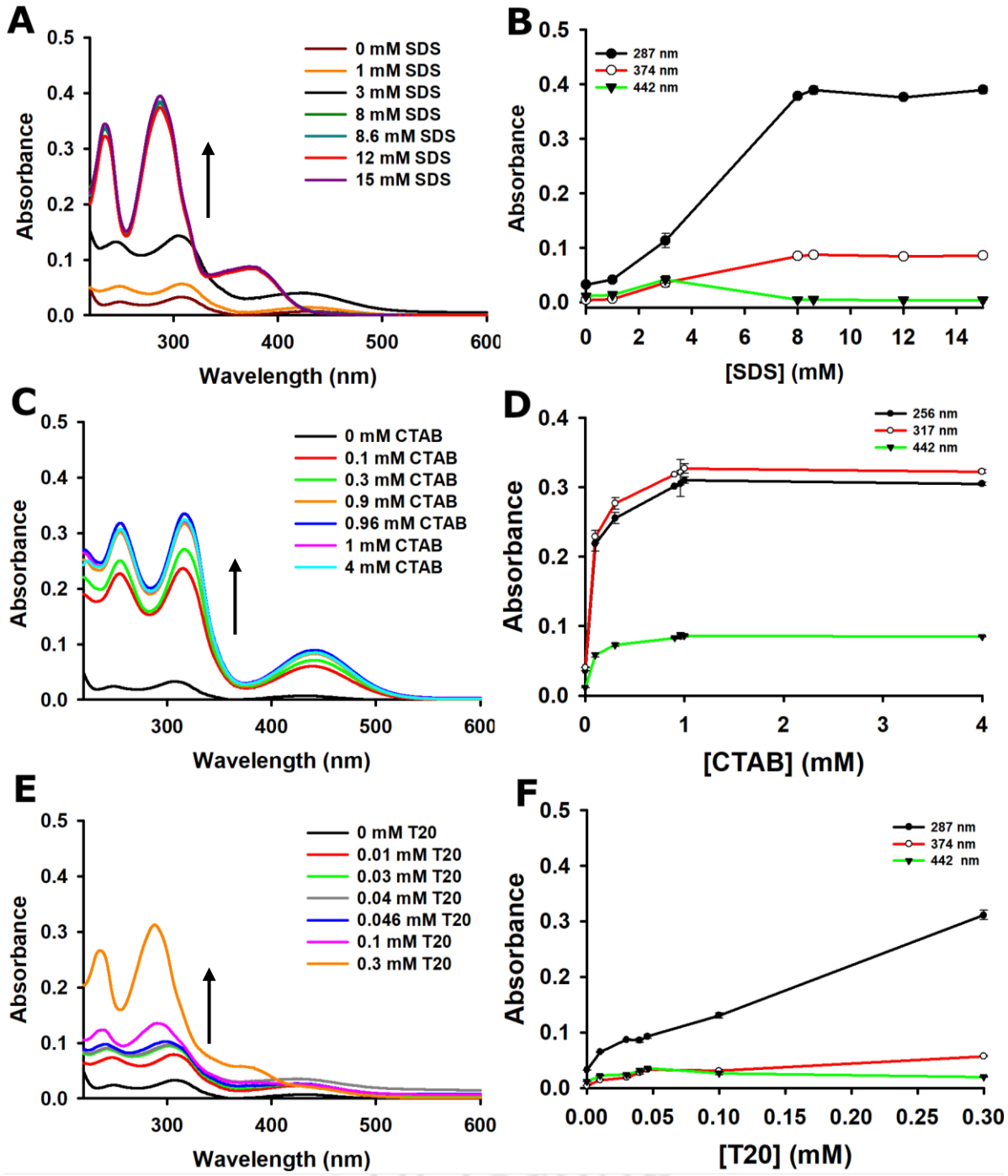

Figure 4.8: Absorption spectra of MMG in different concentrations of (A) SDS, (C) CTAB, (E) T20. Absorbance of MMG at different wavelengths in various concentrations of (B) SDS, (D) CTAB, (F) T20. Arrow marks indicates increase in absorption.

In case of SDS in pH 9 at concentrations below cmc, MMG displayed a red-shifted spectrum with the rise in intensity with increasing SDS concentration (**Fig 4.8 A**). At SDS concentrations beyond the cmc (≥ 8 mM), it displayed blue-shifted spectra same as that observed for the native nonionized MMG in aq. SDS, with saturation in the absorbance with increasing concentrations of SDS (**Fig 4.8 B**). In the case of CTAB, there was increase in the

absorbance observed with increasing concentrations of CTAB, which reached saturation after cmc (0.9 mM) of CTAB. But the bathochromic shift existed at all the concentrations of CTAB unlike that of SDS (**Fig 4.8 C and D**). Similar kind of blue-shifted spectra as SDS was observed in T20 at very high concentrations (0.3 mM), with increase in absorbance. While at the cmc of T20, the spectra of MMG was still red-shifted (**Fig 4.8 E and F**).

With the above results, it can be inferred that at concentration ≥ cmc of SDS, hydrophobic interactions due to the micelle formation resulted in encapsulation of MMG into the micelle, thus protecting it from the surrounding environment. The same is the case for T20 at much higher concentrations. This can be attributed to unique molecular structure and composition of T20. The red-shifted spectra of MMG at low concentrations of T20 can indicate the accessibility of solvent inside the micelles. On the other hand, MMG remained in the ionized form at all the concentrations of CTAB, suggesting the presence of strong electrostatic interactions with the CTAB head group as well as hydrophobic interactive forces due to micellization, leading to stabilization of MMG.

When comparing with MMG-pHEWL interactions, the spectral properties are similar to that of SDS and T20. Although the charges on pHEWL at pH 9 are positive similar to CTAB, MMG-pHEWL complex does not yield red-shifted spectra. This suggested that the hydrophobic interaction is the key force governing the binding of the MMG to pHEWL and the positive charges in the pHEWL were not strong enough for electrostatic interaction, as observed in CTAB.

4.3.4. HEWL aggregates vs surfactants

The environment of MMG in HEWL aggregates was compared with surfactants. From **Table 4.1** and **Fig 4.9**, it was observed that the extinction coefficient of MMG in HEWL aggregates were comparable to that of surfactant micelles, which suggested that MMG experienced similar hydrophobic environment in HEWL aggregates as in surfactants. When comparing MMG in HEWL aggregates in pH 2 and pH 9 conditions, the Ɛ at pH 2 was higher. This could be attributed to higher HEWL concentration (136 μM) at pH 2 than that in pH 9 (12 μM), resulting in more hydrophobic interactions at pH 2. As a consequence, more number of MMG gets incorporated into the aggregates than in the bulk solution. Since, MMG-pHEWL complex at pH 9 occurs at lower HEWL concentration, it resulted in a much wider distribution of MMG in the pHEWL as well as in the bulk solution, resulting in shorter and

broader absorption peak yielding lower Ɛ for MMG-pHEWL complex. On the contrary, HEWL aggregates at pH 5 did not exhibit any interactions with MMG, resulting in extremely low Ɛ ($Ɛ_{300\ nm}$ = 87 ± 51 $M^{-1}cm^{-1}$; $Ɛ_{317\ nm}$ = 35 ± 22 $M^{-1}cm^{-1}$; $Ɛ_{374\ nm}$ = 17.3 ± 11 $M^{-1}cm^{-1}$ and $Ɛ_{442\ nm}$ = 12 ± 6 $M^{-1}cm^{-1}$).

Table 4.1: Extinction coefficient of MMG in in HEWL aggregates and comparison with other solvent systems

	Ɛ ($M^{-1}cm^{-1}$)			
	300 nm	**317 nm**	**374 nm**	**442 nm**
MMG in HEWL aggregates at pH 2	19016 ± 444	12804 ± 236	6667 ± 135	1798 ± 54
MMG in HEWL aggregates at pH 5	87 ± 51	35 ± 22	17.3 ± 11	12 ± 6
MMG in pHEWL aggregate at pH 9	14250 ± 368	10338 ± 351	3838 ± 125	1701 ± 44
SDS (20 mM)	20991 ± 233	9301 ± 90	5708 ± 67	186 ± 4.4
CTAB (5 mM)	15898 ± 220	10788 ± 296	4924 ± 34	1048 ± 115
T20 (0.5 mM)	18897 ± 616	7129 ± 224	4642 ± 147	162 ± 7

When comparing, MMG in HEWL aggregates with the surfactants, MMG-HEWL aggregates at pH 2 had higher Ɛ at 300 nm, 317 nm, 374 nm and 442 nm compared to CTAB and T20 micelles. This could be due to more heterogeneity of HEWL aggregate solution resulting in wider distribution of MMG compared to CTAB and T20. But in case of MMG in SDS, the Ɛ at 300 nm was slightly higher, while Ɛ at 317 nm, 374 nm and 442 nm were lower than HEWL aggregates at pH 2, suggesting SDS provided more non-polar pockets than the aggregates. To conclude, HEWL aggregates at early stages were able to provide the hydrophobic interior required for MMG solubilization, similar to surfactant micelles.

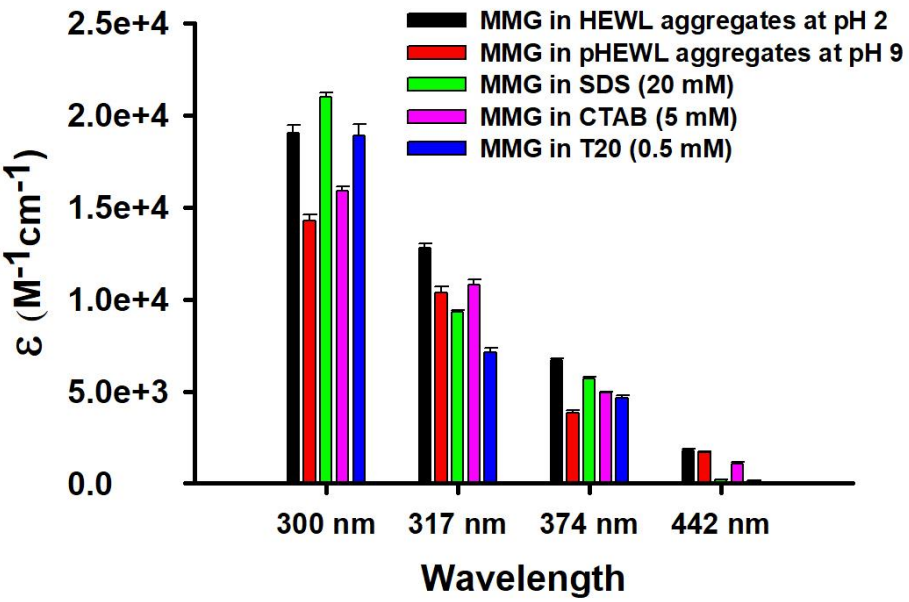

Figure 4.9: Extinction coefficient of MMG in HEWL aggregates at different pH and comparison with surfactant micelle systems

4.4. Conclusions

Interaction of MMG with HEWL aggregates at pH 2, pH 5 and pH 9 was investigated. MMG displayed improved solubility upon interactions with early aggregates of HEWL, which resulted in increase of absorption with MMG concentration at pH 2. However, there was decrease in absorption at the later stages of aggregation resulting from reduced penetration into mature aggregates and fibrils. On the contrary, MMG did not show any interaction with HEWL aggregates at pH 5, attributed to slower aggregation in that condition. Overall, MMG did not stably remain bound to HEWL aggregates with time, suggesting unstable binding with HEWL aggregates. When interacting with pHEWL at pH 9, MMG displayed a blue-shifted spectra which otherwise yielded red-shifted spectra in pH 9 buffer due to ionization. Therefore, partial unfolding of HEWL with exposed hydrophobic regions of aggregates was essential for interaction of MMG with HEWL aggregates. The environment of surfactant micelle was effectively recreated in HEWL aggregates.

Chapter 5

Investigating Mammeigin as acid-base pH indicator in surfactant systems and its structural characterization in alkaline conditions

5.1. Introduction

Flavonoids apart from their role in defense and relieving stress in plants, are involved in flower and fruit coloration, which in turn produce visual cues for pollinators (Harborne and Williams, 2000). These molecules belong to the subclass of flavonoids called anthocyanins. Depending on the pH inside the cell or vacuole, they produce different color hues in flowers and fruits. Due to pH sensitivity of these molecules, they are used as dyes, food colorants and producing different wine colors (Lapidot et al., 1999; Stavenga et al., 2021; Wahyuningsih et al., 2017). In this chapter, we will be focusing on the application of plant polyphenols as pH indicators.

Some examples of plant polyphenols and their extracts displaying properties as pH indicator are red rose juice, cherry and blueberry grape juices, brazil-wood, litmus, red cabbage, tea polyphenols and so on (Mohd et al., 2011). The coloration at each pH depends on the chemical properties of the phenolic constituents. Plant molecules like flavonoids, xanthones, anthocyanins and azo compounds produce these color hues. Some of these like red cabbage, exhibit different colors at different pH, due to which they can be used as an alternative for synthetic indicators (Abedi-Firoozjah et al., 2022).

These changes in colors are attributed to the presence of -OH groups, catechol moieties and C2-C3 double bond, leading to formation of phenoxide forms, quinoidal forms, carbinol pseudo-base forms and chalcone forms (Jurasekova et al., 2014; Mohd et al., 2011; Proestos et al., 2018). Thus pH affects the stability of such compounds (Friedman and Jürgens, 2000; Jurasekova et al., 2014), their anti-oxidant properties (Devi et al., 2021) and also their spectroscopic properties (Amat et al., 2009; Camuri et al., 2018; Favaro et al., 2007).

In the previous chapter it was observed that MMG displayed red-shifted spectra at alkaline pH (pH 9 and 12). Thus, this chapter focuses on further investigating the spectroscopic properties of MMG at different pH in different solvent systems like pH buffers and surfactant systems. The stability of MMG at different pH in the solvent systems was investigated. Further characterization of MMG in pH 13 condition is discussed.

5.2. Materials and Methods

5.2.1. MMG in different pH conditions

MMG (15 μM) from ethanol stock was added to aqueous buffers of different pH, such that the final ethanol concentration was 1 % (v/v). The pH buffers were prepared as per **Table 5.1.**

Table 5.1: Buffer compositions (Ansari et al., 2018; "Buffer Reference Center," www.sigmaaldrich.com)

pH	Buffer composition
2	10 mM Glycine
3	82 mM Citric acid, 18 mM Sodium Citrate
4	59 mM Citric acid, 41 mM sodium Citrate
5	0.1 M Sodium citrate
6	12.2 mM Na_2HPO_4, 87.5 mM NaH_2PO_4
7	50 mM NaH_2PO_4
7.5	87 mM Na_2HPO_4, 13 mM NaH_2PO_4
8	94.7 mM Na_2HPO_4, 5.3 mM NaH_2PO_4
8.5	0.1 M Glycine
9	20 mM Na_2CO_3, 80 mM Na_2HCO_3
9.5	40 mM Na_2CO_3, 60 mM Na_2HCO_3
10	70 mM Na_2CO_3, 30 mM Na_2HCO_3
10.5	90 mM Na_2CO_3, 10 mM Na_2HCO_3
11	99 mM Na_2CO_3, 1 mM Na_2HCO_3
12	50 mM Na_2HPO_4
13	0.1 M NaOH

The samples were vortexed, incubated for 1 hr and centrifuged prior to collecting absorption spectra in the range of 220-600 nm.

To observe time-dependent changes in the absorption spectra of MMG at different pH conditions, the spectra were collected at the time intervals of 1 hr, 6 hrs, 12 hrs and 24 hrs.

5.2.2. MMG in different surfactants at different pH

Surfactant micelle systems SDS (20 mM), CTAB (5 mM) and T20 (0.5 mM) were prepared in buffer solutions of pH 2, 5, 7, 9, and 12. MMG (15 μM) from ethanol stock was added these surfactants, vortexed for 5 minutes, incubated for 1 hr and absorption spectra were collected in the range of 220-600 nm.

For MMG in CTAB micelles, CTAB (5 mM) was prepared in different pH buffers (pH 2-13) and absorption spectra were recorded. Also, the spectra were collected at different time intervals, 1 hr, 6 hrs, 12 hrs and 24 hrs. Absorbance at wavelengths 234, 256, 287 nm, 317 nm, 374 nm and 442 nm were noted to observed the spectral changes of MMG.

5.2.3. MMG in pH 13

MMG from ethanol stock was added to pH 13 (0.1 M NaOH) and absorbance was collected at different time intervals upto 1 week to study the stability of MMG in pH 13. To investigate reversibility of MMG in pH 13, the stock was prepared in pH 13 and diluted into buffers of different pH 13 →2. Absorption spectra were collected for MMG at different pH conditions.

To further structurally characterize MMG in pH 13, isolation and purification based on the physical properties was carried out. Organic-aqueous two phase separation was carried out by adding mixtures of ethanol and ethyl acetate to MMG in pH 13. The solution was shaken well and the organic phase was separated. The organic fraction was subjected to 3-4 round of recrystallization using aq. ethanol. The mixture separated into crystalline fraction and non-crystalline fraction. Both of these fractions were subjected to HPLC, MS and NMR analysis. HPLC (Shimadzu) of the samples were run using C18 column with mobile phase of acetonitrile in water [5-100% v/v (0-10 min); 100 % v/v (10-15 minutes); 5% v/v (15 – 25 minutes)] at 1 ml/min flow rate and detected at 286 nm. The mixtures in non-crystalline fraction were purified using the above HPLC method. LC-MS (Agilent Technologies) was carried out and MS-ESI positive mode spectra for both the fractions. NMR for all the individual purified compounds were carried out in Bruker 600 in solvent $CDCl_3$.

5.3. Results and Discussions

5.3.1. MMG in different pH conditions

The absorption spectroscopic properties of MMG were investigated in buffers of different pH. The compound was found to be completely insoluble at acidic and neutral pH (pH 2-8). From pH 9 onwards, there was partial solubility resulting in red-shifted absorption spectra, with λ_{max} at 256 nm, 317 nm and 442 nm (**Fig 5.1 A**). With increasing pH > 9, there was gradual increase in absorption observed which plateaued out after pH 11 (**Fig 5.1 B**).

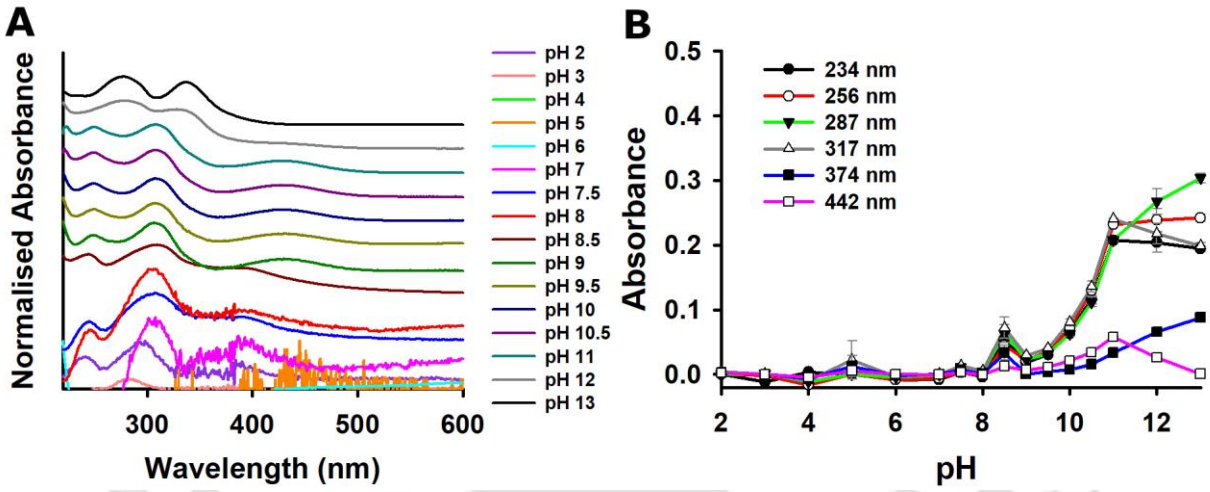

Figure 5.1: (A) Normalised absorption spectra of MMG (15 µM) in buffers of different pH [the spectra are stacked by shifting upwards (for spectra ≥ pH 7.5) for clarity] (B) Absorbance of MMG at different wavelengths. Arrow mark showing increase in spectra.

The plateauing of absorbance beyond pH 11 was attributed to emergence of different spectral pattern. At pH 12, there was loss of 256 nm peak and appearance of blue-shifted peaks at 277 nm and 336 nm. It became more prominent at pH 13. These spectral changes were observed visually as color change of the medium with pH changes. **Fig 5.2 A** depicts the development of yellow coloration which was observed to be distinct at pH 9.5 to 12 as soon as MMG was added.

Such development of yellow coloration from acidic to alkaline pH conditions was also reported for other flavonoids like quercetin (Yazdanshenas and Gharib, 2016). In case of curcumin too there was red spectral shift observed at alkaline pH resulting in development of yellow to red color (Priyadarsini, 2009). In case of anthocyanins, a wide range of color changes are reported at different pH depending on the -OH groups, C2-C3 double bond and presence of glycosidic moiety (He et al., 2012; Mohd et al., 2011; Rakić et al., 2015;

Sigurdson et al., 2019). Thus, in case of MMG it is likely to be due to ionization of -OH group resulting in subsequent phenoxide and quinoidal base forms of MMG.

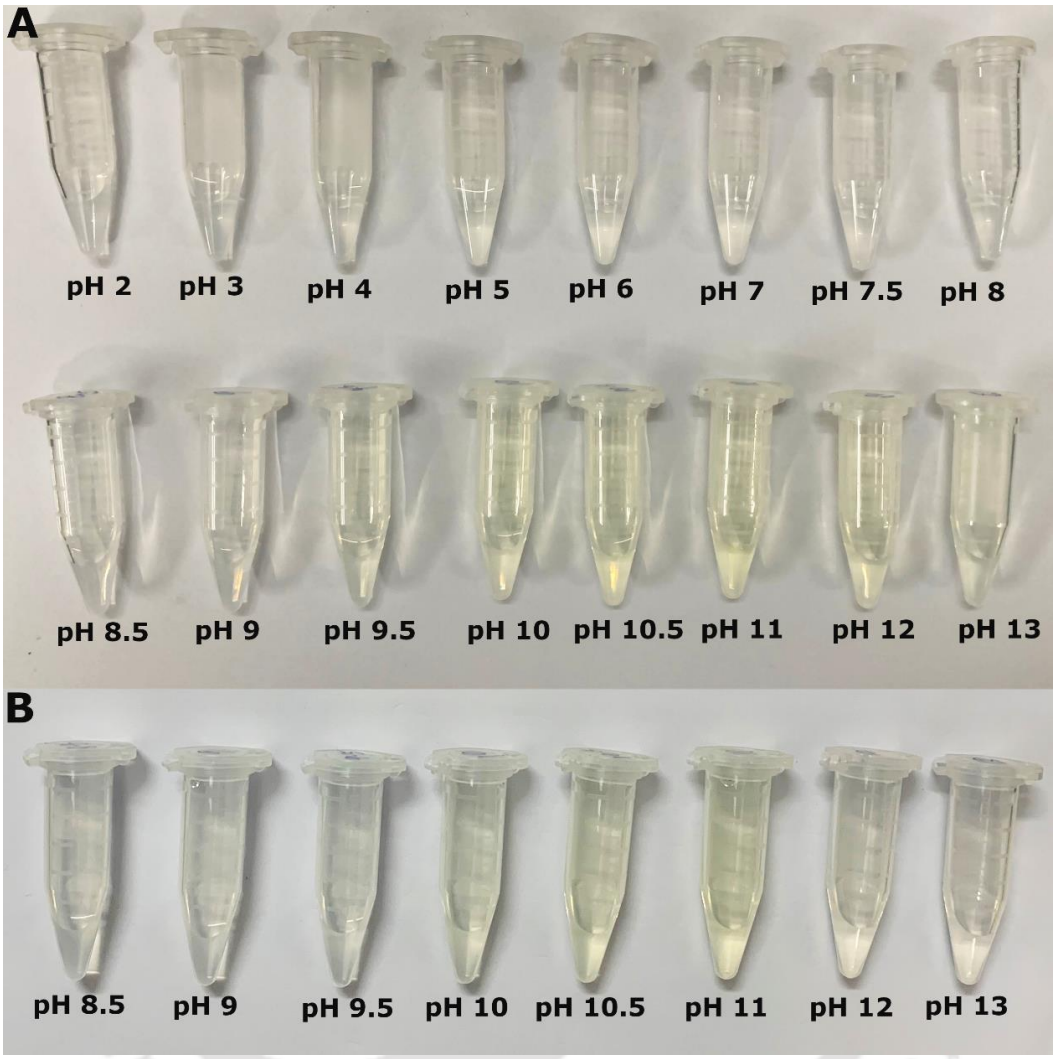

Figure 5.2: Difference in coloration of MMG (15 μM) with increase in pH observed after (A) 15 minutes and (B) 30 minutes.

It was also observed that the color disappeared within 1hr hour of incubation. Mild coloration was observed only at pH 10, 10.5 and 11 (**Fig 5.2 B**). This loss of coloration and instability will be discussed later in this chapter.

5.3.2. Effect of pH on MMG in different surfactants

Since MMG was found to be insoluble at pH 2-8, MMG was added to aqueous surfactant micelle solutions i.e., SDS (20 mM), CTAB (5mM) and T20 (0.5 mM) at different pH conditions (pH 2, 5, 7, 9, 12). It was observed that the solubility improved in the presence of all the three surfactants at all the pH investigated especially at acidic and neutral pH (**Fig 5.3**

A, B,C). However, there was mild spectral transition occurring at pH 7 in the presence of CTAB micelles, which was fully red-shifted at pH 9 (**Fig 5.3 C and D**).

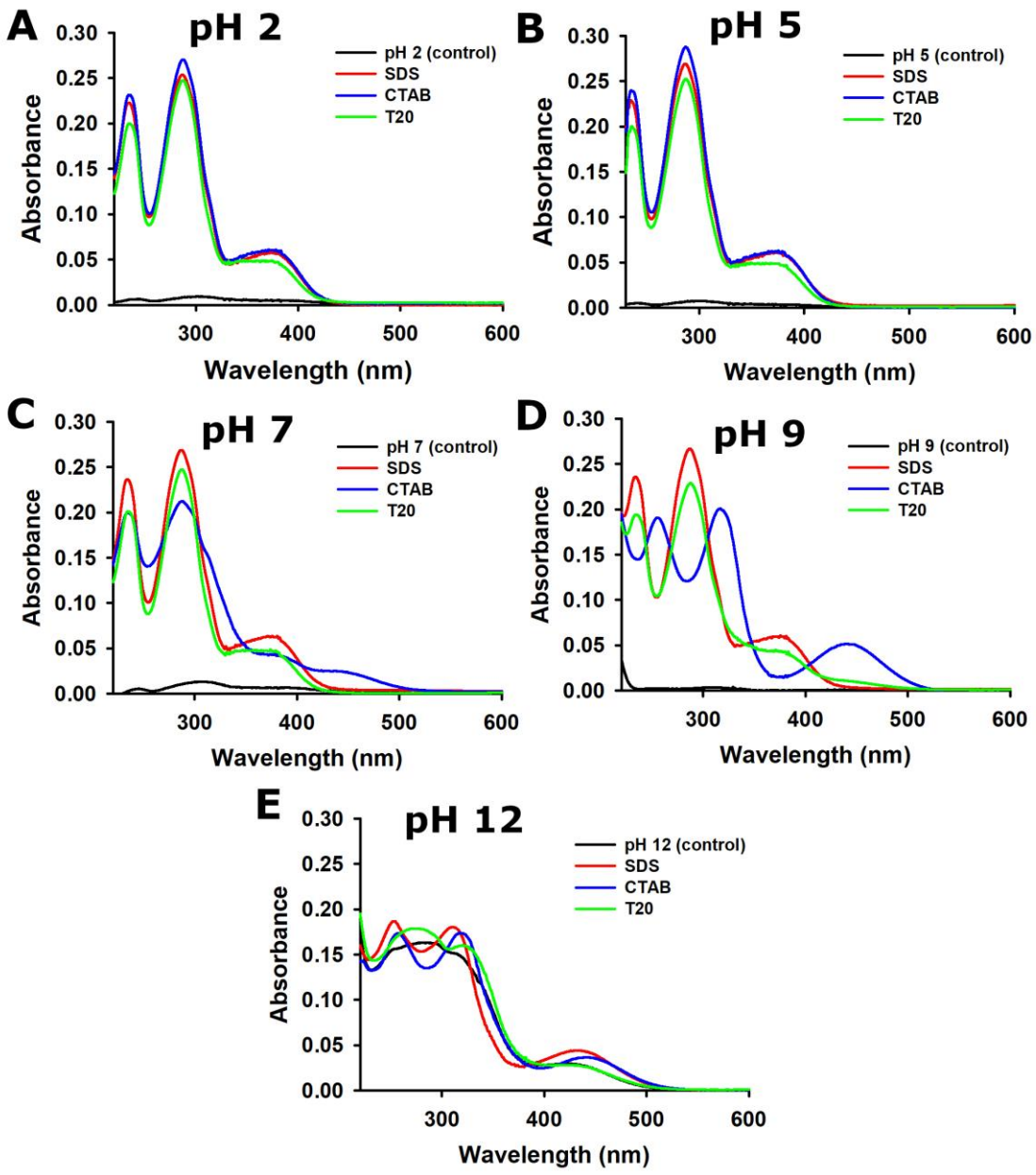

Figure 5.3: Absorption spectra of MMG (15 µM) in SDS (20 mM), CTAB (5 mM), T20 (0.5 mM) at (A) pH 2, (B) pH 5, (C) pH 7, (D) pH 9, (E) pH 12

As discussed in the previous chapter, the bathochromic spectral shift could result from electrostatic interactions between MMG and CTAB head-group (Saraf et al., 2018). In the case of pH 12, there were change in spectra observed at all the surfactant conditions, including control (**Fig 5.3 E**). Since MMG in CTAB (5 mM) solution at different pH displayed pH-dependent spectral transitions, this solvent system was further investigated.

5.3.3. MMG at different pH in the presence of CTAB

When MMG was added to CTAB (5 mM) solution in buffers of different pH, there was brighter hue of yellow colour developed at alkaline pH (pH 7.5 onwards) (**Fig 5.4**). Unlike the buffers, MMG in CTAB micelles displayed a clear demarcation in distinguishing pH from acidic to alkaline medium through change in colour from colourless to yellow.

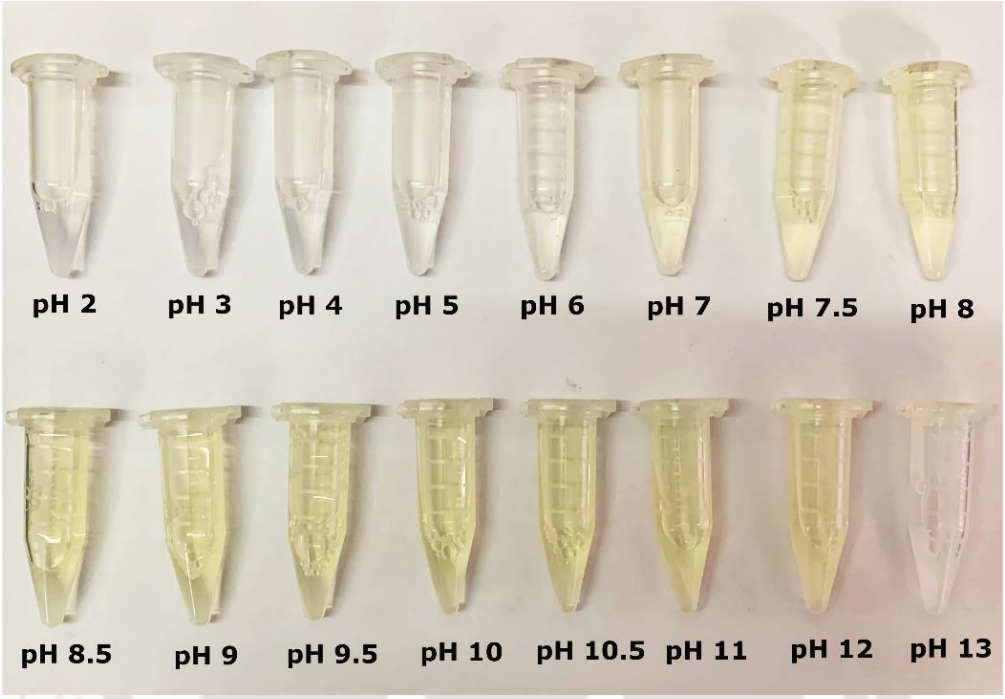

Figure 5.4: Difference in coloration of MMG (15 μM) in CTAB (5 mM) at different pH.

This change in colour was also reflected as change in absorption spectra of MMG (**Fig 5.5 A**). The pH from 2-6 displayed similar spectrum as that in aq. surfactants and organic solvents corresponding to the native non-ionic form, due to which the solution was colourless. At pH conditions 7, 7.5 and 8, the absorption spectra started to undergo slight bathochromic shift. At pH ≥ 8.5, a fully red-shifted spectrum was obtained. The solution however faded at pH 13, which resulted in similar spectral pattern as pH 13 control without CTAB. Unlike the case of buffers, the absorbance intensity at each wavelength was higher in the presence of CTAB (**Fig 5.5 B**). And also, the development of yellow coloration occurred at pH ≥ 7.5 itself while in buffers it was at pH ≥ 9.5. It is reported that the ionic surfactants can shift the pK_a of dyes by 5-6 units in dye-surfactant ion pairs through hydrophobic-electrostatic interactions and H-bonding. It results from strong electron withdrawing or releasing effects (Dutta et al., 2013). Therefore, the current outcome could correspond to the same.

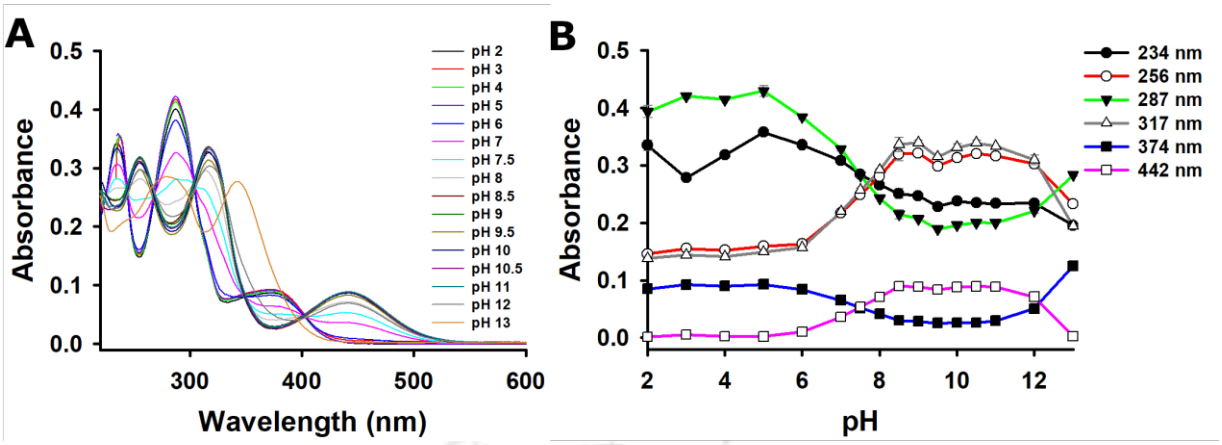

Figure 5.5: (A) Absorption spectra of MMG (15 µM) and (B) Absorbance of MMG (15 µM) at different wavelengths in buffers of different pH containing 5 mM CTAB

5.3.4. Comparing MMG in CTAB micelle and buffer

The stability of MMG in CTAB was investigated at different time intervals viz., 1 hr, 6 hrs, 12 hrs and 24 hrs in CTAB and in buffers of different pH.

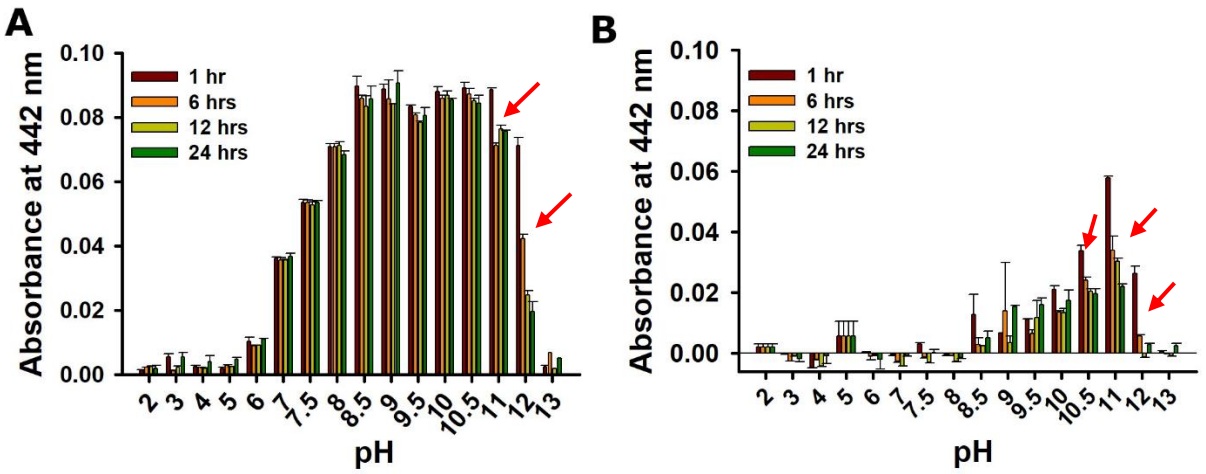

Figure 5.6: Absorbance of MMG (15 µM) at 442 nm at 1hr, 6hr, 12 hr and 24 hr (A) in CTAB (5 mM) and (B) buffer. Arrow marks showing decrease in absorbance.

There was enhanced stability of MMG at all the pH conditions over 24 hrs in CTAB micelle, except in the case of pH 11 and 12 (**Fig 5.6 A**). Whereas in buffers, there was drop in the absorbance at pH 10, 10.5, 11, 12, which could be due to instability of MMG (**Fig 5.6 B**).

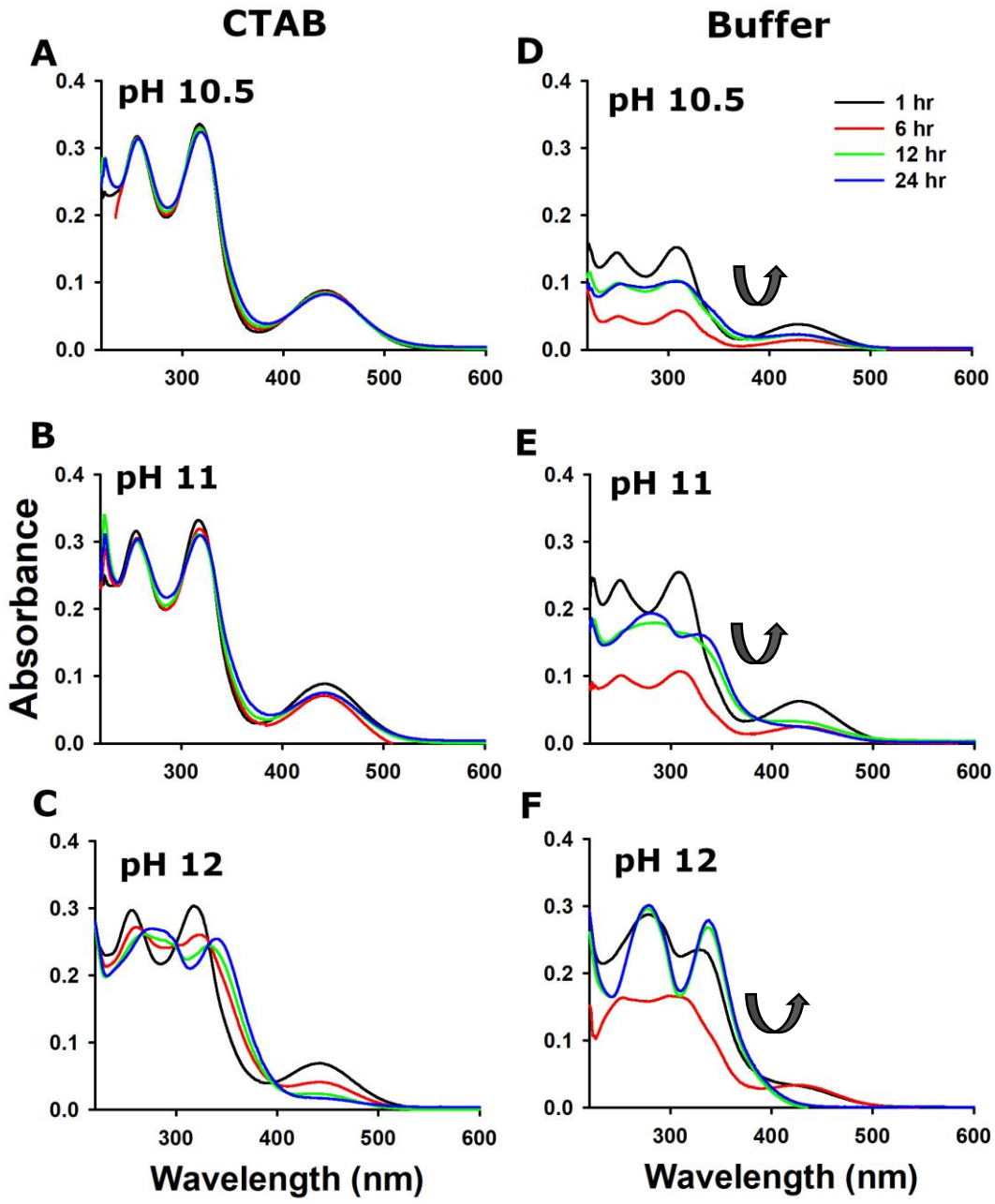

Figure 5.7: Absorption spectra of MMG in (A, B, C) CTAB and buffers (D, E, F) at pH 10.5, 11 and 12 respectively. Arrow marks showing decrease then increase in the absorption.

The instability of MMG at pH 10.5, 11 and 12 was compared in CTAB micelles and in buffers in terms of absorption spectra. In case of CTAB, MMG was fairly stable in pH 10.5 and pH 11 with a subtle decrease in the absorption (**Fig 5.7 A and B**). While at pH 12, there was decrease in absorption accompanied by spectral change, but not as much as the case of buffers (**Fig 5.7 C**). Since the buffers had salts, the influence of the electrolytes would have caused change in morphology of CTAB micelles from spherical-to-ellipsoidal shape

(Chatterjee and Suresh Kumar, 2016; Kuperkar et al., 2010). The instability of MMG at pH 12 could be due to branched networking of the elongated CTAB micelles resulting in destabilization at those pH conditions (Patel et al., 2014).

In case of buffers, there was drastic decrease in the absorption from 1 hr to 6 hrs at the pH 10.5, 11 and 12. At 12 hrs and 24 hrs, there was an increase in the absorption due to spectral change at these pH, more prominently at pH 12 (**Fig 5.7 D, E and F**). In case of phenolic compounds, such changes in the absorption spectra are correlated to formation of quinone oxidation products at alkaline conditions (Friedman and Jürgens, 2000) for galangin (Park et al., 2017), quercetin (Wang and Zhao, 2016), methyl gallate (Zhang et al., 2018) and so on.

5.3.5. MMG at pH 13

It was observed that MMG at pH 13 yielded a different spectra due to which it was further explored. The absorption spectrum at pH 13 was very different from native MMG in ethanol (**Fig 5.8 A**). There was an overall blue shift in the spectrum with increase in intensity at 336 nm. The peak at 234 nm was missing altogether. Increase in the intensity of the shoulder peak 336 nm is indicative of formation of quinoidal base forms (Jeon et al., 2013).

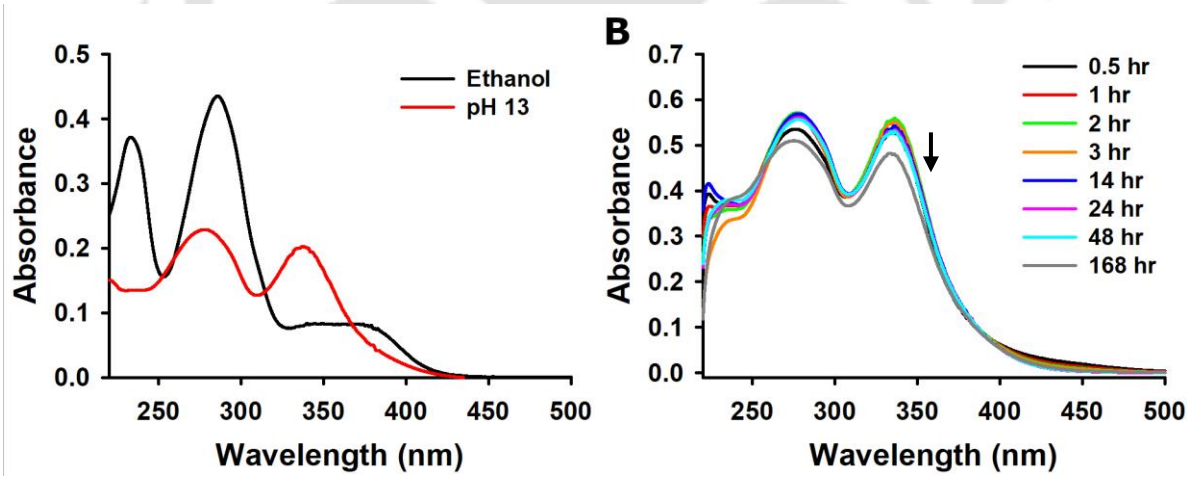

Figure 5.8: (A) Change in spectra – comparison between native MMG (in ethanol) and pH 13. MMG = 15 µM (B) Absorption spectra of MMG in pH 13 with time 0-168 hrs. Arrow mark showing mild decrease in absorption.

Flavonoids have been reported to undergo alkaline degradation in such conditions. To confirm the occurrence of such possibilities, the absorption spectra was monitored over a period of 1 week. It was found that the spectral signature did not change, although a slight

increase at initial periods, followed by slight decrease at later time periods of incubation was observed (**Fig 5.8 B**). Overall it resulted in decrease of 5% and 8% in the absorbance of MMG at 277 nm and 336 nm respectively, from 0.5 hr to 168 hr, hence not quite significant.

It is yet unclear if the spectral change is an ionic form of MMG or any permanent structural change. Therefore, pH titration was carried out where MMG from pH 13 was transferred to buffers of different pH. It was observed that there was not much of a difference in the spectra from pH 13 to 9. The absorbance at 277 nm and 336 nm started to decrease from pH 8 up to pH 2, with drastic decrease observed in 336 nm peak (**Fig 5.9 A and B**). This transition of spectra suggested formation of protonated forms of modified MMG as the pH decreased from pH 13 to 2. However, the absorption spectra did not revert back to that of the native compound. Moreover, the modified MMG was found to be soluble at acidic and neutral pH condition, in contrast to the native MMG. It can thus be concluded that there is a stable permanent structural change MMG undergoes at extreme alkaline condition.

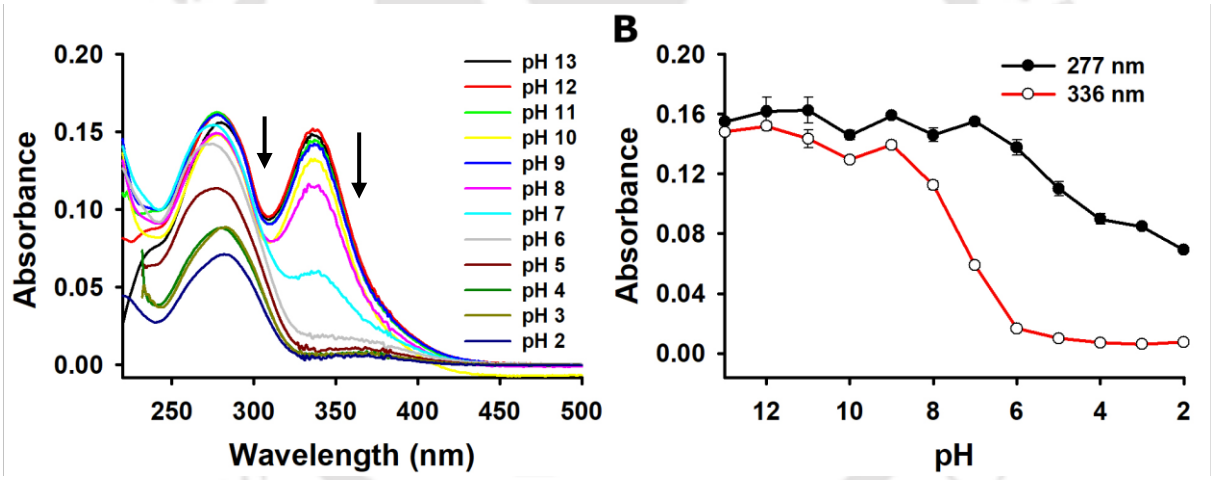

Figure 5.9: (A) Absorption spectra of MMG from pH 13 to 2 in different pH buffers and (B) the corresponding absorbance at 277 nm and 336 nm. Arrow marks indicating the decrease in the absorbance.

5.3.6. Characterization of MMG in pH 13 condition

The isolate obtained from pH 13 medium was a mixture of three or more compounds along with other molecular debris, which were analysed through HPLC. The retention time of MMG was 19.33 minutes (**Fig 5.10 A**) and the corresponding absorption spectra (**Fig 5.10 a**) was taken as reference. In the pH 13 mixture, the crystalline fraction was found to be the most abundant. The crystalline compound had retention time 19.31 min and absorption spectra same as native MMG (**Fig 5.10 B and b**). The mass of the compound was found to 404.16 Da through LC-MS, which also matched with that of MMG.

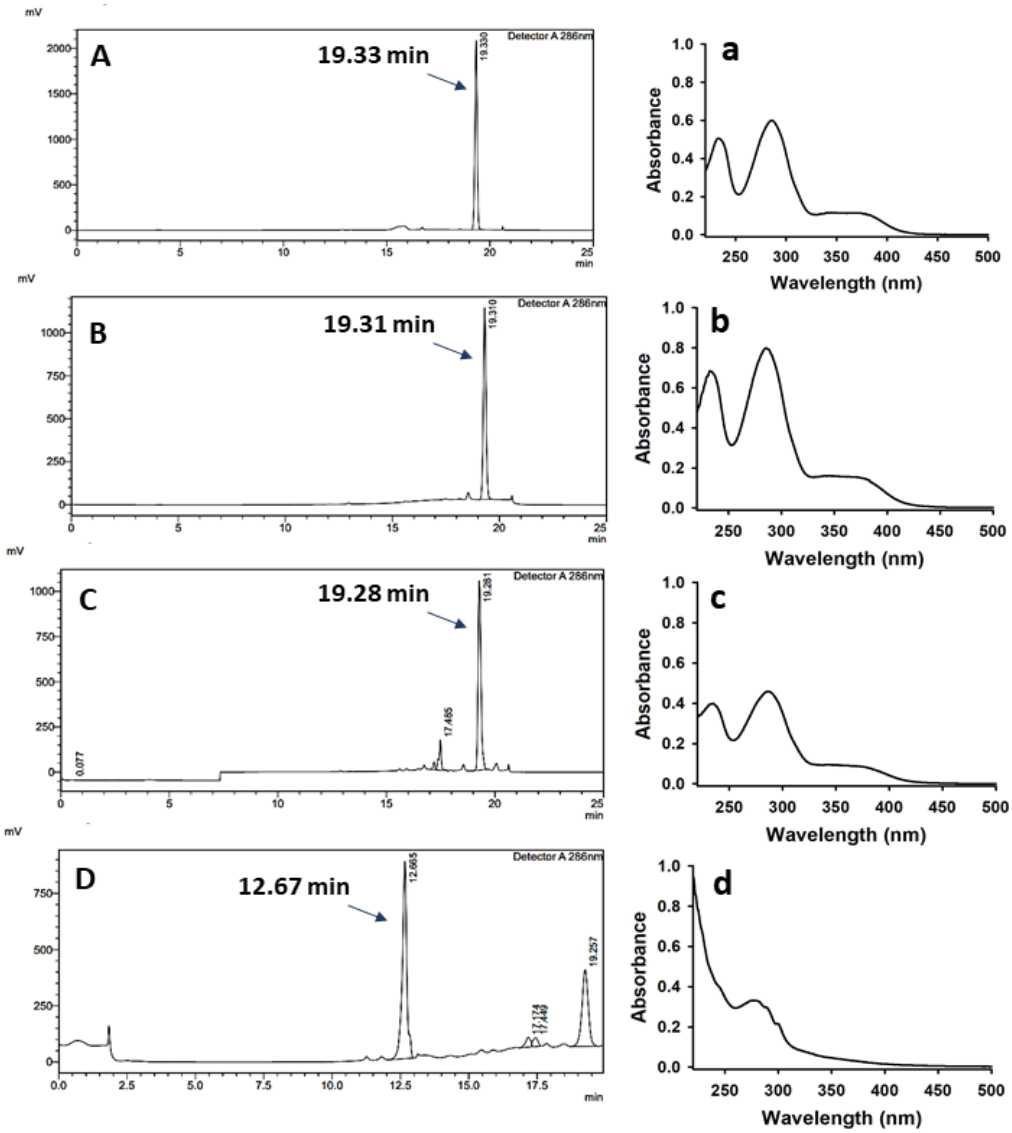

Figure 5.10: HPLC chromatogram and absorption spectra of (A and a) MMG (native), (B and b) crystalline fraction, (C and c) non-crystalline compound A and (D and d) non-crystalline compound B

The uncrystallized fraction revealed the presence of two or more compounds whose abundance varied with every reaction mix. The compound peaks with higher intensities i.e., 19.25 min retention time peak (Compound A) and 12.67 min peak (Compound B) were further analysed (**Fig 5.10 C and D**). Compound A was yellow coloured and displayed similar absorption spectra as native MMG (**Fig 5.10 c**). Unlike MMG crystals, it was a yellow coloured sticky compound. While compound B was colourless and yielded similar absorption spectra as the protonated form depicted in Fig 5.9 (**Fig 5.10 d**), unlike MMG. From LC-MS data, the masses of these peaks were 404.16 Da (Compound A) and 422.179 Da (Compound B).

Further characterization was carried out with ^{1}H NMR. The ^{1}H NMR spectra of MMG was used as reference (**Fig 5.11 A**). The crystalline compound from crystalline fraction yielded same NMR spectra as Fig 5.11 A and was thus confirmed to be native MMG (**Fig 5.11 B**). The non-crystalline fraction was very less abundant comparatively. The purified compound A and B after HPLC purification yielded even less amounts of the compound fractions, due to which the NMR of these compounds were inconclusive for the entire structural elucidation. Also, there were peaks from debris which overlapped with the signal especially at lower ppm (**Fig 5.11 C and D**). Therefore, NMR spectra of compound A and B was used to predict only the possible sites of chemical reaction.

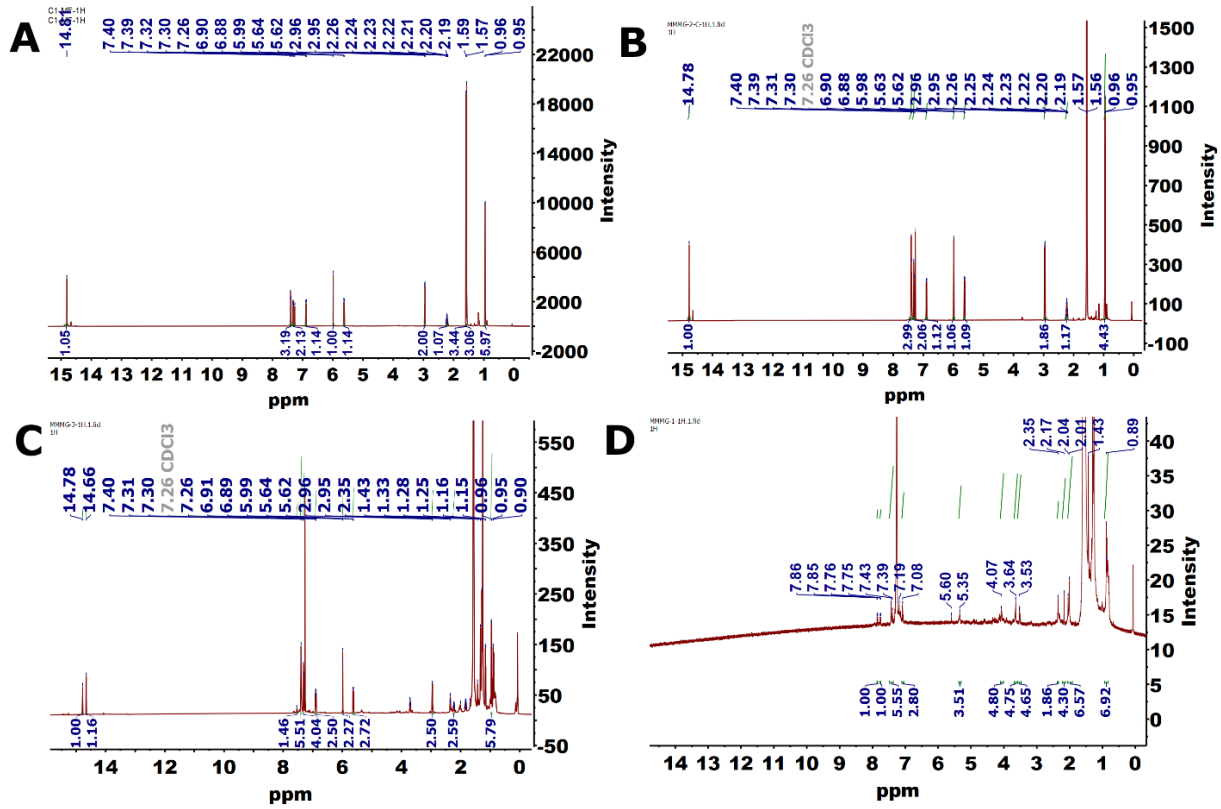

Figure 5.11: 1H NMR spectra of (A) Native MMG, (B) Crystalline fraction, (C) Compound A and (D) Compound B from non-crystalline fraction.

Compound A revealed the presence of two -OH groups (14.8 and 14.66 ppm) and presence of all the NMR signal peaks corresponding to native MMG (**Fig 5.11 C**). Also, the mass of compound B matched with native MMG. While compound B yielded very noisy data and low intensity NMR spectra, which turned to be inconclusive (**Fig 5.11 D**). But it did not show any peaks at 12-15 ppm range, which suggested absence of -OH groups due to quinoidal form component B.

In case of anthocyanins from red cabbage, at alkaline pH there co-existed two compounds, a carbinol pseudo base (colourless) from addition of -OH in the C ring and chalcone form with a bond cleaved at the 1-O bond in the C ring (yellow coloured) (Abedi-Firoozjah et al., 2022). This can be correlated to MMG at pH 13. Therefore, the presence of two -OH groups in compound A suggested the occurrence of hydrolysis. Compound A could correspond to the chalcone form of MMG. Since compound B was colourless and had higher mass than MMG, it could correspond to the carbinol pseudobase form of MMG. **Fig 5.12** depicts the schematic representation of the possible chemical reaction of MMG at alkaline pH.

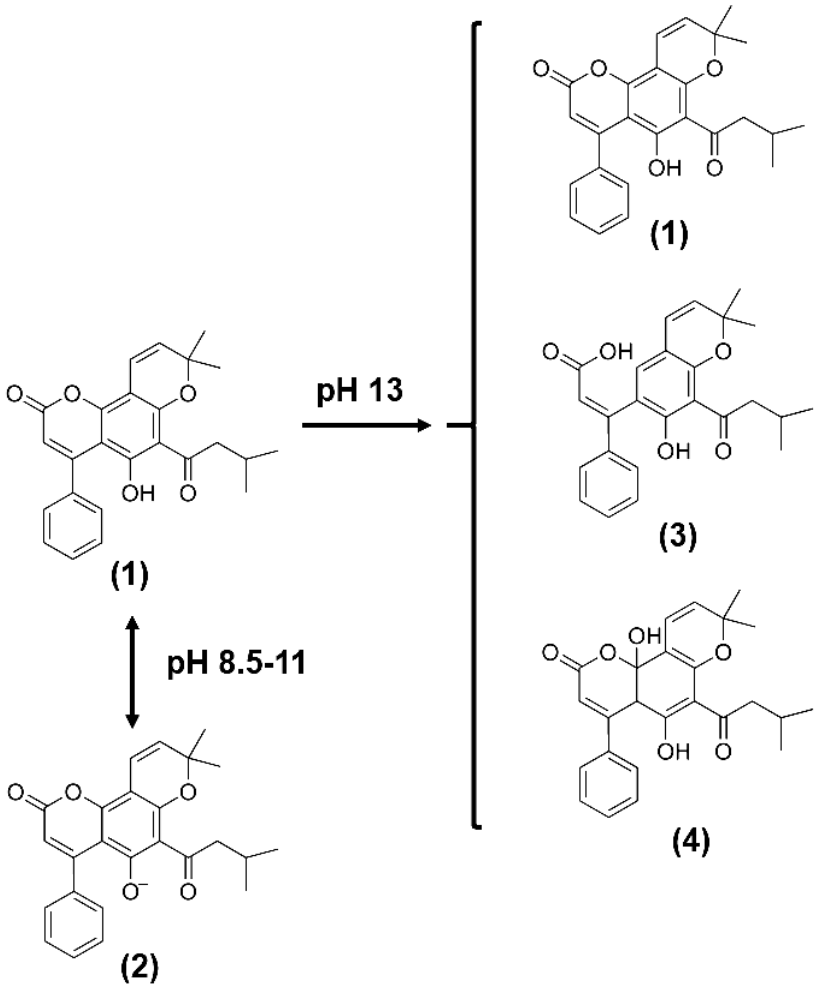

Figure 5.12: Schematic diagram of the possible chemical reaction of MMG at alkaline pH; (1) Native MMG and crystalline fraction in pH 13 (2) ionic MMG, (3) Chalcone form (Compound A) and (4) Carbinol pseudobase form (Compound B). [Unmodified MMG (interpreted through HPLC, LC-MS, NMR); Carbinol pseudobase form or Compound B (interpreted through physical properties like compound colour, HPLC, LC-MS) and Chalcone form or Compound A (interpreted through HPLC, NMR, LC-MS)].

5.4. Conclusion

Absorption spectroscopic properties of MMG were investigated at different pH conditions in various solvent systems. MMG was insoluble in acidic and neutral pH and displayed increase in solubility at alkaline condition with rise in pH accompanied by bathochromic shift in the absorption spectra. Upon investigating MMG in surfactant micelle systems at different pH, the solubility was improved at all the pH conditions. In case of CTAB (5 mM), MMG displayed distinctive spectral transitions at alkaline pH compared to acidic pH, corresponding to the phenoxide form of MMG. When comparing CTAB and buffer systems, CTAB provides a relatively protective environment for MMG at alkaline conditions, except at pH 11 and 12. MMG in pH 13 revealed a different absorption spectrum to that of native MMG, which was found to be irreversible. Upon characterization using HPLC, LC-MS and NMR, it was revealed that MMG in pH 13 exists as a mixture of 3 or more compounds with the abundant fraction to be unmodified MMG. The possible chemical modification was suggested to be the carbinol pseudobase and chalcone forms of MMG.

Chapter 6

Investigating the effect of salts on the spectroscopic properties of Mammeigin in micro-heterogenous systems.

6.1. Introduction

Surfactants, polymers and interfaces are few of the most explored systems that exhibit Hofmeister effect (Lo Nostro and Ninham, 2012). Hofmeister effect refers to the influence of different ions on the micellar properties of amphiphiles like cmc, micelle shape, size and interfacial behaviour (Hooshyar and Sadeghi, 2015). They occur in bulk solutions as well at interfaces. The interfacial water is an intrinsic part of aggregate structure. The presence of salts perturbs the hydration layers strongly at the aggregate water interfaces and involves ion-pairs depending on the type of electrolyte (Lo Nostro and Ninham, 2012). Depending on the influence of ions on the water structure, they are classified as kosmotropes and chaotropes (**Fig 6.1**). Kosmotropes refers to small ions with high charge density, large hydration shell and thus promote water structures. While chaotropes are larger ions with larger polarizability, low charge density and thin hydration shell are known to break water structures (Abezgauz et al., 2010). According to the concept of "Matching water affinities", kosmotropes have stronger ion binding to another kosmotrope, as with chaotropes with other chaotrope (Moreira and Firoozabadi, 2010).

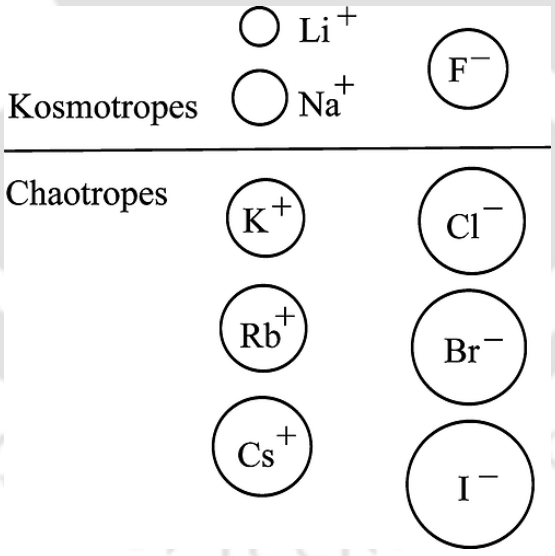

Figure 6.1: Examples of kosmotropes and chaotropes of alkali and halogen ions. The ions are drawn to scale of their bare radii (Adapted from Moreira and Firoozabadi, 2010)

The head group of the surfactant plays a pivotal role in surface chemistry of surfactants (Kumar et al., 2012). In charged surfactants, the presence of co-ions influences the electrostatic repulsion, hydration, head-group size through various means (Abezgauz et al., 2010).

The counterions either bind to the micelle surface or gets distributed in the diffuse layer. The ions of opposite charges to the head-groups gets intercalated among the surfactant heads in the stern layer and the excess ions are distributed in the diffuse region, which lies beyond the steric exclusion of the stern layer (Moreira and Firoozabadi, 2010) (**Fig. 6.2**).

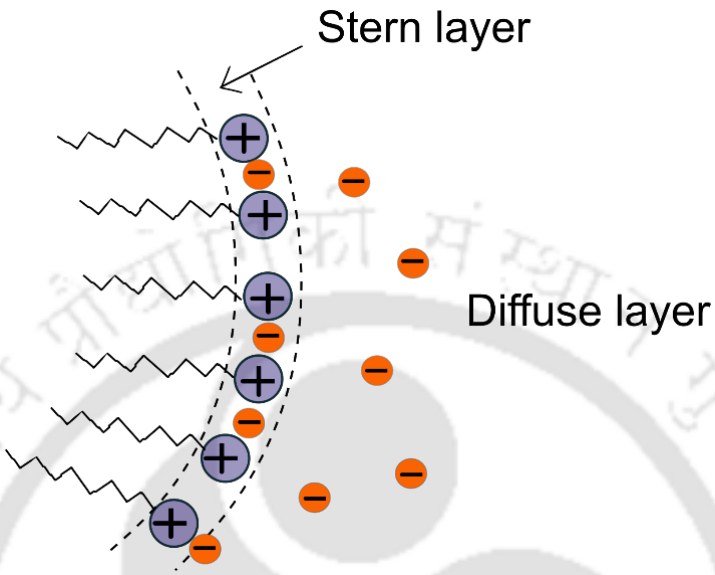

Figure 6.2: Schematic representation of micelle interface region containing stern and diffuse layers. Blue head groups and the tail represent surfactant molecule and orange circles represents electrolyte ion of opposite charge to the surfactant head-group (modified and redrawn from Moreira and Firoozabadi, 2010).

The nature of ion paring in the stern layer depends on the mutual geometry of the ions involved and the solvent molecules. Based on this, there are three types of ion-pairing: contact ion pairs (no solvent between the ions in contact); solvent-shared ion pair (ions separated by one layer of solvent molecule) and solvent-separated ion pair (further dissociation of the ions by solvation shells) (Moreira and Firoozabadi, 2010).

In this chapter, the effect of cations and anions of group 1 and group 17 elements respectively, on the spectroscopic properties of MMG in different surfactant micelle systems was investigated. Further exploration on the effect of fluoride and CTAB on absorption spectra of MMG was carried out. The influence of interfering ions on the fluoride effect on MMG is also discussed.

6.2. Materials and Methods:

6.2.1. Investigation on the effect of specific-ions on MMG spectra in different surfactants

Surfactant micelle solution of SDS (20 mM), CTAB (5 mM) and T20 (0.5 mM) were prepared in water. For investigating specific-ion effect, chloride salts of group 1 cations and sodium salts of group 17 anions i.e., LiCl, NaCl, KCl, NaF, NaBr and NaI were added in the concentration of 200 mM. MMG from ethanol stock was added in the concentration of 15 μM with final ethanol concentration of 1% (v/v). The samples were vortexed and incubated for 1hr and absorption spectra were collected in the range of 220-600 nm.

6.2.2. Sensitivity of MMG to fluoride in other solvent systems

To determine the sensitivity of MMG in CTAB solution to sodium fluoride, different concentrations of fluoride (0.024 mM (concentration limit in drinking water), 0.24 mM, 1.1 mM, 2.4 mM) were investigated. Apart from aqueous CTAB (5 mM), other solvent systems like CTAB (5 mM) with 10 mM NaCl, ethanol in water (1:1) and acetonitrile in water (1:1) were also explored. Absorption spectra were collected in the range 220-600 nm and absorbance at 442 nm was recorded.

6.2.3. Effect of CTAB concentration in fluoride sensing

To further study the sensitivity to fluoride, MMG (15 μM) was added to different concentration of CTAB (0.6 mM, 1 mM, 5 mM and 15 mM) in the presence of 10 mM NaCl. The samples were incubated for 1 hr with and without the addition of NaF (50 mM). The absorption spectra were collected.

6.2.4. MMG in CTAB with high concentrations of fluoride

MMG was added with high concentrations of NaF (0.024 mM-200 mM) in 1 mM CTAB solution in the presence of 10 mM NaCl. Absorption spectra were collected in the range 220-600 nm. Absorbance at 254 nm, 287 nm, 374 nm and 442 nm were noted for every spectra. The ratio of absorbance $A_{287nm}/A_{254\ nm}$ and $A_{442nm}/A_{374\ nm}$ were determined and plotted against the concentration of NaF added.

6.2.5. Effect of other interfering ions

To study the effect of interfering ions, sodium and chloride salts of common ions present in drinking water were chosen. They were added to solution containing MMG in 1 mM aq. CTAB+10 mM NaCl and sodium fluoride (0, 1.1, 25 and 200 mM) at the upper limit concentration found in the drinking water, according to World Health Organization (WHO) standards (**Table 6.1**) . Absorption spectra were collected and $A_{442nm}/A_{374\ nm}$ was calculated.

Table 6.1: Upper limit concentration of ions (as sodium and chloride salts) in drinking water (Kumar and Puri, 2012)

Salts	Concentration (mg/L)
$CaCl_2$	75
$MgCl_2$	50
$FeCl_3$	0.1
$CuCl_2$	1
$ZnCl_2$	5
$MnCl_2$	0.5
$AlCl_3$	0.1
$NaNO_3$	100
$NaSO_4$	250

6.3. Results and Discussion:

6.3.1. Investigation on the effect of Specific-Ions on MMG spectra in different surfactants

When ions of different charges and sizes were added to MMG in surfactant solutions, it resulted in a range of reactions as tabulated (**Table 6.2**).

In case of cations (**Fig. 6.3 A, B, C**), LiCl did not have any effect in the presence of SDS and T20, while it resulted in slight increase in absorption in case of CTAB. NaCl resulted in slightly higher absorption in case of CTAB. While, KCl resulted in precipitation of samples in SDS alone. These results are attributed to ion-pairing affinities of salt with ionic surfactants (Gregory et al., 2022; Moreira and Firoozabadi, 2010). Since Li^+ is the smallest

ion, it does not form stronger ion-pairs which resulted in no significant effect. While K^+ formed stronger and insoluble ion-pairs with negatively charged SDS, corresponding to its high polarizability and thin hydration shell. Na^+ has intermediate size, which resulted in absorption rise slightly more prominent in CTAB.

Table 6.2: Specific-ion effects of different salts (200 mM) on MMG (15 µM) in surfactant systems. The arrow marks indicate increase or decrease in the absorption (Abs.), ppt refers to precipitation.

Salt	SDS (20 mM)	CTAB (5 mM)	T20 (0.5 mM)
LiCl	No effect	↑Abs.	No effect
NaCl	No effect	↑Abs.	No effect
KCl	ppt	No effect	No effect
NaF	No effect	Red-Shift	↓Abs., ppt
NaBr	↑↑Abs.	↑Abs.	↑↑Abs.
NaI	No effect	Ppt	No effect

On the other hand in case of anions (**Fig 6.3 D, E, F**), addition of NaF resulted in red shift of absorption spectra in case of CTAB alone, similar to the alkaline pH conditions. While in T20, it precipitated the samples. NaBr resulted in noticeably higher absorption, especially in SDS and T20. And NaI resulted in precipitation in case CTAB. F^- ion is oppositely charged to CTAB, but not big in size to form strong ion-pair. F^- is classified as a hard base (Gregory et al., 2022), due to which the presence of fluoride could have resulted in deionization of MMG in CTAB solution. Cl^- has intermediate size which resulted in slightly more absorption in CTAB, compared to other surfactants. Br^- is reported to have similar size to that of trimethylammonium group of CTAB resulting in stronger ion-pairing. This could have led to higher absorption (Moreira and Firoozabadi, 2010). I^- being the large-sized chaotrope, resulted in insoluble ion-pairs with CTAB and displayed no effect on other surfactants.

Since the presence of NaF in CTAB resulted in a unique observation compared to other ions, it was investigated further.

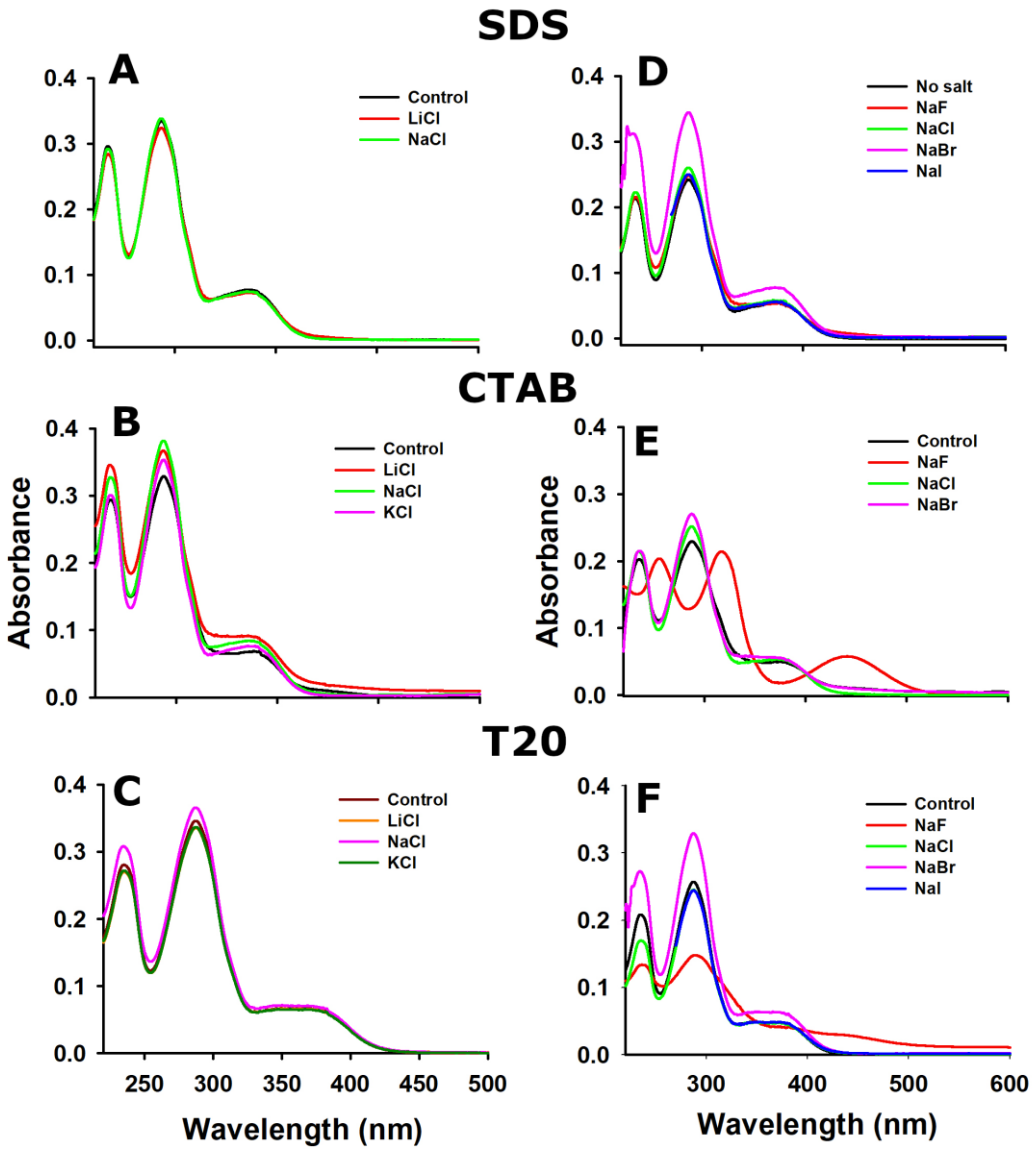

Figure 6.3: Absorption of MMG (15 µM) in SDS (20 mM), CTAB (5 mM) and T20 (0.5 mM) with 200 mM of (**A, B, C**) LiCl, NaCl, KCl, (**D, E, F**) NaF, NaCl, NaBr, NaI.

6.3.2. Sensitivity of MMG to fluoride in other solvent systems

Apart from aq. CTAB (5 mM), other solvent systems like organic-water mixtures, CTAB with and without salt additives were investigated. Various concentrations of NaF were added with the lowest concentration being 0.024 mM, which is the limit for drinking water according to WHO (Kumar and Puri, 2012). As a reference, 200 mM NaF was also tested in these solvents systems. The occurrence of red-shift was monitored through relative absorbance at 442 nm. In aqueous- organic solvent systems i.e., 1:1 ethanol in water and 1:1 acetonitrile in water, there was no red-shift in the spectra observed at lower concentrations (**Fig 6.4**). While at 200 mM

NaF, it resulted in precipitation of samples. This suggested that there was no direct binding of fluoride to MMG molecule proving that CTAB had a role to play.

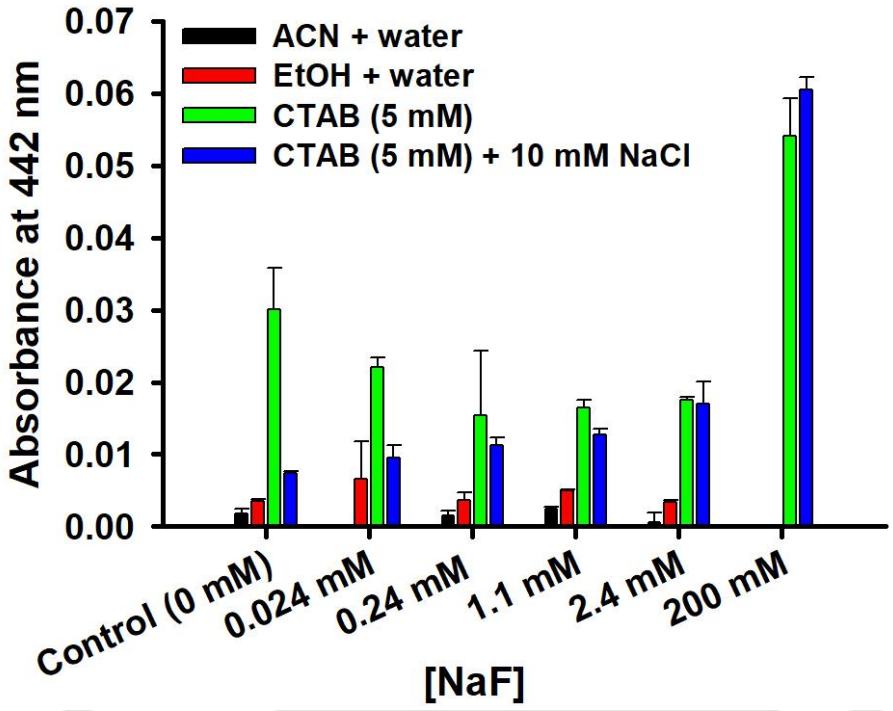

Figure 6.4: Absorbance of MMG (15 µM) at 442 nm in different solvent systems in the presence of different concentrations of NaF

Unlike the case of MMG, turmeric and curcumin amongst plant phenols displayed sensitivity to fluoride in the range of 1-100 ppm in aqueous-organic solvent systems (Bhat et al., 2016; Venkataraj et al., 2017). It was as a result of direct interaction with fluoride ion. As discussed earlier, CTAB itself provides a mild alkaline environment which resulted in occurrence of 442 nm peak. But its occurrence and intensity was not found to be consistent. This caused irregular values in the 442 nm absorbance, which did not follow any particular trend with fluoride concentration (**Fig 6.4**). To overcome this, small amounts of NaCl (10 mM) was added to neutralize the CTAB charges but not strong enough to hinder the van der Waals forces for interaction (Ivanov et al., 2011). With this solvent system, consistent increase in the 442 nm absorbance was observed with increase in fluoride concentration and this medium was used for further experiments. Although there was increase in the absorbance with fluoride concentration, the difference in the absorbance was not significant enough to be used to detect lower levels of fluoride and therefore its related applications.

6.3.3. Effect of CTAB concentration on the fluoride sensitivity

To study the effect of CTAB on the spectral shift of MMG, different concentrations of CTAB were added. In the absorption spectra, there was increase and decrease of absorption peaks at 442 nm and 374 nm respectively, when high concentration of fluoride (50 mM) was added (**Fig 6.5 A**). Since the difference in the absorbances was not significant enough, the ratio of these peaks were calculated to monitor the changes in the absorption spectra. The ratio decreased with increasing concentrations of CTAB (**Fig 6.5 B**). At higher CTAB concentrations, the micelles could have also undergone change in shape from spherical to rod-like, in the presence of salt (Chaudhuri et al., 2011; Sarkar and Chattopadhyay, 2016). Usually such transitions happens at high salt concentrations. Since the CTAB concentration is itself high, the shape transition must have occurred at this condition. Such structures are tightly packed resulting in more internalization of MMG into the core, leading to absorption increase and least permeable to outside solution (Chaudhuri et al., 2011). Amongst the low CTAB concentrations, the ratio was higher in 1 mM CTAB compared to 0.6 mM CTAB, which was optimized for further investigation.

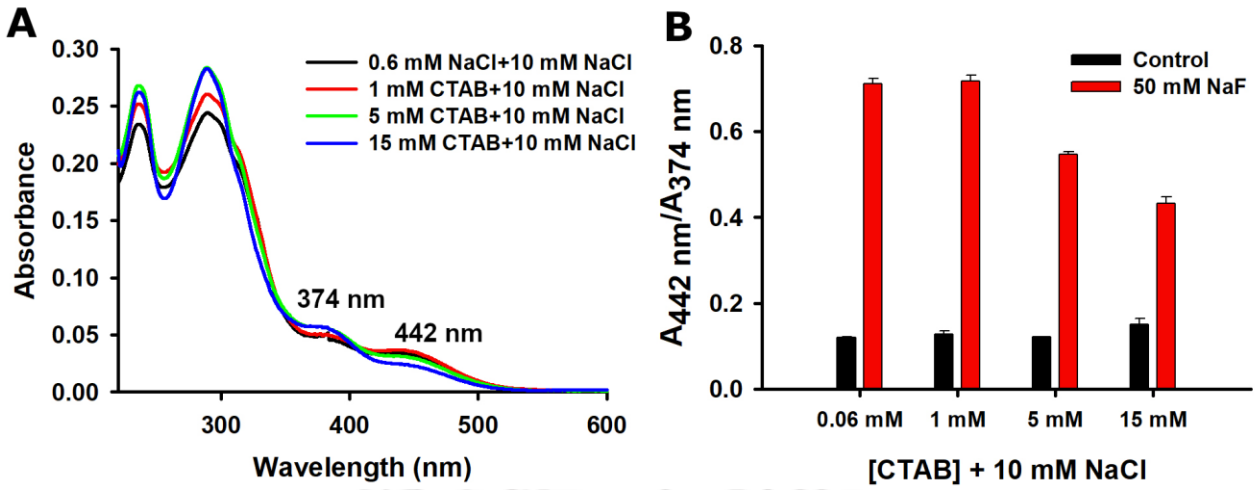

Figure 6.5: (A) Absorption spectra and (B) $A_{442nm}/A_{374\ nm}$ of MMG (15 µM) in different CTAB concentration with 50 mM NaF.

6.3.4. MMG in CTAB with higher concentrations of fluoride

Since MMG was not found to be sensitive to lower concentrations of NaF, higher amounts (0.024-200 mM) were added. With increasing fluoride concentrations, there was gradual spectral shift observed from wavelengths 234 nm → 256 nm, 287 nm → 317 nm, 374 nm → 442 nm (**Fig 6.6 A**). This shift in spectra could be due to the basic nature of fluoride ions

resulting in ionization of MMG in the presence of CTAB. Since fluoride ion has smaller ionic size, it does not involve in stronger ion-pairing with CTAB molecules (Gregory et al., 2022; Moreira and Firoozabadi, 2010). Thus the role of CTAB could be majorly for solubilization of MMG.

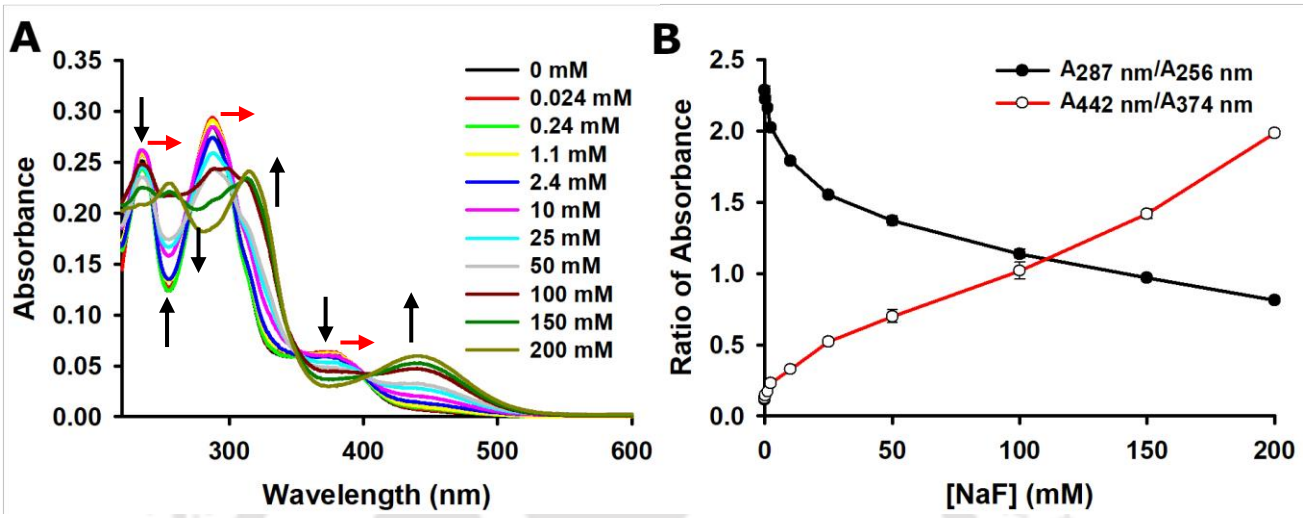

Figure 6.6: (A) Absorption spectra and (B) Absorbance ratios of MMG (15 μM) in different concentrations of NaF. Black arrow marks indicates increase or decrease in the absorption and red arrow marks indicates shift in the spectral peaks.

Since fluoride is a hard base, it resulted in ionization of MMG. This resulted in mixture of both ionic and non-ionic MMG, whose proportion depended on the concentration of NaF. Since the absorption spectra were different for both the forms of MMG, the intersection of both the spectra resulted in isosbestic points at 243 nm, 268 nm, 303 nm, 350 nm, 400 nm. The increase in absorption at one λ_{max} will result in the decrease of the other about the isosbestic points. Therefore, the concentration of NaF was directly correlated to ratio of the absorbances $A_{287nm}/A_{254\ nm}$ and $A_{442nm}/A_{374\ nm}$. **Fig 6.6 B** represents the plot where $A_{287nm}/A_{254\ nm}$ resulted in a decreasing trend while $A_{442nm}/A_{374\ nm}$ lead to increasing trend. Thus it can be concluded that only at higher concentrations of NaF, the effects in the absorption spectra was significant. Therefore, MMG has poor sensitivity in detecting fluoride at lower concentrations.

6.3.5. Effect of other interfering ions

The influence of some interfering ions on the absorption spectral transitions in the presence of NaF was investigated. At the upper limit concentrations of ions in the drinking water, MMG in 1 mM aq. CTAB+10 mM NaCl was added along with NaF at 0 mM, 1.1 mm, 25 mM and

200 mM concentrations. The ratio $A_{442nm}/A_{374\ nm}$ was estimated from the absorption spectra. It was observed that there was no major influence of interfering ions at lower concentrations of NaF (1.1mM and 25 mM). However at 200 mm NaF, $MgCl_2$, $FeCl_3$ and $CuCl_2$ resulted in lowering of $A_{442nm}/A_{374\ nm}$ (**Fig 6.7 A**). Thus, at lower concentrations of NaF taken, there was no influence of interfering ions.

The effect of high concentrations of these interfering ions were also tested (data not shown). The salts except $CaCl_2$, did not display any spectral shifts. The presence of $CaCl_2$ resulted in similar red-shifted absorption spectra (**Fig 6.7 B**). Absorption spectra could not be obtained for $ZnCl_2$, $FeCl_3$ and Na_2SO_4 at high concentrations, either due precipitation in case of $ZnCl_2$ and Na_2SO_4 or overlapping of intrinsic absorbance of $FeCl_3$ and MMG. This investigation can be carried out as future work.

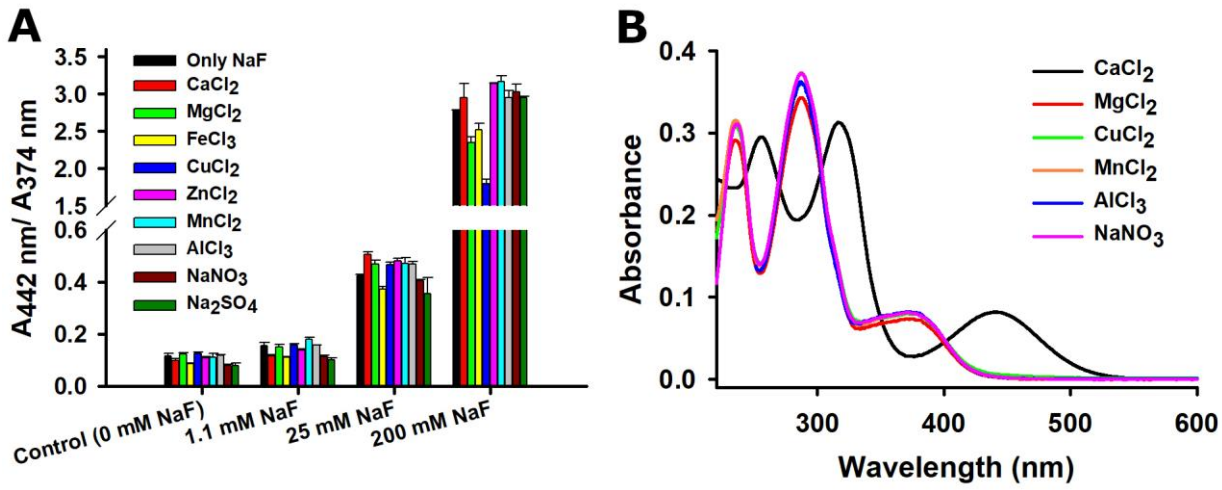

Figure 6.6: (A) Selectivity of MMG to fluoride concentrations (0 mM, 1.1 mM, 25 mM, 200 mM) in the presence of other ions (as Na and Cl salts) found in drinking water. (B) Absorption spectra of MMG in CTAB (1 mM)+10 mM NaCl, mixed with the ions under investigation at 200 mM concentration.

6.4. Conclusions

MMG in different surfactant micelle solutions displayed range of effects due to Hofmeister series. Absorption spectra of MMG in CTAB solution in the presence of NaF resulted in bathochromic shift in the spectra. In the presence of other MMG soluble solvents like aqueous-organic systems, MMG did not undergo such red-shift in spectra at lower concentrations of fluoride, suggesting non-existence of direct binding of MMG with fluoride ion(s). The sensitivity to fluoride was higher in lower concentrations of CTAB, which in the presence of lower NaCl was optimized as the solvent system. Addition of higher NaF

concentrations resulted in gradual shift in the absorption spectra in a NaF concentration-dependant manner. There was no significant influence of interfering ions at relatively lower concentrations of NaF. MMG can serve as an inexpensive spectroscopic tool to detect fluoride in the concentration range of 2.4-200 mM.

Chapter 7

Thesis Summary

THESIS SUMMARY

Mammeigin was extracted, isolated and identified from the seed oil of *Mesua ferrea*. With the process optimized in the current work, an overall yield of 0.64 % w/w of seeds and purity of 99% was obtained, which was found to be higher than the previous reports.

Absorption spectra of MMG displayed three absorption bands in organic solvents with λ_{max} at 234 nm, 286 nm and 339-369 nm. However, major spectral shifts were not observed with different polarity of the solvents. MMG is water insoluble and required ≥ 40 % v/v ethanol in water for solubilization. Since ethanol concentrations of 1-5 % v/v is the accepted range for biological assays, self-assemblies like surfactants were explored. Surfactants of different charges i.e., SDS, CTAB and T20 were investigated and aqueous solubility of MMG was enhanced in all the three surfactants. MMG in surfactants around the cmc resulted in dip in the absorbance due to precipitation in SDS and possibly lower molar absorption coefficient in CTAB. The stability at these concentrations was improved in the presence of 200 mM NaCl. While in T20, MMG precipitated below the cmc and also instability of MMG in T20 micelles over time were observed.

Similarly, the surfactant environment was attempted to be recreated in HEWL aggregates. MMG showed interactions with HEWL aggregates in pH 2 at initial stages of aggregation. But these interactions were weakened at later stages of aggregation and fibrillation, due to low permeability into the aggregates resulting in instability. While, MMG in HEWL aggregates at pH 5 did not display any interactions. Furthermore from the investigation of MMG-pHEWL interactions at pH 9, it was inferred that partial unfolding of HEWL with exposed hydrophobic regions was essential for MMG to bind to the aggregates. The environment of MMG in HEWL aggregates was comparable to surfactant micelles, but found to be more heterogenous in HEWL aggregates.

Absorption spectral properties of MMG were investigated at different pH conditions in various solvent systems. It was observed that MMG was insoluble in acidic and neutral pH buffers. While at alkaline pH (9.5-12), the solubility of ionic MMG increased in buffers in a pH dependent manner along with bathochromic spectral shift ($\Delta\lambda$=22-68 nm). In the presence of surfactants, the solubility was achieved at all the pH conditions while a prominent and stable red-shift in the spectra in CTAB micelles was observed, resulting in bright yellow coloration at pH ≥ 7.5. Moreover, MMG was unstable in buffers and the stability was

improved in CTAB micelles at pH 2-10.5 and 13. However, MMG in pH 13 yielded a different and irreversible absorption spectral change (λ_{max}=277 nm and 336 nm). Through further characterization, the structural transformations are suggested to be carbinol pseudobase and chalcone forms of MMG.

Lastly the specific ion effect of LiCl, NaCl, KCl, NaF, NaBr and NaI at 200 mM concentrations on the absorption properties of MMG was investigated. Out of these ions, MMG in CTAB with NaF displayed a red shift in the spectra, similar to that observed in alkaline pH. This effect was only observed in case of CTAB but not in other solvent systems, suggesting no direct interactions of MMG with fluoride and specific involvement of CTAB. The sensitivity to fluoride detection was found to be more at lower CTAB concentrations in the presence of 10 mM NaCl. At this solvent condition, MMG displayed noticeable spectral changes only at high concentrations of NaF (2.4-200 mM). The presence of interfering ions in drinking water levels were found to not have any significant interference with the spectral shifts due to NaF.

Therefore, the current thesis work provides insights for developing an efficient drug-carrier systems for targeted drug delivery. MMG can also be utilized for applications like pH and fluoride ion sensing.

Appendix

Device developed for evaporation and recovery of organic solvents using simple labwares

A.1. Introduction

Various experiments like chromatographic separations, multistep synthesis, crude extracts, and distillates preparation requires frequent use of solvent evaporation and recovery in chemistry and certain biological laboratories. Without a proper device or equipment, it would be a challenging task to carry out on a large scale. Therefore, several methods and techniques have been developed like open dish evaporation, nitrogen blowing, distillation, Kuderna-Danish (K-D) evaporative concentrator, centrifugal concentration, vortex evaporation, and blow-down evaporation (Abeysena, 2013; Erickson et al., 1981; Norris, 1924). An American biochemist Craig, L. C. in (1950) devised a rapid and efficient setup, which is now known as a rotary evaporator (Craig et al., 1950; Jensen, 2008). In recent times, many improvisations have been made on the model, due to which it has dominated over the other techniques. Recently advanced updating of the device came with a high expense due to which under-funded laboratories, universities, and secondary schools cannot easily afford it.

Since this is an essential and most frequently required instrument, there has been reports on alternative setups. Radin, (1956) proposed a technique wherein the samples were taken in test tubes or flasks and subjected to heat, agitation, and vacuum, without the use of rotary seals. In the design by Kamphausen, (1962), the samples were subjected to combined action of suction and blowing for rapid evaporation. A cost-effective design assembly was suggested by Hoffman, (1976) consisting of commercially available motor, Teflon rod, condenser, receiver, and a vacuum source. Yet another design was proposed wherein the sample was allowed to fall over a heated coil as a slow stream (Rabman and Doulatabadi, 1984). Smaerd, (2013) constructed a modular rotary evaporator where the design implemented modular components, ease of construction and effectiveness.

The above methods were constructed with the use of sophisticated glassware, mechanical and electrical components. In the current work, a simple and cost-effective design was implemented to meet the same necessity. It requires only commonly available components and fundamental skills to construct this device. It banks on three factors: heat supplied, surface area for solvent exposure, effective vapor removal by vacuum, and recovery of the condensed solvent. It is also demonstrated that the user can easily customized the present device to operate multiple samples simultaneously. ***This device was constructed as***

an alternative to rotary evaporator and utilized in the process of extraction, isolation and purification of MMG.

A.2. Materials and Methods

A.2.1. Materials needed

The apparatus was assembled using separating funnel(s) (Jain Scientific glasswares JSGW, India), two or more Erlenmeyer conical flasks (Borosil), two or more sidearm conical flasks (Borosil), unstirred heating/cooling water bath (Grant Instruments), plastic microtips (1 mL and 5 mL) (Tarsons), rubber corks (size 11) (JSGW) fitting to the conical flasks, 80 glass tubes of 7 mm outer diameter (Borosil), silicone tubes 7 and 8 mm outer diameter and 4-5 m length approximately (Sevitsil, India), parafilm, sandpaper, driller, T- joint or multi-joint connectors, diamond glass cutter, silicone sealant with a hot glue gun applicator, peristaltic pump for process optimization (Miclins India), ice bath in ice jacket/plastic tub and vacuum pump (KNF pumps).

A.2.2. Fabrication of parts

Certain parts needed to be altered and fabricated before setting up the device. Firstly, two sets of rubber corks were made i.e., one-way channel and two-way channel. The rubber corks (component A in **Fig A.1 A and B**) were drilled to create holes (7 mm diameter approximately) using driller (component B in **Fig A.1 A and B**).

For the two-way channel rubber corks (component D) (**Fig A.1 A)**, 1 mL plastic microtips (component C) were fixed into the holes tightly to create a channel. The joints between the hole and the microtip were hermitically sealed using silicone sealant through a hot glue gun applicator and secured with parafilm layers. The narrow end of the microtip was trimmed to ensure free flow of liquid. Similarly, for one-way channel corks (component D) **(Fig A.1 B)**, a single hole (7-8 mm diameter) was drilled (component B) and 5 mL microtip (component C) was fixed with the wider end of the microtip towards the narrow end of the rubber cork.

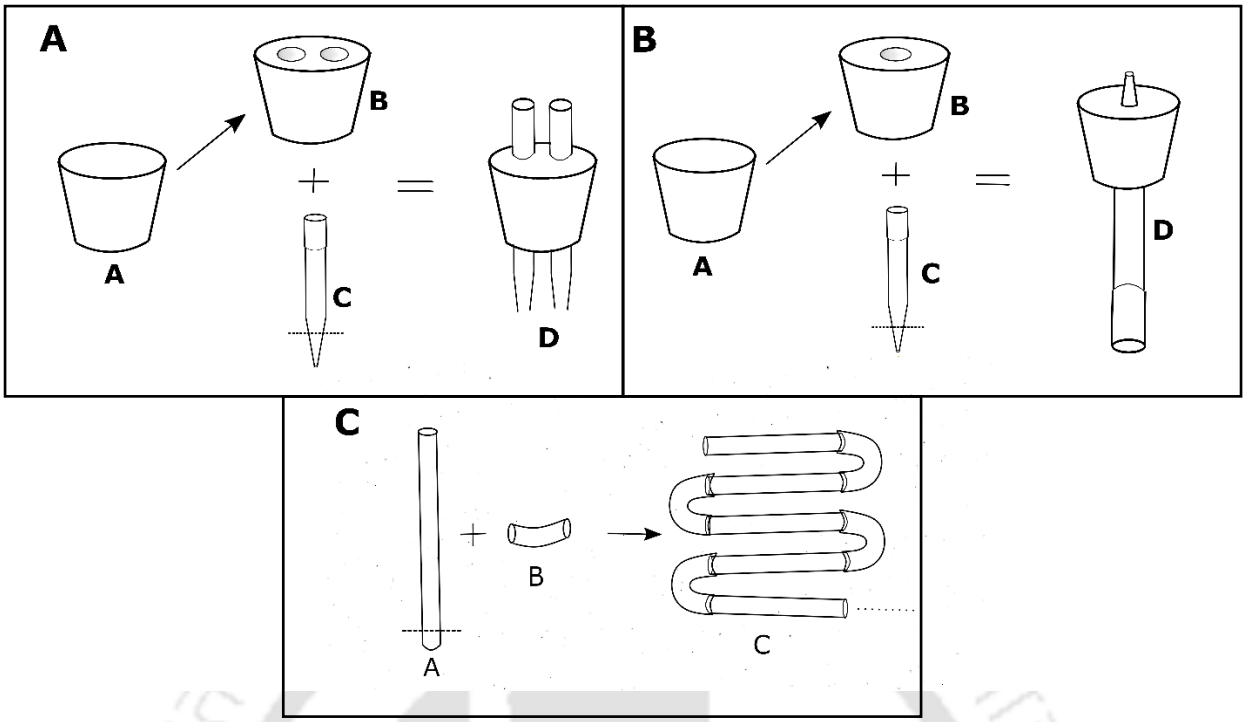

Figure A.1: Fabrication of (A) Two-way rubber cork, (B) One-way rubber cork and (C) glass condenser coils.

Lastly, glass coil was fabricated for condensation unit (**Fig A.1 C**). Around 80 glass tubes of size 7 x 127 mm (component A) were cut at the bottom with a glass cutter and the edges were evened out and polished with sand paper. The glass tubes were then connected to each other through short silicone tubes of outer diameter 7mm (component B) and the joints were sealed with the silicone sealant. For the current device, a total length of 9 meters coil was fabricated (component C).

A.2.3. Fractional factorial design

Performance of the device was assessed using 2_{V}^{5-1} fractional factorial design for enhancing recovery of condensed solvent and reducing the solvent retentate in the evaporation unit. Five parameters were investigated i.e., boiling point (A) of the solvent, the flow rate of sample into the evaporation flask from the dispenser (B), water bath temperature in evaporation unit (C), surface area of the conical flask base in the evaporation unit (D) and ice bath temperature in the condensation unit (E) (**Table A.1**).

Table A.1: Variables and levels under study for fractional factorial design

Factor code	Factors	Factor levels		
		-	0 (Center point)	+
A	Solvent	Acetone (bp = 56 ºC)	Chloroform (bp = 61.2 ºC)	Hexane (bp = 69 ºC)
B	Flow rate of solvent from dispenser (ml/min)	3.0 ± 0.5	5.0 ± 0.5	7.0 ± 0.5
C	Evaporation unit temperature (ºC)	60 ± 1	66 ± 1	72 ± 1
D	Base surface area of evaporation flask (cm^2)	28 (250 ml flask)	-	50 (500 ml flask)
E	Condensation unit temperature (ºC)	2 ± 2	7.5 ± 2	13 ± 2

The experiments were designed and analyzed using Minitab software 16.0. The response was modelled using the below regression **equation A.1**:

$$Y = b_0 + b_1 A + b_2 B + b_3 C + b_4 D + b_5 E + b_{12} A*B + b_{13} A*C + b_{14} A*D + b_{15} A*E + b_{23} B*C + b_{24} B*D + b_{25} B*E + b_{34} C*D + b_{35} C*E + b_{45} D*E + b_{1235} A*B*C*E \quad \ldots\ldots\ldots\ldots\ldots\ldots \text{(A.1)}$$

Where, Y is the response; b_0 is the model constant; b_1, b_2, b_3, b_4, b_5 are linear coefficients; b_{12}, b_{13},…..b_{1235} are cross product coefficients

A.2.4. Comparison with conventional design combinations

The current device was compared to conventional systems in terms of evaporation flux rate and recovery of solvents with regards to condensation coil length. The device incorporated a dispenser type system which was compared to bulk type system, commonly incorporated in conventional distillation units. Time taken for evaporation of different volumes of acetone i.e., 10.5 ml, 31.5 ml and 52.5 ml was recorded and divided by the surface area of the flask containing the solvent exposed to heat was estimated.

The relation of solvent recovery and the length of glass condenser coil was investigated. Solvent recovery was measured for different coil lengths i.e., 246.5 cm (I), 493

cm (II), 740 cm (III) and 986 cm (IV) at two different vacuum pressures, -300-350 mbar and -600-650 mbar.

A.3. Results and discussion

A.3.1. Construction of the apparatus

Figure A.2 A depicts the assembly of the device representing different components. A separating funnel (A) was taken as a sample dispenser and fitted at a particular height to a clamp stand using appropriate clamps. The separating funnel outlet was connected to the evaporation unit (D) using a silicone tube (C) such that the free-flowing of the sample was ensured. The sample flow rate was regulated by adjusting the separating funnel knob (B). For parameter optimization experiments, peristaltic pump was used for precise flow rate of the solvent.

The evaporation unit constituted of a conical flask (D) fitted with two-way channel rubber cork and placed in a heating water bath (G). One of the channels (E) was connected to the separating funnel and the other (F) to glass condenser coil using silicone tubes of appropriate lengths. Since the device is for organic solvents, it is preferable to use chemical-resistant rubber corks. In this device, aluminium foils were used to cover up the rubber cork at solvent-exposed regions.

The condensation unit comprised of the fabricated glass coil (H) arranged in an ice bath (I) in a plastic tub. The coil was wound in larger circles and placed in the tub such that there was no intertwining or tightening of silicone tubes joining the glass tubes. The volume of the ice bath was taken such that the coil was entirely submerged.

The recovery unit comprised of a sidearm conical flask (J) kept in the same ice bath (I). The flask was fixed with the one-way channel rubber cork. The inlet of the channel was connected to other end of the condensation coil (K), and the sidearm of the flask (M) was connected to vacuum pump (N). It is key to ensure that the longer end of the one-way channel (the fitted 5 ml microtip) (L) extends well into the flask to prevent loss of recovered solvent and to protect vacuum pump. Chemical-resistant vacuum pump was used in this device. After assembling the components, all the joints were hermitically sealed with silicone sealant and secured with parafilm wherever applicable.

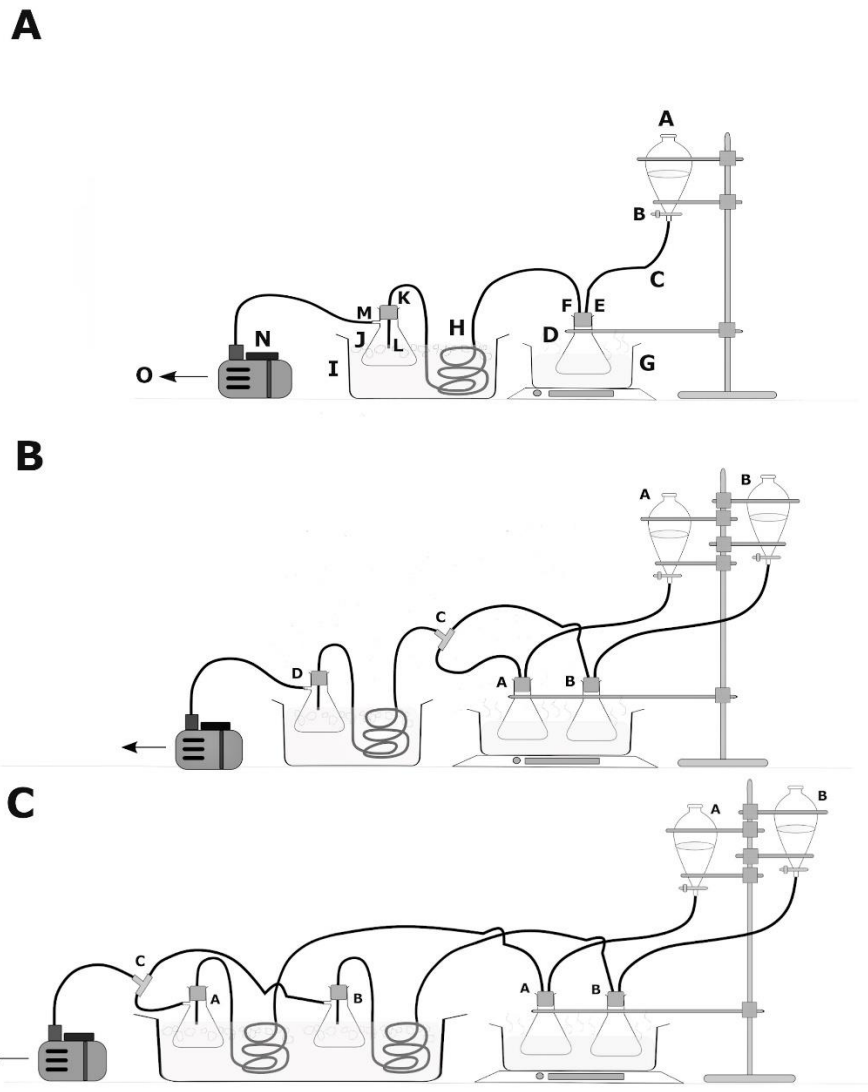

Figure A.2: (A) Depicts the assembly of the device with different components. A – Sample dispenser; B – separating funnel knob/flow rate controller; C - Silicone tubes connecting different units; D – Evaporation flask; E – channel connecting C and D; F – channel connecting D and condenser coil (H); G – Unstirred heating water bath arrangement; H – Glass condenser coil; I - Ice bath; J – Recovery flask; K – channel connecting H and J; L – Extension of microtip into J; M – side arm of J connected to vacuum pump (N); N – Vacuum pump; O – Direction of vacuum pressure applied.

(B) Depicts the assembly of the components for operating multiple samples with same solvent system. Samples A and B were connected to separate evaporation flasks (A and B) which were connected to common channel through T-joint connector (C) and recovered in a single unit (D).

(C) Depicts the assembly of the components for operating multiple samples with different solvent systems. Samples A and B were connected independently up to recovery unit and connected to a common vacuum source through T-joint connector (C).

After construction of the device, the sample was taken in the separating flask. It is advisable to create vacuum in the system with the condenser glass coil at room temperature, prior to running the device. This prevented condensation of moisture inside the coils when they placed in ice bath and avoided moisture contamination in the recovered solvents. Later, the sample was dispensed into the evaporation flask as a slow stream. The solvent from the evaporation flask vaporized and the vapours entered the glass coils in the ice bath while the solutes got concentrated in the evaporation flask. The solvent condensed and got collected in the recovery unit. The application of vacuum allowed evaporation to take place at reduced pressure. The major benefit of this device is customizability, allowing the user to run multiple samples, either containing the same or different solvents.

Fig A.2 B depicts an example of the setup for the case of two samples containing same solvent base. The samples (A and B) were taken in two different separating funnels and connected as separate lines to the evaporation unit, as mentioned previously. In this case, the outlet from each extraction unit was channelized to a single condensation tube using a T-joint connector (C) or multi-joint connector, depending on the number of samples. The rest of the system was the same as mentioned above. The solvent from the samples was collected in a common recovery unit (D).

In the case of employing more than one sample containing different solvent bases and each of them needs to be recovered separately, each sample from the separating funnel up to the recovery unit (A and B), was set up as independent lines. The difference was that the outlet tube from each recovery flask were connected to a single tube leading to the vacuum source using T- joint (C) or multi-joint connectors (**Fig A.2 C** depicting two samples).

Fig A.3 Depicts the basic setup of the device for one sample representing different components.

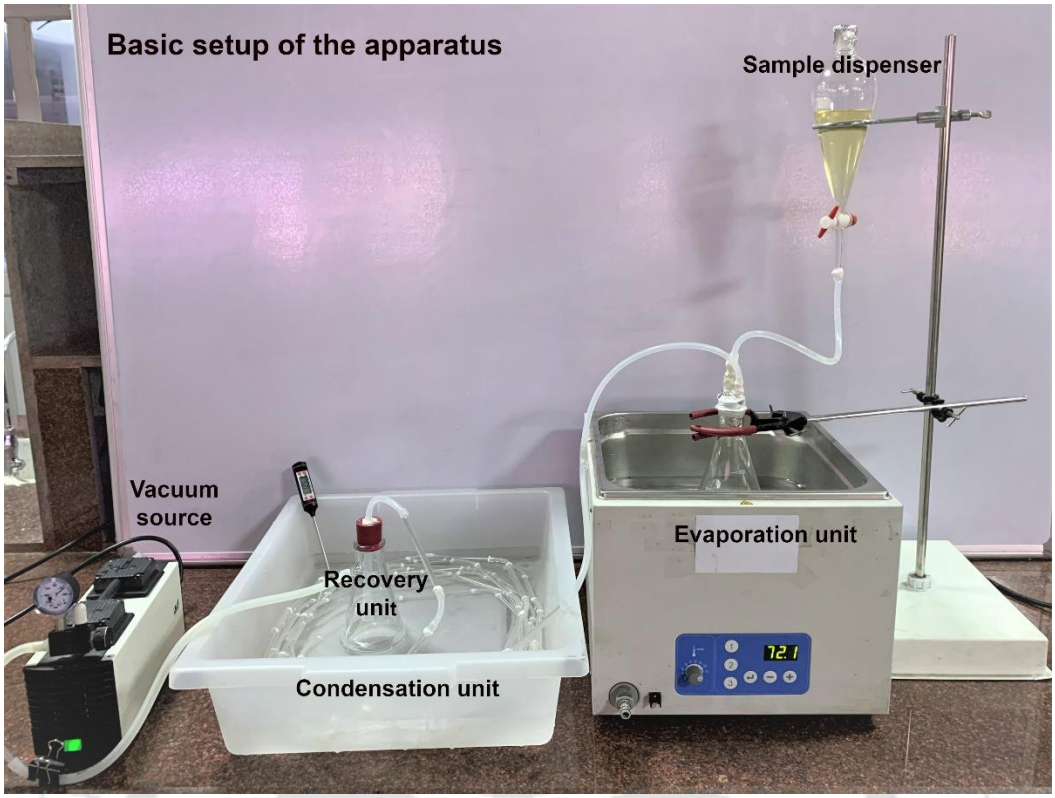

Figure A.3: Basic setup of the apparatus representing all the components

A.3.2. Fractional factorial analysis

The performance of the system was demonstrated with the help of 2_V^{5-1} fractional factorial screening experiment. The following example is not to be considered as being exhaustive or exclusive to the scope of this device.

There were five factors investigated which were likely to affect the efficiency of the device i.e., nature of the solvent in terms of its boiling point (A), the flow rate of sample from dispenser to the evaporation flask (B), temperature of the water bath in evaporation unit (C), surface area of the conical flask base in the evaporation unit (D) and temperature of the ice bath in the condensation unit (E). Here, the efficiency (in %) was the amount of solvent recovered in the recovery unit to the amount of solvent input in the evaporation flask for a period of time. Also, the amount of solvent retained in the evaporation flask at the end of the run was measured as retentate. The screening experiment was used to determine the main effects and interactions of the factors involved in the evaporation and recovery processes.

Table A.2 gives the design matrix for 2_V^{5-1} fractional factorial design, the observed and predicted responses. A regression analysis was executed to evaluate the relation between

the factors and responses. The adequacy of the regression model obtained was examined based on the analysis of variance (ANOVA) and the residual plot.

The models fitted the data well and the residual values were small and unbiased. **Figure A.4 A and B** depicts the residual plots for recovery and retentate, which shows that the residual values were distributed uniformly.

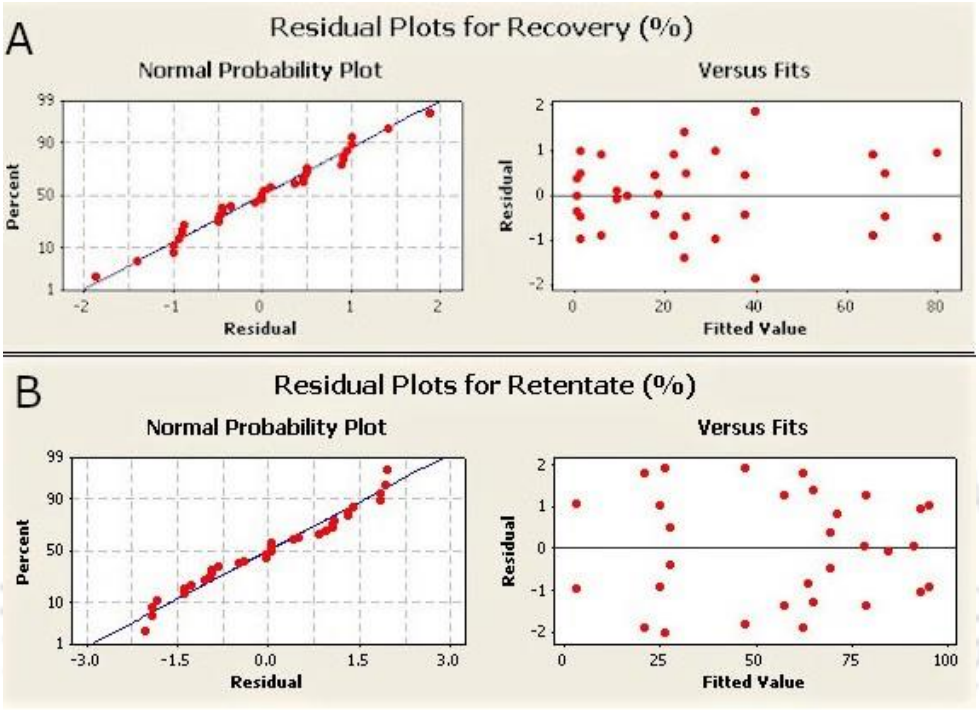

Figure A.4: Residual plots for recovery (A) and retentate (B) responses.

Table A.2: Design matrix and results of fractional factorial design analysis.

Factors								
Solvent	Flow rate of the sample from the dispenser (ml/min)	Evaporation temperature (°C)	Base surface area of the evaporation unit (cm^2)	Condensation temperature (°C)				
A	B	C	D	E	Recovery (%)	Predicted Recovery	Retentate (%)	Predicted Retentate
-1	3	60	28	13	25.47 ± 2	24.0555	62.26 ± 2.67	62.31676
1	3	60	28	2	1.1 ± 0.71	1.098894	93 ± 1.41	93.05261
-1	7	60	28	2	17.55 ± 0.64	17.55065	78.76 ± 1.91	78.81049
1	7	60	28	13	0.36 ± 0.5	0.357156	84.19	84.24428
-1	3	72	28	2	68.4 ± 0.67	68.39512	20.75 ± 2.67	20.80733
1	3	72	28	13	31 ± 1.41	30.99889	26 ± 2.83	26.05261
-1	7	72	28	13	37. 35 ± 0.64	37.35263	57.16 ± 1.91	57.20833
1	7	72	28	2	5.37 ± 1.27	5.37283	69.41 ± 0.63	69.46596
-1	3	60	50	2	39.62 ± 2.67	39.62375	47.17 ± 2.67	47.1172
1	3	60	50	13	1 ± 1.41	1.001106	95 ± 1.41	94.94739
-1	7	60	50	13	21.6 ± 1.27	21.60327	78.44	78.39023
1	7	60	50	2	0	0.001106	91.36	91.30431
-1	3	72	50	13	80.19 ± 1.33	80.18876	3.12 ± 1.45	3.072388
1	3	72	50	2	24.5 ± 0.71	24.50111	25 ± 1.41	24.94739
-1	7	72	50	2	65.71 ± 1.27	65.70768	27.45 ± 0.64	27.40013
1	7	72	50	13	8.87 ± 0.13	8.868101	64.94 ± 1.9	64.88245
0	5	66	28	7.5	11.26687	11.28457	72.05555	71.21375
0	5	66	50	7.5	18.34141	18.32371	62.88484	63.72664

The adequacies of the regression models (**Equations A.2 and A.3**) were analyzed statistically by Analysis of Variance (ANOVA) and summarized in **Table A.3 and A.4**.

Equation A.2.

The regression model for the recovery is:

$$\text{Recovery (\%)} = 26.7 - 17.6\,A - 7.07\,B + 13.51\,C + 3.54\,D - 1.11\,E + 1.69\,A*B - 5.1\,A*C - 3.95\,A*D + 2.4\,A*E - 3.78\,B*C + 0.92\,B*D - 1.44\,B*E + 1.12\,C*D + 0.29\,C*E - 1.16\,D*E - 0.02\,A*B*C*E - 11.86\,\text{Ct Pt}$$

Equation A.3.

The regression model for the retention is:

$$\text{Retentate (\%)} = 57.751 + 10.861\,A + 11.212\,B - 21.022\,C - 4.59\,D + 1.138\,E - 2.350\,A*B - 1.253\,A*C + 4.152\,A*D - 2.219\,A*E + 6.798\,B*C + 0.275\,B*D + 1.080\,B*E - 2.910\,C*D - 0.064\,C*E + 5.177\,D*E + 0.89\,A*B*C*E + 9.72\,\text{Ct Pt}$$

In equation A.2 and A.3, high value of coefficients indicates large effect on the response and the sign indicates the nature of its effect. All the terms had significant effect on the output measured with some exceptions. In case of recovery output (**Equation A.2**), C*E had the least effect amongst two-way interactions and also the four-way interactions were found to be negligible. Whereas for retentate (**Equation A.3**), C*E was also found to be least influential to the output. Furthermore, the nature of solvent, flow rate and the condensation temperature had negative effects on the recovery while evaporation temperature and base surface area of the unit had positive effects. In case of retentate, an opposite trend was observed.

The coefficients of determination (R^2) were 0.9988 for the recovery and 0.9981 for retentate outputs, obtained from the software. The ANOVA **Table A.3** displays the results obtained for the fit as Sum-of-squares (SS), Mean squares (Adj MS) and F-value, which were used to calculate the P-value by the software for recovery and retentate. The P-value as α=0.05 significance level, infers the statistical significance of the response. From **Table A.3**, all the factors and their two-way interactions were found to be significant except for C*E,

similar to **equation A.2**. This suggested that there was no correlation between evaporation temperature and condensation temperature to the recovery output. Whereas in case of retentate, P-value suggested that the interaction factors B*D and C*E was not significant with the retentate. That is, along with C*E, the combined effect of flow rate and base surface area of evaporation unit had insignificant effects compared to the solvent boiling point and evaporation temperature with these factors. The P-value-lack-of-fit for both recovery and retentate were found to be greater than significance level, indicating that the model rightly specified the relationship.

Table A.3: Analysis of Variance (ANOVA) of recovery and Retentate

		Recovery (%)				Retentate (%)			
Sources	**DF**	**SS**	**MS**	**F**	**P**	**SS**	**MS**	**F**	**P**
Main Effects	5	17855.6	3571.12	2500.93	0.000	22456.5	4491.3	1506.71	0.000
A	1	9960.1	9960.12	6975.27	0.000	3774.7	3774.7	1266.31	0.000
B	1	1597.5	1597.53	1118.78	0.000	4022.7	4022.7	1349.52	0.000
C	1	5837.1	5837.06	4087.81	0.000	14141.1	14141.1	4743.99	0.000
D	1	421.2	421.17	294.95	0.000	476.5	476.5	159.85	0.000
E	1	39.7	39.72	27.82	0.000	41.4	41.4	13.9	0.002
2-Way Interactions	10	2243.3	224.33	157.1	0.000	3583.4	358.3	120.21	0.000
A*B	1	91.4	91.45	64.04	0.000	176.7	176.7	59.28	0.000
A*C	1	830.9	830.86	581.87	0.000	50.3	50.3	16.86	0.001
A*D	1	499.7	499.69	349.94	0.000	551.6	551.6	185.05	0.000
A*E	1	183.6	183.63	128.6	0.000	157.5	157.5	52.84	0.000
B*C	1	457.8	457.77	320.58	0.000	1478.6	1478.6	496.05	0.000
B*D	1	27.3	27.31	19.12	0.000	2.4	2.4	0.81	0.381
B*E	1	66.6	66.57	46.62	0.000	37.3	37.3	12.52	0.003
C*D	1	40.4	40.41	28.3	0.000	271.1	271.1	90.93	0.000
C*E	1	2.7	2.75	1.92	0.183	0.1	0.1	0.04	0.837
D*E	1	42.9	42.87	30.02	0.000	857.8	857.8	287.76	0.000
Curvature	1	264.9	264.91	185.52	0.000	177.8	177.8	59.65	0.000
Residual Error	17	24.3	1.43			50.7	3.0		
Lack of fit	1	0.0	0.0	0.00	0.984	1.5	1.5	0.49	0.494
Pure Error	16	24.3	1.52			49.2	3.1		
Total	33	20388.1				26268.3			

*DF – Degrees of Freedom; SS – Sum-of-squares; MS – Mean square

Further, the experimental results of measured recovery showed that the most significant factors affecting the recovery and retentate were the type of solvent, the flow rate of solvent from the dispenser, evaporation unit's temperature and base surface area. The condensation unit temperature had negligible effects. This is illustrated in the Pareto charts (**Fig A.5 A and**

C). The results displayed that the solvent boiling point and the evaporation temperature had the higher effects on the recovery, while evaporation temperature and sample flow rate had the most effect on retentate. These factors are interrelated to each other.

Upon optimization of the process, the predicted value for maximum recovery was 86.05% for acetone with sample input rate of 3 ml/min, 72°C evaporation unit temperature, 50 cm^2 surface area of evaporation unit flask base, and 2°C condensation unit temperature. The experimental value for the recovery for the above condition was 83.96%, which is well within the range and comparable to the predicted value. Similar result was observed in **Table A.1**. And converse of the above parameters yielded the no recovery.

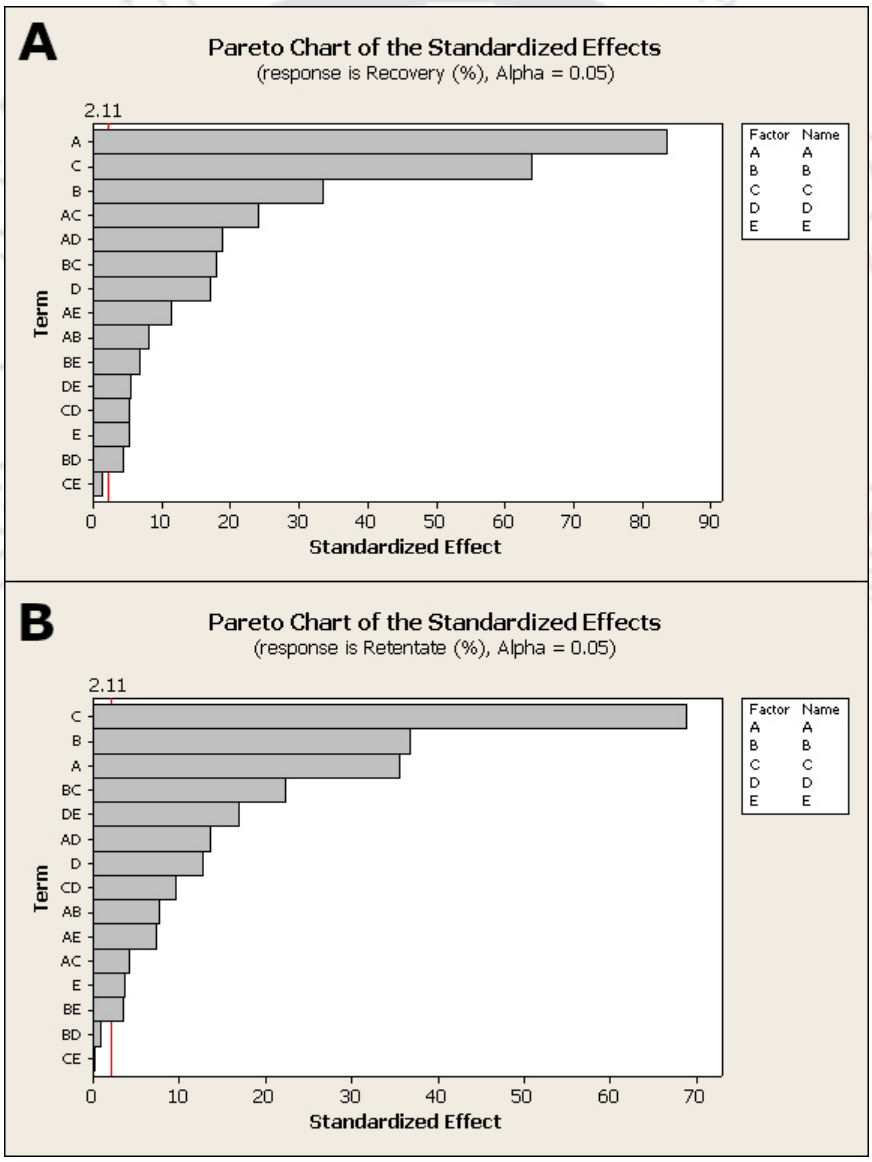

Figure A.5: Pareto charts for (A) Recovery and (C) Retentate.

The device developed is not restricted to the solvents used in the screening experiments. These experiments was carried out to understand how each factor, either individually or in the influence of one another, affects the overall evaporation and recovery process of the apparatus design. It was inferred that the overall efficiency of the apparatus relied on increasing the heat exchange of the sample solvent for evaporation. Thus, the samples with lower flow rate exposing to a larger surface area with higher temperature than the solvent boiling point resulted in better outcomes. When the sample flow rate was low and employed over larger evaporation base surface area, it reduced flooding of the evaporation chamber and ensured a thin film of solvent over a heated surface area. This enabled uniform heat distribution and increased the evaporation flux rate. The condensation temperature in the range of 2-13 ºC was found to be least influential and thus the user can employ either ice flakes or chill water within this temperature range, without affecting the overall efficiency. To conclude, influential parameters affecting the evaporation rate of sample and in turn the recovery efficiency of the apparatus are solvent boiling point, evaporation temperature, sample flow rate of the sample to evaporation unit and base surface area of the unit.

A.3.3. Comparison with alternative design combinations

In this device, the novel aspects governing the efficiency of the system are (1) method for improved heat exchange, i.e., combination of sample dispenser and evaporation unit and (2) high solvent recovery due to self-fabricated long condenser glass coil. The performance of the above components were compared with conventional design combinations for the best optimized parameter combination obtained from the 2_V^{5-1} fractional factorial analysis, i.e., acetone with 3 ml/min flow rate, subjected to at 72 ºC using flask surface area of 50 cm^2, condensation temperature of 2ºC and -300-350 mbar vacuum pressure.

The evaporation system in the current setup is a combination of sample dispenser and evaporation unit as a whole (dispenser type system) was compared in terms of solvent evaporation rate, to the conventional distillation type system. The evaporation flux rate (ml $min^{-1}cm^{-2}$) was measured for three different solvent input volumes for both the systems. In the distillation type system, the entire volume of the sample was taken in the evaporation flask. The dispenser type system had 70-fold higher evaporation flux rate than distillation type system. This is because the volume of sample being exposed to the heating surface is lower in the dispenser type system, compared to the bulk solvent taken in the distillation type

systems, which enhanced the evaporation flux rate (**Fig A.6 A**). Also in distillation type systems, the solvent volume taken as a bulk will affect the evaporation flux rates. Thus flux rates were measured for different solvent volumes, i.e., 10.5 ml, 31.5 ml and 52.5 ml. It was observed that the evaporation flux rates slightly decreased with increase in solvent volumes for distillation type system, attributed to poor heat distribution for larger volumes taken in bulk. On the contrary for dispenser type system, the volume of solvent exposed to the heated surface area in the flask was the same at any time of the run, irrespective of the sample volume in the sample dispenser. This was achieved because the solvent was dispensed into the evaporation flask at a constant flow rate resulting in a constant evaporation flux rate throughout the entire experimental run. Thus, it can be concluded that the dispenser type system incorporated in this device, enhances the evaporation flux rate of the sample.

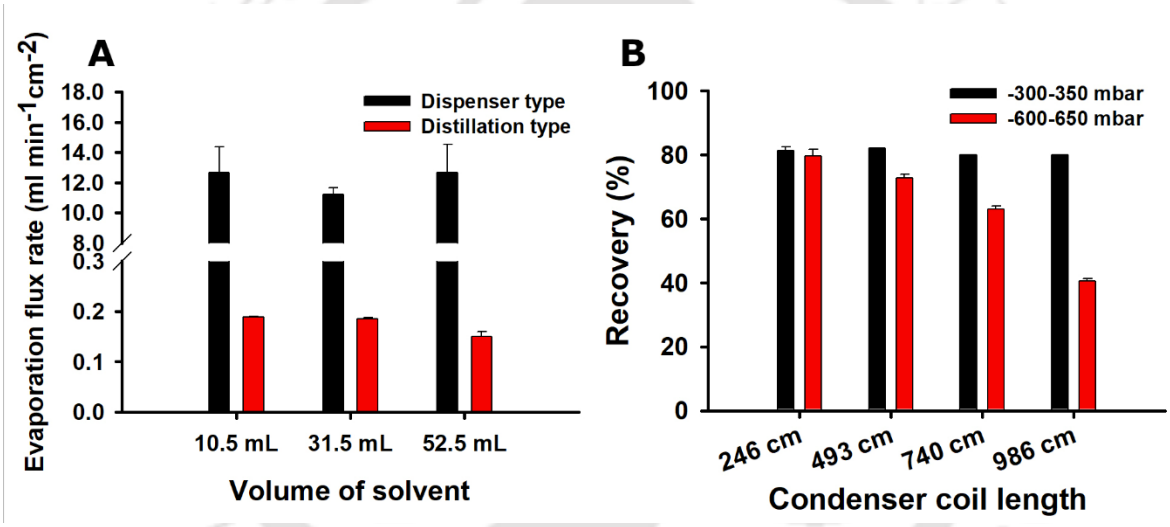

Figure A.6: (A) Evaporation flux rates of dispenser type and distillation type systems. (B) Recovery (%) with different condenser coil lengths at different vacuum pressures.

Conventional condensers usually have shorter tube lengths, which might not be suited for certain applications. In this case, the amount of solvent recovered depends on the condenser coil length for a given vacuum pressure. In order to achieve minimum solvent loss, there is a specific length of the condenser coil required for a particular vacuum pressure applied. In the current work, solvent recovery was measured for four different coil lengths, i.e., 246.5 cm, 493 cm, 740 cm and 986 cm at two different vacuum pressure ranges, i.e., -300-350 mbar and -600-650 mbar. For the vacuum pressure (-300-350 mbar) optimized in 2_V^{5-1} fractional factorial analysis, the recovery was found to be independent of the condenser lengths under consideration (**Fig A.6 B**). However, upon applying high vacuum pressure (-600-650 mbar),

there was a gradual decrease in the solvent recovery with decrease in lengths of condenser coil. Thus fabrication of glass condenser coils to any desired length is a huge advantage for the device. With this, high vacuum pressures can be used for increasing evaporation efficiency without affecting the solvent recovery. Moreover, since the each glass tube is connected via silicone tubes, it is easily attached and detached as per the required lengths.

A.4. Conclusions

A inexpensive and easy-to-assemble device for solvent evaporation and recovery was developed, which was utilized for MMG extraction, isolation and purification steps as an alternative for rotary evaporator. It worked on the principle of evaporation under reduced pressure and increased surface area for heat exchange. It consisted of a sample reservoir from which the sample was dispensed into a heated flask for evaporation. The vapours of the solvent were condensed and collected into another flask under reduced pressure. The major benefits of this setup over the commercial equipment, rotary evaporator, and other similar set-ups are cost-effectiveness, modular design, and customizability as per the requirement of the user where simultaneous operation of multiple samples either containing same or different solvent compositions was possible. This design incorporates sample dispenser and evaporation unit as a whole to increase heat exchange and fabrication of flexible glass condenser coils for efficient recovery of solvents.

The device has been filed for Patent (Application no. 202131005168).

List of Conferences and Publications

CONFERENCE PRESENTATIONS:

1. Sanjana S., A. N. Panda, L. Rangan, R. Swaminathan, "Effect of pH and ions on absorption spectroscopic behaviour of Mammeigin in different solvent systems", Shotgun oral and poster presentation, *5th International Caparica Conference on Chromogenic and Emissive Materials*, 2022, Caparica, Portugal. SG/PSG.09. pp 199.
2. Sanjana S., S. Shreekant, M. K. Gupta, H. Boro, R. Swaminathan, L. Rangan, "Device for evaporation and recovery of organic solvents using simple labwares", Model presentation, *Innovation & Entrepreneurship Conclave*, IEC 2022, IIT Guwahati, India.
3. Sanjana S., L. Rangan, R. Swaminathan, "Investigating the role of surfactant charge in the interaction of plant polyphenol Mammeigin with micelles using UV-vis spectroscopy", Poster presentation at *66th Biophysical Society Annual Meeting,* 2022, San Francisco, California, USA. Poster no. 2333.
4. Sanjana S., L. Rangan, R. Swaminathan, "Spectroscopic investigations of Mammeigin from *Mesua ferrea* in understanding the structural dynamics under different solvent conditions", Poster presentation at *A National Workshop on 'Fluorescence and Raman Spectroscopy'* (FCS-2020) (virtual mode), 2020, Mumbai, India. poster no. 89.
5. Sanjana S., R. Swaminathan, L. Rangan, "Purification and Characterization of Mammeigin: A possible therapeutic neoflavonoid from *Mesua ferrea*", Poster presentation at *International conference on 'Nutraceuticals and Chronic diseases'*, 2019, IIT Guwahati, India. pp 230.
6. Sanjana S., R. Swaminathan, L. Rangan, "Effect of extraction solvent system on the native structure of the plant metabolites: A study on *para*-coumaric acid from *Mesua ferrea*", Poster presentation at *Indian Plant Science Congress*, 2019, Chennai, India. Pp117.
7. Sanjana S., R. Swaminathan, L. Rangan, "Downstream processing of polyphenols from medicinal plants: A review", Poster presentation at *Research conclave*, 2017, IIT Guwahati, India. Pp 65.
8. Sanjana S., R. Swaminathan, L. Rangan, "Economical Rotary Evaporator" Model presentation at *Research conclave*, 2017, IIT Guwahati, India. Pp 65.

CONFERENCE PUBLICATION:

1. Sanjana S., L. Rangan, R. Swaminathan, "Investigating the role of surfactant charge in the interaction of plant polyphenol Mammeigin with micelles using UV-vis spectroscopy", *Biophysical Journal*, vol.121, no.3, p. 482a, 2022, doi:10.1016/j.bpj.2021.11.356.

JOURNAL PUBLICATIONS:

1. S. Mitra, A. Ghose, N. Gujre, Sanjana S., P. Borah, A. Paul, L. Rangan, "A review on environmental and socioeconomic perspectives of three promising biofuel plants *Jatropha curcas, Pongamia pinnata* and *Mesua ferrea*," *Biomass and Bioenergy*, vol. 151, p. 106173, Aug. 2021, doi: 10.1016/j.biombioe.2021.106173.

2. A. Singh, Mohd. Z. Ansari, Sanjana S., L. Rangan, and R. Swaminathan, "Enhanced solubility, electronic absorption and fluorescence observed for Karanjin in aqueous SDS micelles compared to water," *Journal of Photochemistry and Photobiology A: Chemistry*, vol. 414, p. 113289, Jun. 2021, doi: 10.1016/j.jphotochem.2021.113289.

3. M. K. Gupta, Sanjana S., A. K. Chiranjivi, K. Banik, S. Girisa, A. B. Kunnumakkara, V. K. Dubey, L Rangan, "Antioxidant, anti-tyrosinase and anti-inflammatory activities of 3,5-dihydroxy-4′,7- dimethoxyflavone isolated from the leaves of *Alpinia nigra*," *Phytomedicine Plus*, Vol. 1 (3), p. 100097, Aug. 2021. doi:10.1016/j.phyplu.2021.100097.

4. Sanjana S., R. Singh, L. Rangan and R. Swaminathan, "Enhanced Electronic Absorption and Solubility of Mammeigin in Aqueous Micelles and Protein Aggregate solutions compared to water ". (Manuscript under preparation)

5. Sanjana S., A. N. Panda, L. Rangan and R. Swaminathan, "Effect of pH and ions on the spectroscopic properties of Mammeigin in different surfactant systems". (Manuscript under preparation)

PATENT:

1. Sanjana S., S. Shreekant, M. K. Gupta, H. Boro, R. Swaminathan, L. Rangan, "Device for evaporation and recovery of organic solvents using simple labwares", Appl. No. 202131005168 (under process in patent office).

References

Abedi-Firoozjah, R., Yousefi, S., Heydari, M., Seyedfatehi, F., Jafarzadeh, S., Mohammadi, R., Rouhi, M., Garavand, F., 2022. Application of Red Cabbage Anthocyanins as pH-Sensitive Pigments in Smart Food Packaging and Sensors. Polymers 14, 1629.

Abeysena, I., 2013 Understanding Evaporation and Concentration Technologies. *Genevac Ltd*, Ipswich, UK. Labmate. https://www.labmate-online.com/article/laboratory-products/3/genevac-ltd/understanding-evaporation-and-concentration-technologies/1365 (accessed on Aug 2022)

Abezgauz, L., Kuperkar, K., Hassan, P.A., Ramon, O., Bahadur, P., Danino, D., 2010. Effect of Hofmeister anions on micellization and micellar growth of the surfactant cetylpyridinium chloride. Journal of Colloid and Interface Science 342, 83–92.

Adebooye, O.C., Alashi, A.M., Aluko, R.E., 2018. A brief review on emerging trends in global polyphenol research. Journal of Food Biochemistry 42, e12519.

Adhikary, R., Mukherjee, P., Kee, T.W., Petrich, J.W., 2009. Excited-State Intramolecular Hydrogen Atom Transfer and Solvation Dynamics of the Medicinal Pigment Curcumin. The Journal of Physical Chemistry B 113, 5255–5261.

Ali, O.M., Hashem, Y., Bekhit, A.A., Khattab, S.N., Elkhodairy, K.A., Freag, M.S., Teleb, M., Elzoghby, A.O., 2019. 8 - Nanostructures of gelatin for encapsulation of food ingredients, in: Jafari, S.M. (Ed.), Biopolymer Nanostructures for Food Encapsulation Purposes, Nanoencapsulation in the Food Industry. Academic Press, 189–216.

Amat, A., Clementi, C., De Angelis, F., Sgamellotti, A., Fantacci, S., 2009. Absorption and Emission of the Apigenin and Luteolin Flavonoids: A TD-DFT Investigation. The Journal of Physical Chemistry A 113, 15118–15126.

Anouar, E.H., Osman, C.P., Weber, J-F.F., Ismail, N.H., 2014. UV/Visible spectra of a series of natural and synthesised anthraquinones: experimental and quantum chemical approaches. SpringerPlus 3, 233.

Ansari, M.Z., Kumar, A., Ahari, D., Priyadarshi, A., Lolla, P., Bhandari, R., Swaminathan, R., 2018. Protein charge transfer absorption spectra: an intrinsic probe to monitor structural and oligomeric transitions in proteins. Faraday Discuss 207, 91–113.

Arora, P., Ansari, S., Nazish, I., 2019. *Mesua Ferrea*: An Ethnobotanically Important Plant. American Journal of PharmTech Research 9, 31–39.

Arshad, N., Rashid, N., Absar, S., Abbasi, M., Saleem, S., Mirza, B., 2013. UV-absorption studies of interaction of karanjin and karanjachromene with ds. DNA: Evaluation of binding and antioxidant activity. Open Chemistry 11, 2040–2047.

Asif, M., Jafari, F., Iqbal, Z., Revadigar, V., Oon, C.E., Farsi, E., Abdul Majid, A.M.S., 2017. Ethnobotanical and Phytopharmacological attributes of *Mesua ferrea*: A mini review. Journal of Applied Pharmaceutical Science 7, 242–251.

Aslanoğlu, M., Öge, N., 2005. Voltammetric, UV Absorption and Viscometric Studies of the Interaction of Norepinephrine with DNA. Turkish Journal of Chemistry 29, 477–485.

Aygün, S., Beşer, B.M., Acar, M., Meral, K., 2020. Photophysical Properties of Some Fluorescent Dyes in SDS Micellar Solutions. Journal of Fluorescence 30, 849–857.

Bala, K.R., Seshadri, T.R., 1971. Isolation and synthesis of some coumarin components of *Mesua ferrea* seed oil. Phytochemistry 10, 1131–1134.

Balakrishnan, P., Lee, B.-J., Oh, D.H., Kim, J.O., Hong, M.J., Jee, J-P., Kim, J.A., Yoo, B.K., Woo, J.S., Yong, C.S., Choi, H-G., 2009. Enhanced oral bioavailability of dexibuprofen by a novel solid self-emulsifying drug delivery system (SEDDS). European Journal of Pharmaceuticals and Biopharmaceutics 72, 539–545.

Balasubramanian, K., 1991. Theoretical calculations on the transition energies of the UV-visible spectra of curcurnin pigment in turmeric. Indian Journal of Chemistry 30A, 61-65.

Bandaranayake, W.M., Selliah, S.S., Sultanbawa, M.U.S., Games, D.E., 1975. Xanthones and 4-phenylcoumarins of *Mesua thwaitesii*. Phytochemistry 14, 265–269.

Bansal, A., Priyadarsini, C., 2021. Medicinal Properties of Phytochemicals and Their Production, Natural Drugs from Plants, in: Pharmacognosy-Medicinal Plants. IntechOpen.

Bedoya, L.M., Beltrán, M., Sancho, R., Olmedo, D.A., Sánchez-Palomino, S., del Olmo, E., López-Pérez, J.L., Muñoz, E., San Feliciano, A., Alcamí, J., 2005. 4-Phenylcoumarins

as HIV transcription inhibitors. Bioorganic & Medicinal Chemistry Letters 15, 4447–4450.

Bhat, M.P., Madhuprasad, Patil, P., Nataraj, S.K., Altalhi, T., Jung, H-Y., Losic, D., Kurkuri, M.D., 2016. Turmeric, naturally available colorimetric receptor for quantitative detection of fluoride and iron. Chemical Engineering Journal 303, 14–21.

Bhatia, N.K., Kishor, S., Katyal, N., Gogoi, P., Narang, P., Deep, S., 2016. Effect of pH and temperature on conformational equilibria and aggregation behaviour of curcumin in aqueous binary mixtures of ethanol. RSC Advances 6, 103275–103288.

Bhattacharyya, K., Bagchi, B., 2000. Slow Dynamics of Constrained Water in Complex Geometries. Journal of Physical Chemistry A 104, 10603–10613.

Biasutto, L., Mattarei, A., Sassi, N., Azzolini, M., Romio, M., Paradisi, C., Zoratti, M., 2014. Improving the efficacy of plant polyphenols. Anticancer Agents Med 14, 1332–1342.

Biler, M., Biedermann, D., Valentová, K., Křen, V., Kubala, M., 2017. Quercetin and its analogues: optical and acido–basic properties. Physical Chemistry Chemical Physics 19, 26870–26879.

Biler, M., Trouillas, P., Biedermann, D., Křen, V., Kubala, M., 2016. Tunable optical properties of silymarin flavonolignans. Journal of Photochemistry and Photobiology A: Chemistry 328, 154–162.

Bora, P., Boro, J., Deka, D., 2013. A study on the development of *Mesua ferrea* l. seed oil based microemulsified fuel system. International Journal of Emerging Technology and Advanced Engineering 3 (3), 47-51.

Boudet, A.-M., 2007. Evolution and current status of research in phenolic compounds. Phytochemistry, Highlights in the Evolution of Phytochemistry: 50 Years of the Phytochemical Society of Europe 68, 2722–2735.

Brouwer, A.M., 2011. Standards for photoluminescence quantum yield measurements in solution (IUPAC Technical Report). Pure and Applied Chemistry 83, 2213–2228.

Brovarets', O.O., Hovorun, D.M., 2020. Conformational transitions of the quercetin molecule via the rotations of its rings: a comprehensive theoretical study. Journal of Biomolecular Structure and Dynamics 38, 2865–2883.

Buffer Reference Center,
https://www.sigmaaldrich.com/IN/en/technical documents/protocol/protein-biology/protein-concentration-and-buffer-exchange/buffer-reference-center#citric2 (accessed on December 2022).

Camuri, I.J., Costa, A.B., Ito, A.S., Pazin, W.M., 2018. Optical absorption and fluorescence spectroscopy studies of Artepillin C, the major component of green propolis. Spectrochimica Acta Part A: Molecular and Biomolecular Spectroscopy 198, 71–77.

Cantor, C.R., Schimmel, P.R., 1980. Biophysical Chemistry: Part II: Techniques for the Study of Biological Structure and Function. W. H. Freeman.

Carpenter, I., McGarry, E.J., Scheinmann, F., 1971. Extractives from Guttiferae. Part XXI. The isolation and structure of nine coumarins from the bark of *Mammea africana* G. Don. Journal of Chemical Society C 3783–3790.

Chahar, K., 2013. *Mesua ferrea* L.: A review of the medical evidence for its phytochemistry and pharmacological actions. African Journal of Pharmacy and Pharmacology 7, 211–219.

Chandrakala, V., Aruna, V., Angajala, G., 2022. Review on metal nanoparticles as nanocarriers: current challenges and perspectives in drug delivery systems. Emergent mater 1-23.

Chang, C., Li, J., Su, Y., Gu, L., Yang, Y., Zhai, J., 2022. Protein particle-based vehicles for encapsulation and delivery of nutrients: Fabrication, digestion, and release properties. Food Hydrocolloids 123, 106963.

Chaniad, P., Chukaew, A., Payaka, A., Phuwajaroanpong, A., Techarang, T., Plirat, W., Punsawad, C., 2022. Antimalarial potential of compounds isolated from *Mammea siamensis* T. Anders. flowers: *in vitro* and molecular docking studies. BMC Complement Med Ther 22, 266.

Chatterjee, S., Suresh Kumar, G., 2016. Visualization of Stepwise Drug-Micelle Aggregate Formation and Correlation with Spectroscopic and Calorimetric Results. Journal of Physical Chemistry B 120, 11751–11760.

Chaudhuri, A., Haldar, S., Chattopadhyay, A., 2011. Structural transition in micelles: Novel insight into microenvironmental changes in polarity and dynamics. Chemistry and physics of lipids 165, 497–504.

Chen, H., Khemtong, C., Yang, X., Chang, X., Gao, J., 2011. Nanonization strategies for poorly water-soluble drugs. Drug Discovery Today 16, 354–360.

Chen, X-Q., Gudmundsson, O.S., Hageman, M.J., 2012. Application of Lipid-Based Formulations in Drug Discovery. Journal of Medicinal Chemistry 55, 7945–7956.

Cheremisinoff, N.P., 2003. Industrial Solvents Handbook, Revised And Expanded. CRC Press.

Cheynier, V., Comte, G., Davies, K.M., Lattanzio, V., Martens, S., 2013. Plant phenolics: Recent advances on their biosynthesis, genetics, and ecophysiology. Plant Physiology and Biochemistry 72, 1–20.

Chiti, F., Dobson, C.M., 2006. Protein misfolding, functional amyloid, and human disease. Annual Review of Biochemistry 75, 333–366.

Chow, Y.L., Quon, H.H., 1968. Chemical constituents of the heartwood of *Mesua ferrea*. Phytochemistry 7, 1871–1874.

Cornard, J.P., Merlin, J.C., Boudet, A.C., Vrielynck, L., 1997. Structural study of quercetin by vibrational and electronic spectroscopies combined with semiempirical calculations. Biospectroscopy 3, 183–193.

Craig, L.C., Gregory, J.D., Hausmann, W., 1950. Versatile Laboratory Concentration Device. Analytical Chemistry 22, 1462-1462.

Crombie, L., Games, D.E., Haskins, N.J., Read, G.F., 1970. Isolation and structure of insecticidal components from *Mammea americana* L. Tetrahedron Letters 11, 251–254.

Crombie, L., Games, D.E., Haskins, N.J., Reed, G.F., 1972. Extractives of *Mammea americana* L. Part V. The insecticidal compounds. Journal of the Chemical Society, Perkin Trans 1, 2255–2260.

Cruz, F.G., Silva-Neto. J.T. da, Guedes, M.L.S., 2001. Xanthones and Coumarins from *Kielmeyera lathrophyton*. Journal of the Brazilian Chemical Society 12.

Cunha, M.G. da, Rosalen, P.L., Franchin, M., Alencar, S.M. de, Ikegaki, M., Ransom, T., Beutler, J.A., 2016. Antiproliferative Constituents of Geopropolis from the Bee Melipona scutellaris. Planta Medica 82, 190–194.

Daayf, F., Lattanzio, V., 2009. Recent Advances in Polyphenol Research. John Wiley & Sons.

Danaf, N.A., Melhem, R.A., Assaf, K.I., Nau, W.M., Patra, D., 2016. Photophysical properties of neutral and dissociated forms of rosmarinic acid. Journal of Luminescence 175, 50–56.

Dang, B.T., Gény, C., Blanchard, P., Rouger, C., Tonnerre, P., Charreau, B., Rakolomalala, G., Randriamboavonjy, J.I., Loirand, G., Pacaud, P., Litaudon, M., Richomme, P., Séraphin, D., Derbré, S., 2014. Advanced glycation inhibition and protection against endothelial dysfunction induced by coumarins and procyanidins from *Mammea neurophylla*. Fitoterapia 96, 65–75.

Daniloski, D., Petkoska, A.T., Lee, N.A., Bekhit, A.E.-D., Carne, A., Vaskoska, R., Vasiljevic, T., 2021. Active edible packaging based on milk proteins: A route to carry and deliver nutraceuticals. Trends in Food Science & Technology 111, 688–705.

Dave, N., Joshi, T., 2017. A Concise Review on Surfactants and Its Significance. International Journal of Applied Chemistry 13, 663–672.

Devi, P., Singh, S., Sangwan, S., Sihag, S., Moond, M., 2021. Effect of pH on Phytochemical and Antioxidant Potential of Satawar Tubers (*Asparagus Racemosus* Willd.). Journal of Antioxidant Activity 2, 42-50.

Donbrow, M., Azaz, E., Pillersdorf, A., 1978. Autoxidation of Polysorbates. Journal of Pharmaceutical Sciences 67, 1676–1681.

Doriguetto, A.C., Ellena, J., Dos Santos, M.H., Moreira, M.E.C., Nagem, T.J., 2006. Mammeigin. Acta Crystallographica Section C 62, o350–o352.

Dutta, A., Boruah, B., Manna, A.K., Gohain, B., Saikia, P.M., Dutta, R.K., 2013. Stabilization of diketo tautomer of curcumin by premicellar anionic surfactants: UV–Visible, fluorescence, tensiometric and TD-DFT evidences. Spectrochimica Acta Part A: Molecular and Biomolecular Spectroscopy 104, 150–157.

Erickson, M.D., Giguere, M.T., Whitaker, D.A., 1981. Comparison of Common Solvent Evaporation Techniques in Organic Analysis. Analytical Letters 14, 841–857.

Evale, B.G., Hanagodimath, S.M., Khan, I.A., Kulkarni, M.V., 2009. Estimation of dipole moments of some biologically active coumarins by solvatochromic shift method based on solvent polarity parameter, E(T)(N). Spectrochimica acta. Part A, Molecular and Biomolecular Spectroscopy 73, 694–700.

Faraji, M., Farajtabar, A., 2020. Preferential solvation of quercetin in aqueous aprotic solvent mixtures. Journal of the Serbian Chemical Society 85, 227–236.

Farajtabar, A., Gharib, F., 2013. Spectral analysis of naringenin deprotonation in aqueous ethanol solutions. Chemical Papers 67, 538–545.

Favaro, G., Clementi, C., Romani, A., Vickackaite, V., 2007. Acidichromism and Ionochromism of Luteolin and Apigenin, the Main Components of the Naturally Occurring Yellow Weld: A Spectrophotometric and Fluorimetric Study. Journal of Fluorescence 17, 707–714.

Fawcett, W.R., 2004. Liquids, Solutions, and Interfaces: From Classical Macroscopic Descriptions to Modern Microscopic Details. Oxford University Press.

Finnegan, R.A., Merkel, K.E., Back, N., 1972. Constituents of Mammea americana L. VIII: Novel structural variations on the mammein theme and antitumor activity of mammein and related coumarin and phloroglucinol derivatives. Journal of Pharmaceutical Sciences 61, 1599–1603.

Finnegan, R.A., Mueller, W.H., 1965. Constituents of *Mammea americana* L. IV. The Structure of Mammeigin. The Journal of Organic Chemistry 30, 2342–2344.

Frieden, C., 2007. Protein aggregation processes: In search of the mechanism. Protein Science 16, 2334–2344.

Friedman, M., Jürgens, H.S., 2000. Effect of pH on the Stability of Plant Phenolic Compounds. Journal of Agricultural and Food Chemistry 48, 2101–2110.

Fujii, K., Hara, Y., Arai, M.A., Sadhu, S.K., Ahmed, F., Ishibashi, M., 2022. Natural Compounds with BMI1 Promoter Inhibitory Activity from *Mammea siamensis* and *Andrographis paniculata*. Chemical and Pharmaceutical Bulletin 70, 885–891.

Funes, M., Correa, N.M., Silber, J.J., Biasutti, M.A., 2007. Comparative Study of the Photophysical Behavior of Fisetin in Homogeneous Media and in Anionic and Cationic Reverse Micelles Media. Photochemistry and Photobiology 83, 486–493.

Furkan, M., Siddiqi, M.K., Zakariya, S.M., Khan, F.I., Hassan, Md.I., Khan, R.H., 2019. An *In Vitro* elucidation of the antiaggregatory potential of Diosminover thermally induced unfolding of hen egg white lysozyme; A preventive quest for lysozyme amyloidosis. International Journal of Biological Macromolecules 129, 1015–1023.

Gao, Z., Zhao, J., Huang, Y., Yao, X., Zhang, K., Fang, Y., Nishinari, K., Phillips, G.O., Jiang, F., Yang, H., 2017. Edible Pickering emulsion stabilized by protein fibrils. Part 1: Effects of pH and fibrils concentration. LWT - Food Science and Technology 76, 1–8.

Garazd, M., Garazd, Y., Khilya, V., 2003. Neoflavones. 1. Natural Distribution and Spectral and Biological Properties. Chemistry of Natural Compounds 39, 54–121.

German, J.B., Walzem, R.L., 2000. The health benefits of wine. Annual Review of Nutrition 20, 561–593.

Goszcz, K., Duthie, G.G., Stewart, D., Leslie, S.J., Megson, I.L., 2017. Bioactive polyphenols and cardiovascular disease: chemical antagonists, pharmacological agents or xenobiotics that drive an adaptive response? British Journal of Pharmacology 174, 1209–1225.

Gou, S., Chen, Q., Liu, Y., Zeng, L., Song, H., Xu, Z., Kang, Y., Li, C., Xiao, B., 2018. Green Fabrication of Ovalbumin Nanoparticles as Natural Polyphenol Carriers for Ulcerative Colitis Therapy. Sustainable Chemistry & Engineering 6, 12658–12667.

Govindachari, T.R., Pai, B.R., Subramaniam, P.S., Ramdas Rao, U., Muthukumaraswamy, N., 1967a. Constituents of *Mesua ferrea* L.—II:: Ferruol A, a new 4-alkylcoumarin. Tetrahedron 23, 4161–4165.

Govindachari, T.R., Pai, B.R., Subramaniam, P.S., Rao, U.R., Muthukumaraswamy, N., 1967b. Constituents of *Mesua ferrea* L.—I: Mesuaxanthone A and mesuaxanthone B. Tetrahedron 23, 243–248.

Gramacho, R. da S., Nagem, T.J., de Oliveira, T.T., de Queiroz, M.E.L.R., Neves, A.A., Saddi, N., 1999. Phenylcoumarins from *Kielmeyera elata*. Phytochemistry 51, 579–581.

Gregory, K.P., Elliott, G.R., Robertson, H., Kumar, A., Wanless, E.J., Webber, G.B., Craig, V.S.J., Andersson, G.G., Page, A.J., 2022. Understanding specific ion effects and the Hofmeister series. Physical Chemistry Chemical Physics 24, 12682–12718.

Guo, Q., Zhao, B., Shen, S., Hou, J., Hu, J., Xin, W., 1999. ESR study on the structure–antioxidant activity relationship of tea catechins and their epimers. Biochimica et Biophysica Acta (BBA) - General Subjects 1427, 13–23.

Hamzeloo-Moghadam, M., Taiebi, N., Mosaddegh, M., Tehrani, B., Esmaeili, S., 2014. The effect of some cosolvents and surfactants on viability of cancerous cell lines. Research Journal of Pharmacognosy 1, 41-45.

Harborne, J.B., 1980. Plant Phenolics. Secondary Plant Products 329–402.

Harborne, J.B., Williams, C.A., 2000. Advances in flavonoid research since 1992. Phytochemistry 55, 481–504.

He, F., Liang, N-N., Mu, L., Pan, Q-H., Wang, J., Reeves, M.J., Duan, C-Q., 2012. Anthocyanins and Their Variation in Red Wines I. Monomeric Anthocyanins and Their Color Expression. Molecules 17, 1571–1601.

Hoffman, R.V., 1976. The construction of an inexpensive rotary evaporator. Journal of Chemical Education 53, 459.

Holmberg, K. (Ed.), 2007. Surfactants and polymers in aqueous solution, 2. ed., Wiley, Chichester.

Homocianu, M., Airinei, A., Dorohoi, D.O., 2011. Solvent Effects on the Electronic Absorption and Fluorescence Spectra. Journal of Advanced Research in Physics 2, 011105.

Hooshyar, H., Sadeghi, R., 2015. Influence of Sodium Salts on the Micellization and Interfacial Behavior of Cationic Surfactant Dodecyltrimethylammonium Bromide in Aqueous Solution. Journal of Chemical & Engineering Data 60, 983–992.

Hu, B., Liu, X., Zhang, C., Zeng, X., 2017. Food macromolecule based nanodelivery systems for enhancing the bioavailability of polyphenols. Journal of Food and Drug Analysis, Dietary Natural Compounds 25, 3–15.

Huang, Q., Yu, H., Ru, Q., 2010. Bioavailability and Delivery of Nutraceuticals Using Nanotechnology. Journal of Food Science 75, R50–R57.

Iosub, S., Meghea, A., Geană, I., 2014. Solvatochromic parameters of some anthocyanin derivatives concentrated from selective natural extracts. UPB Scientific Bulletin, Series B 76, 25-34.

Ivanov, I.B., Slavchov, R.I., Basheva, E.S., Sidzhakova, D., Karakashev, S.I., 2011. Hofmeister effect on micellization, thin films and emulsion stability. Advances in Colloid and Interface Science 168, 93–104.

Janakiraman, A.K., Suhail, M., Janakiraman, A.K., Khan, A., Naeem, A., Badshah, S.F., 2019. Surfactants and their role in Pharmaceutical Product Development: An Overview. Journal of Pharmacy and Pharmaceutics 6, 72–82.

Janjua, N.K., Siddiqa, A., Yaqub, A., Sabahat, S., Qureshi, R., Haque, S. ul, 2009. Spectrophotometric analysis of flavonoid–DNA binding interactions at physiological conditions. Spectrochimica Acta Part A: Molecular and Biomolecular Spectroscopy 74, 1135–1137.

Jensen, W.B., 2008. The Origin of the Rotavap. Journal of Chemical Education 85, 1481.

Jeon, J.-R., Kim, J.-H., Chang, Y.-S., 2013. Enzymatic polymerization of plant-derived phenols for material-independent and multifunctional coating. Journal of Materials Chemistry B 1, 6501–6509.

Jurasekova, Z., Domingo, C., Garcia-Ramos, J.V., Sanchez-Cortes, S., 2014. Effect of pH on the chemical modification of quercetin and structurally related flavonoids characterized by optical (UV-visible and Raman) spectroscopy. Physical Chemistry Chemical Physics 16, 12802–12811.

Kamphausen, H.A., 1962. A convenient and safe method for the evaporation of organic solvents. Journal of Chemical Education 39, 208.

Kaur, H., Kaur, G., 2014. A Critical Appraisal of Solubility Enhancement Techniques of Polyphenols. Journal of Pharmaceutics 2014, e180845.

Khopde, S.M., Priyadarsini, K.I., Palit, D.K., Mukherjee, T., 2000. Effect of Solvent on the Excited-state Photophysical Properties of Curcumin. Photochemistry and Photobiology 72, 625–631.

Kok, R.J., Haas, M., Moolenaar, F., de Zeeuw, D., Meijer, D.K., 1998. Drug delivery to the kidneys and the bladder with the low molecular weight protein lysozyme. Renal Failure 20, 211–217.

Konwer, D., Taylor, S.E., Gordon, B.E., Otvos, J.W., Calvin, M., 1989. Liquid fuels from *Mesua ferrea* L. seed oil. Journal of the American Oil Chemists' Society 66, 223–226.

Kralova, I., Sjöblom, J., 2009. Surfactants Used in Food Industry: A Review. Journal of Dispersion Science and Technology 30, 1363–1383.

Kumar, B., Tikariha, D., Ghosh, K.K., 2012. Effects of Electrolytes on Micellar and Surface Properties of Some Monomeric Surfactants. Journal of Dispersion Science and Technology 33, 265–271.

Kumar, M., Puri, A., 2012. A review of permissible limits of drinking water. Indian Journal of Occupational and Environmental Medicine 16, 40–44.

Kumar, P., Ahamad, T., Mishra, D.P., Khan, M.F., 2020. Plant Neoflavonoids: Chemical Structures and Biological Functions, in: Swamy, M.K. (Ed.), Plant-Derived Bioactives: Chemistry and Mode of Action. Springer, Singapore, 35–57.

Kumar, P., Deepika, Khatri, H., Singh, J., 2022. Solubility Enhancement Techniques by Solid Dispersion. Journal of Pharma Innovation 1, 10-17.

Kumar, S., Pandey, A.K., 2013. Chemistry and Biological Activities of Flavonoids: An Overview. Scientific World Journal 162750.

Kumar, S., Udgaonkar, J.B., 2010. Mechanisms of amyloid fibril formation by proteins. Current Science 98, 639–656.

Kuperkar, K., Abezgauz, L., Prasad, K., Bahadur, P., 2010. Formation and Growth of Micelles in Dilute Aqueous CTAB Solutions in the Presence of $NaNO_3$ and $NaClO_3$. Journal of Surfactants and Detergents 13, 293–303.

Lakowicz, J.R., 2013. Principles of Fluorescence Spectroscopy. Springer Science & Business Media.

Lapidot, T., Harel, S., Akiri, B., Granit, R., Kanner, J., 1999. pH-Dependent Forms of Red Wine Anthocyanins as Antioxidants. Journal of Agricultural and Food Chemistry 47, 67–70.

Lattanzio, V., 2013. in: Ramawat, K.G., Mérillon, J.-M. (Eds.), Natural Products: Phytochemistry, Botany and Metabolism of Alkaloids, Phenolics and Terpenes. Springer, Berlin, Heidelberg, 1543–1580.

Leung, M.H.M., Colangelo, H., Kee, T.W., 2008. Encapsulation of Curcumin in Cationic Micelles Suppresses Alkaline Hydrolysis. Langmuir 24, 5672–5675.

Li, M., Fokkink, R., Ni, Y., Kleijn, J.M., 2019. Bovine beta-casein micelles as delivery systems for hydrophobic flavonoids. Food Hydrocolloids 96, 653–662.

Li, Z., Jiang, H., Xu, C., Gu, L., 2015. A review: Using nanoparticles to enhance absorption and bioavailability of phenolic phytochemicals. Food Hydrocolloids 43, 153–164.

Lipinski, C.A., Lombardo, F., Dominy, B.W., Feeney, P.J., 2001. Experimental and computational approaches to estimate solubility and permeability in drug discovery and development settings. Advanced Drug Delivery Reviews 46, 3–26.

Liu, H-B., Yu, D., Shin, S.C., Park, H-R., Park, J.K., Bark, K-M., 2009. Spectroscopic Properties of Quercetin Derivatives, Quercetin-3-O-rhamnoside and Quercetin-3-O-rutinoside, in Hydro-organic Mixed Solvents. Photochemistry and Photobiology 85, 934–942.

Liu, R., Yang, J., Wu, X., Hua, S., Sun, C., 2001. Interaction of morin with CTMAB: aggregation and location in micellar. Spectrochimica Acta Part A: Molecular and Biomolecular Spectroscopy 57, 2561–2566.

Liu, W., Guo, R., 2006a. Interaction of flavonoid, quercetin with organized molecular assemblies of nonionic surfactant. Colloids and Surfaces A: Physicochemical and Engineering Aspects 274, 192–199.

Liu, W., Guo, R., 2006. Interaction between flavonoid, quercetin and surfactant aggregates with different charges. Journal of Colloid and Interface Science 302, 625–632.

Lo Nostro, P., Ninham, B.W., 2012. Hofmeister Phenomena: An Update on Ion Specificity in Biology. Chemical Reviews 112, 2286–2322.

López-Pérez, J.L., Olmedo, D.A., del Olmo, E., Vásquez, Y., Solís, P.N., Gupta, M.P., San Feliciano, A., 2005. Cytotoxic 4-Phenylcoumarins from the Leaves of *Marila pluricostata*. Journal of Natural Products 68, 369–373.

Lu, Y., Zhang, E., Yang, J., Cao, Z., 2018. Strategies to improve micelle stability for drug delivery. Nano Research 11, 4985–4998.

Mabrouk, M.M., Hamed, N.A., Mansour, F.R., 2021. Spectroscopic methods for determination of critical micelle concentrations of surfactants; a comprehensive review. Applied Spectroscopy Reviews 1–29.

Manach, C., Scalbert, A., Morand, C., Rémésy, C., Jiménez, L., 2004. Polyphenols: food sources and bioavailability. The American Journal of Clinical Nutrition 79, 727–747.

Marcus, Y., 2002. Solvent Mixtures: Properties and Selective Solvation. CRC Press.

Marcus, Y., 1998. The properties of solvents. Wiley.

Marković, S., Tošović, J., 2015. Application of Time-Dependent Density Functional and Natural Bond Orbital Theories to the UV–vis Absorption Spectra of Some Phenolic Compounds. Journal of Physical Chemistry A 119, 9352–9362.

Mehanna, N.S., Hassan, Z.M.R., El-Din, H.M.F., Ali, A.A.-E., Amarowicz, R., El-Messery, T.M., 2014. Effect of Interaction Phenolic Compounds with Milk Proteins on Cell Line. Food and Nutrition Sciences 5, 2130–2146.

Michalík, M., Biela, M., Cagardová, D., Lukeš, V., 2020. Influence of catecholic ring torsion on hydroxyflavones. Acta Chimica Slovaca 13, 49–55.

Mitra, S., Ghose, A., Gujre, N., Senthilkumar, S., Borah, P., Paul, A., Rangan, L., 2021. A review on environmental and socioeconomic perspectives of three promising biofuel plants *Jatropha curcas, Pongamia pinnata* and *Mesua ferrea*. Biomass and Bioenergy 151, 106173.

Mohd, P., Khan, A., Farooqui, M., 2011. Analytical applications of plant extract as natural pH indicator: a review. Journal of Advanced Scientific Research 2, 20–27.

Mondal, S., Ghosh, S., Moulik, S.P., 2016. Stability of curcumin in different solvent and solution media: UV–visible and steady-state fluorescence spectral study. Journal of Photochemistry and Photobiology B: Biology 158, 212–218.

Moreira, L., Firoozabadi, A., 2010. Molecular Thermodynamic Modeling of Specific Ion Effects on Micellization of Ionic Surfactants. Langmuir 26, 15177–15191.

Morikawa, T., Luo, F., Manse, Y., Sugita, H., Saeki, S., Chaipech, S., Pongpiriyadacha, Y., Muraoka, O., Ninomiya, K., 2020. Geranylated Coumarins From Thai Medicinal Plant *Mammea siamensis* With Testosterone 5α-Reductase Inhibitory Activity. Frontiers in Chemistry 8, 199.

Nagem, T.J., A. e Silva, M.D., 1988. Xanthones and phenylcoumarins from *Kielmeyera pumila*. Phytochemistry 27, 2961–2962.

Nardo, L., Paderno, R., Andreoni, A., Másson, M., Haukvik, T., Tønnesen, H.H., 2008. Role of H-bond formation in the photoreactivity of curcumin. Spectroscopy 22, 187–198.

Neslihan Gursoy, R., Benita, S., 2004. Self-emulsifying drug delivery systems (SEDDS) for improved oral delivery of lipophilic drugs. Biomedicine & Pharmacotherapy 58, 173–182.

Nguyen, S.T., Nguyen, H.T.-L., Truong, K.D., 2020. Comparative cytotoxic effects of methanol, ethanol and DMSO on human cancer cell lines. Biomedical Research and Therapy 7, 3855–3859.

Nigam, S., Rutan, S., 2001. Principles and Applications of Solvatochromism. Applied Spectroscopy 55, 362A-370A.

Ninomiya, K., Shibatani, K., Sueyoshi, M., Chaipech, S., Pongpiriyadacha, Y., Hayakawa, T., Muraoka, O., Morikawa, T., 2016. Aromatase Inhibitory Activity of Geranylated Coumarins, Mammeasins C and D, Isolated from the Flowers of *Mammea siamensis*. Chemical & pharmaceutical bulletin 64, 880–885.

Nogueira, P., Andrade, M., Andrade, L., Moraes, V., Ribeiro, A., Bittrich, V., Amaral, M. do C., Ferreira, A., Alcantara, G., Leão, K., Alves, P., 2008. Chemical constituents from *Kielmeyera rugosa* Choisy (Clusiaceae). Biochemical Systematics and Ecology 36, 921–924.

Norris, J.F., 1924. Experimental Organic Chemistry 228. McGraw-Hill Book Company, Inc.

Pandey, K.B., Rizvi, S.I., 2009. Plant polyphenols as dietary antioxidants in human health and disease. Oxidative Medicine Cellular Longevity 2, 270–278.

Park, H-R., Im, S-E., Seo, J-J., Kim, B-G., Yoon, J.A., Bark, K-M., 2015. Spectroscopic Properties of Morin in Various $CH_3OH–H_2O$ and $CH_3CN–H_2O$ Mixed Solvents. Photochemistry and Photobiology 91, 280–290.

Park, H.-R., Park, C.-H., Park, H.-R., Park, C.-H., 2017. Spectroscopic Study on the Anti-oxidant Properties of Flavonoid Galangin. Asian Journal of Beauty Cosmetology 15, 411–419.

Pasto, D.J., 1979. Laboratory text for organic chemistry : a source book of chemical and physical techniques. Englewood Cliffs, N.J. : Prentice-Hall.

Patel, V., Dharaiya, N., Ray, D., Aswal, V., Bahadur, P., 2014. pH controlled size/shape in CTAB micelles with solubilized polar additives: A viscometry, scattering and spectral evaluation. Colloids and Surfaces A: Physicochemical and Engineering Aspects 455, 67–75.

Pavia, D.L., Lampman, G.M., 2009. Spectroscopy. Brooks/Cole, Cengage Learning.

Prajapati, K., Patel, S., 2012. Micellization of Surfactants in Mixed Solvent of Different Polarity. Archives of Applied Science Research 4, 662-668.

Priyadarsini, K.I., 2009. Photophysics, photochemistry and photobiology of curcumin: Studies from organic solutions, bio-mimetics and living cells. Journal of Photochemistry and Photobiology C: Photochemistry Reviews 10, 81–95.

Proestos, C., Zoumpoulakis, P., Sinanoglou, V., 2018. Isolation and Characterization of Phenolic Compounds From Selected Foods of Plant Origin Using Modern Spectroscopic Approaches, in: Studies in Natural Products Chemistry 57, 203-220.

Qazi, M.J., Schlegel, S.J., Backus, E.H.G., Bonn, M., Bonn, D., Shahidzadeh, N., 2020. Dynamic Surface Tension of Surfactants in the Presence of High Salt Concentrations. Langmuir 36, 7956–7964.

Quideau, S., Deffieux, D., Douat-Casassus, C., Pouységu, L., 2011. Plant polyphenols: chemical properties, biological activities, and synthesis. Angewandte Chemie International Edition 50, 586–621.

Rabman, A., Doulatabadi, N., 1984. An efficient solvent evaporating system. Journal of Chemical Education 61, 810.

Radin, N.S., 1956. Solvent Removal by Vacuum Evaporation. Analytical Chemistry 28, 542–543.

Rahman, S.M.M., Shabnom, S., Quader, M.A., Hossain, M.A., 2010. Phytochemical study on the ethylacetate extract of the leaves of *Mesua ferrea* Linn. Indonesian Journal of Chemistry 8, 242–244.

Rajendran, M., Ravichandran, R., Devapiriam, D., 2013. Electronic Description of Few Selected Flavonoids by Theoretical Study. International Journal of Computer Applications 77, 18–25.

Raju, M.S., Srimannarayana, G., Rao, N.V.S., Bala, K.R., Seshadri, T.R., 1976. Structure of mesuaferrone-b a new biflavanone from the stamens of *Mesua ferrea* Linn. Tetrahedron Letters 17, 4509–4512.

Rakić, V.P., Skrt, M.A., Miljković, M.N., Kostić, D.A., Sokolović, D.T., Poklar-Ulrih, N.E., 2015. Effects of pH on the stability of cyanidin and cyanidin 3-O-β-glucopyranoside in aqueous solution. Hemijska Industrija 69, 511–522.

Ramalho, Í.M. de M., Bezerra, G.S., Ostrosky, E.A., Ferrari, M., Oliveira, V. da S., Wanderley Neto, A. de O., Quintans, J. de S.S., Passos, F.R.S., Heimfarth, L., Quintans-Júnior, L.J., Damasceno, B.P.G. de L., Converti, A., de Lima, Á.A.N., 2022. Chrysin-Loaded Microemulsion: Formulation Design, Evaluation and Antihyperalgesic Activity in Mice. Applied Sciences 12, 477.

Ravi, V.K., Goel, M., Kotamarthi, H.C., Ainavarapu, S.R.K., Swaminathan, R., 2014a. Preventing Disulfide Bond Formation Weakens Non-Covalent Forces among Lysozyme Aggregates. PLOS ONE 9, e87012.

Ravi, V.K., Swain, T., Chandra, N., Swaminathan, R., 2014b. On the Characterization of Intermediates in the Isodesmic Aggregation Pathway of Hen Lysozyme at Alkaline pH. PLOS ONE 9, e87256.

Reichardt, C., 2007. Solvents and Solvent Effects: An Introduction. Organic Process Research & Development 11, 105–113.

Reichardt, C., Welton, T., 2011. Solvents and Solvent Effects in Organic Chemistry. John Wiley & Sons.

Reutrakul, V., Leewanich, P., Tuchinda, P., Pohmakotr, M., Jaipetch, T., Sophasan, S., Santisuk, T., 2003. Cytotoxic Coumarins from *Mammea harmandii.* Planta Medica 69, 1048–1051.

Robards, K., Antolovich, M., 1997. Analytical Chemistry of Fruit BioflavonoidsA Review. Analyst 122, 11R-34R.

Sahu, A., Hemalatha, S., Sairam, K., 2014. Phyto-pharmacological review of *Mesua ferrea* linn. International Journal of Phytopharmacology 5, 6–14.

Sahu, A., Kasoju, N., Bora, U., 2008. Fluorescence Study of the Curcumin−Casein Micelle Complexation and Its Application as a Drug Nanocarrier to Cancer Cells. Biomacromolecules 9, 2905–2912.

Saini, R.K., Das, K., 2012. Picosecond Spectral Relaxation of Curcumin Excited State in a Binary Solvent Mixture of Toluene and Methanol. Journal of Physical Chemistry B 116, 10357–10363.

Saraf, A., Sharma, S., Sachar, S., 2018. Insights into the Interactions of Sulfamethoxazole with Organized Assemblies of Ionic and Nonionic Surfactants. Langmuir 34, 14624–14632.

Sarkar, P., Chattopadhyay, A., 2016. Micellar dipole potential is sensitive to sphere-to-rod transition. Chemistry and Physics of Lipids 195, 34–38.

Sears. D.W.,2019. Hen Egg White Lysozyme: Overview of Function and Structure. URL https://biosci.mcdb.ucsb.edu/biochemistry/tw-enz/lysozyme/HEWL/lysozyme-overview.htm (accessed August 2022).

Serajuddin, A.T.M., 1999. Solid dispersion of poorly water-soluble drugs: Early promises, subsequent problems, and recent breakthroughs. Journal of Pharmaceutical Sciences 88, 1058–1066.

Shariatizi, S., Meratan, A.A., Ghasemi, A., Nemat-Gorgani, M., 2015. Inhibition of amyloid fibrillation and cytotoxicity of lysozyme fibrillation products by polyphenols. International Journal of Biological Macromolecules 80, 95–106.

Sharma, A., Sharma, S., Rohit, Naresh, Parashar, B., 2017. *Mesua ferrae* linn:- A Review of the Indian Medical Herb. Systematic Reviews in Pharmacy 8, 19–23.

Shetab Boushehri, M.A., Dietrich, D., Lamprecht, A., 2020. Nanotechnology as a Platform for the Development of Injectable Parenteral Formulations: A Comprehensive Review of the Know-Hows and State of the Art. Pharmaceutics 12, 510.

Sigurdson, G.T., Robbins, R.J., Collins, T.M., Giusti, M.M., 2019. Molar absorptivities (ε) and spectral and colorimetric characteristics of purple sweet potato anthocyanins. Food Chemistry 271, 497–504.

Sigurdson, G.T., Tang, P., Giusti, M.M., 2018. Cis–Trans Configuration of Coumaric Acid Acylation Affects the Spectral and Colorimetric Properties of Anthocyanins. Molecules 23, 598.

Singh, A., Ansari, Mohd.Z., Senthilkumar, S., Rangan, L., Swaminathan, R., 2021. Enhanced solubility, electronic absorption and fluorescence observed for Karanjin in aqueous SDS micelles compared to water. Journal of Photochemistry and Photobiology A: Chemistry 414, 113289.

Sinopoli, A., Calogero, G., Bartolotta, A., 2019. Computational aspects of anthocyanidins and anthocyanins: A review. Food Chemistry 297, 124898.

Smaerd. **2013.** An Affordable Modular Rotary Evaporator. The art and science of amateur experimentalism. http://www.sciencemadness.org/talk/viewthread.php?tid=23139 (accessed on August 2022)

Soto, C., Pritzkow, S., 2018. Protein misfolding, aggregation, and conformational strains in neurodegenerative diseases. Nature Neuroscience 21, 1332–1340.

Stavenga, D.G., Leertouwer, H.L., Dudek, B., van der Kooi, C.J., 2021. Coloration of Flowers by Flavonoids and Consequences of pH Dependent Absorption. Frontiers in Plant Science 11.

Stefani, M., Rigacci, S., 2013. Protein Folding and Aggregation into Amyloid: The Interference by Natural Phenolic Compounds. International Journal of Molecular Sciences 14, 12411–12457.

Suhail, M., Kumar, A., Khan, A., Naeem, A., Badshah, S., 2019. Surfactants and their Role in Pharmaceutical Product Development: An overview. Journal of Pharmacy and Pharmaceiticals 6, 72–82.

Swain, T., 1975. Evolution of Flavonoid Compounds, in: Harborne, J.B., Mabry, T.J., Mabry, H. (Eds.), The Flavonoids. Springer US, Boston, MA, 1096–1129.

Swaminathan, R., Ravi, V.K., Kumar, S., Kumar, M.V.S., Chandra, N., 2011. Lysozyme: a model protein for amyloid research. Advances in Protein Chemistry and Structural Biology 84, 63–111.

Tang, C.-H., 2019. Nanostructured soy proteins: Fabrication and applications as delivery systems for bioactives (a review). Food Hydrocolloids 91, 92–116.

Tanjung, M., Saputri, R.D., Fitriati, F.F., Tjahjandarie, T.S., 2016. Antimalarial and Antioxidant Activities of Isoprenylated Coumarins from the Stem Bark of *Mesua borneensis* L. Journal of Biologically Active Products from Nature 6, 95–100.

Teh, S.S., Ee, G.C.L., Mah, S.H., 2017. Evaluation of nitric oxide inhibition effect in LPS-stimulated RAW 264.7 macrophages by phytochemical constituents from *Mesua beccariana*, *Mesua congestiflora*, and *Mesua ferrea*. Medicinal Chemistry Research 26, 3240–3246.

Teh, S.S., Ee, G.C.L., Mah, S.H., Lim, Y.M., Ahmad, Z., 2013. Cytotoxicity and structure-activity relationships of xanthone derivatives from *Mesua beccariana, Mesua ferrea* and *Mesua congestiflora* towards nine human cancer cell lines. Molecules 18, 1985–1994.

Teh, S.S., Ee, G.C.L., Rahmani, M., Taufiq-Yap, Y.H., Go, R., Mah, S.H., 2011. Pyranoxanthones from *Mesua ferrea*. Molecules 16, 5647–5654.

Ting, P., Srinuanchai, W., Suttisansanee, U., Tuntipopipat, S., Charoenkiatkul, S., Praengam, K., Chantong, B., Temviriyanukul, P., Nuchuchua, O., 2021. Development of Chrysin Loaded Oil-in-Water Nanoemulsion for Improving Bioaccessibility. Foods 10, 1912.

Tomadoni, B., Capello, C., Valencia, G.A., Gutiérrez, T.J., 2020. Self-assembled proteins for food applications: A review. Trends in Food Science & Technology 101, 1–16.

Tosif, M.M., Najda, A., Bains, A., Krishna, T.C., Chawla, P., Dyduch-Siemińska, M., Klepacka, J., Kaushik, R., 2021. A Comprehensive Review on the Interaction of Milk Protein Concentrates with Plant-Based Polyphenolics. International Journal of Molecular Sciences 22, 13548.

Tošović, J., Marković, S., 2017. Reproduction and interpretation of the UV–vis spectra of some flavonoids. Chemical Papers 71, 543–552.

Valeur, B., Berberan-Santos, M.N., 2012. Molecular Fluorescence: Principles and Applications. John Wiley & Sons.

Venkataraj, R., Girijavallabhan, C.P., Radhakrishnan, P., Nampoori, V.P.N., Kailasnath, M., 2017. Photochemical Degradation of Curcumin: a Mechanism for Aqueous Based Sensing of Fluoride. Journal of Fluorescence 27, 2169–2176.

Verotta, L., Lovaglio, E., Vidari, G., Finzi, P.V., Neri, M.G., Raimondi, A., Parapini, S., Taramelli, D., Riva, A., Bombardelli, E., 2004. 4-Alkyl- and 4-phenylcoumarins from *Mesua ferrea* as promising multidrug resistant antibacterials. Phytochemistry, 65, 2867–2879.

Vojta, D., Karlsen, E.M., Spanget-Larsen, J., 2017. Electronic states of Myricetin. UV–Vis polarization spectroscopy and quantum chemical calculations. Spectrochimica Acta Part A: Molecular and Biomolecular Spectroscopy 173, 182–187.

Wahyuningsih, S., Wulandari, L., Wartono, M.W., Munawaroh, H., Ramelan, A.H., 2017. The Effect of pH and Color Stability of Anthocyanin on Food Colorant. IOP Conference Series: Material Science and Engineering 193, 012047.

Walia, S., Mukerjee, S.K., 1984. Ferrxanthone, a 1,3,5,6-tetraoxygenated xanthone from *Mesua ferrea.* Phytochemistry 23, 1816–1817.

Wang, J., Zhao, X.-H., 2016. Degradation kinetics of fisetin and quercetin in solutions affected by medium pH, temperature and co-existed proteins. Journal of the Serbian Chemical Society 81, 243–253.

Wang, S.-Y., Wang, Y.-X., Guo, Y.-P., Huang, J., Wang, J.-H., Xiao, W., Li, Q., 2020. New cytotoxic 4-alkyl-dihydroxyfuran coumarins from *Mesua ferrea*. Phytochemistry Letters 38, 121-127.

Wypych, G., 2001. Handbook of Solvents. ChemTec Publishing.

Xin, Y., Yun, S., Yuhe, L., Yinxue, M., Shurui, N., Yue, Z., Kunming, Q., Weidong, L., 2021. Development of Licorice Flavonoids Loaded Microemulsion for Transdermal Delivery Using CCD-Optimal Experimental Approach: Formulation Development and Characterization. Frontiers in Nanotechnology 3, 748791.

Xu, Y., Wei, Z., Xue, C., Huang, Q., 2022. Assembly of zein–polyphenol conjugates via carbodiimide method: Evaluation of physicochemical and functional properties. LWT 154, 112708.

Yang, B., Dong, Y., Wang, F., Zhang, Y., 2020. Nanoformulations to Enhance the Bioavailability and Physiological Functions of Polyphenols. Molecules 25, 4613.

Yang, G-J., Xu, J-J., Chen, H-Y., Leng, Z-Z., 2004. Studies on the interaction between rutin and DNA in the absence and presence of β-cyclodextrin by electrochemical and spectroscopic methods. Chinese Journal of Chemistry 22, 1325–1329.

Yang, H., Protiva, P., Gil, R.R., Jiang, B., Baggett, S., Basile, M.J., Reynertson, K.A., Weinstein, I.B., Kennelly, E.J., 2005. Antioxidant and cytotoxic isoprenylated coumarins from *Mammea americana*. Planta Medica 71, 852–860.

Yazdanshenas, R., Gharib, F., 2016. Protonation equilibria studies of quercetin in aqueous solutions of ethanol and dimethyl sulphoxide. Journal of Molecular Liquids 224, 1227–1232.

Yuan, C.L., Xu, Z.Z., Fan, M.X., Liu, H.Y., Xie, Y.H., Zhu, T., 2014. Study on characteristics and harm of surfactants. Journal of Chemical and Pharmaceutical Research 6, 2233-2237.

Yutani, R., Morita, Sy., Teraoka, R., Kitagawa, S., 2012. Distribution of polyphenols and a surfactant component in skin during Aerosol OT microemulsion-enhanced intradermal delivery. Chemical & pharmaceutical bulletin 60, 989-994.

Zhang, L., Liu, Y., Wang, Y., 2018. Deprotonation Mechanism of Methyl Gallate: UV Spectroscopic and Computational Studies. International Journal of Molecular Sciences 19, 3111.

Zhou, F.-Z., Huang, X.-N., Wu, Z., Yin, S.-W., Zhu, J., Tang, C.-H., Yang, X.-Q., 2018. Fabrication of Zein/Pectin Hybrid Particle-Stabilized Pickering High Internal Phase Emulsions with Robust and Ordered Interface Architecture. Journal of Agricultural and Food Chemistry 66, 11113–11123.

Zhou, W., Peng, C., Wang, D., Li, J., Tu, Z., Zhang, L., 2022. Interaction Mechanism between OVA and Flavonoids with Different Hydroxyl Groups on B-Ring and Effect on Antioxidant Activity. Foods 11, 1302.